Adhesion and Friction in Single Asperity Contact

Muhammad Adeel Yaqoob

ADHESION AND FRICTION IN SINGLE ASPERITY CONTACT

Muhammad Adeel Yaqoob

This research was carried out under project number MC 7.06248 in the framework of the Research Program of the Materials innovation institute (M2i) in The Netherlands (www.m2i.nl).

De promotiecommissie is als volgt opgesteld:

prof.dr.ir. F. Eising	Universiteit Twente	Voorzitter en secretaris
prof.dr.ir. D.J. Schippper	Universiteit Twente	promotor
dr.ir. M.B. de Rooij	Universiteit Twente	assistent promotor
prof. dr. J.Th.M. de Hosson	Rijksuniversiteit Groningen	
dr.ir. W.M. van Spengen	Technische Universiteit Delft	
prof.dr.ir. G.J.M. Krijnen	Universiteit Twente	
prof.dr.ir. A.H. van den Boogaard	Universiteit Twente	
dr.ir. R.G.K.M. Aarts	Universiteit Twente	

Yaqoob, Muhammad Adeel
Adhesion and Friction in Single Asperity Contact
Ph.D. Thesis, University of Twente, Enschede, The Netherlands,
December 2012

ISBN: 978-90-77172-86-5

Keywords: tribology, adhesion, friction, single asperity contact, modelling, contact mechanics, high vacuum, van der Waals interaction.

Printed by Ipskamp Drukkers

The cover shows the stresses produced by a contact with a combined normal and tangential load made visible by polarization optics. This picture was taken by Reibungsphysik.

Adhesion and Friction in Single Asperity Contact

PROEFSCHRIFT

ter verkrijging van
de graad van doctor aan de Universiteit Twente,
op gezag van de rector magnificus,
prof.dr. H. Brinksma,
volgens besluit van het College voor Promoties
in het openbaar te verdedigen
op donderdag 20 december 2012 om 14.45 uur

door

Muhammad Adeel Yaqoob

geboren op 8 januari 1982

te Lahore, Pakistan

Dit proefschrift is goedgekeurd door:
de promotor: prof.dr.ir. D.J. Schipper
de assistent promotor: dr.ir. M.B. de Rooij

In the memory of my parents
To my beloved family

TABLE OF CONTENTS

SAMENVATTING

Adhesie en het wrijvingsgedrag van contactvlakken in positioneringsmechanismen beinvloeden de positienauwkeurigheid, herhaalbaarheid en betrouwbaarheid van de mechanismen. Met behulp van modellen en experimenten kunnen de adhesie- en wrijvingsversschijnselen op het ruwheidsniveau worden begrepen. Dit proefschrift beschrijft zowel de modellen voor de adhesie en wrijving in puntcontacten als de experimentele verificatie hiervan.

Eerst wordt een model ontwikkeld voor de adhesiekracht als functie van de relatieve luchtvochtigheid (RH; Relative Humidity). Het model beschrijft verschillende overgangen in de adhesiekracht bij veranderende RH voor hydrofiele materialen. De overgangen in de adhesiekracht komen overeen met de overgangen van de dominante adhesieve verschijnselen in het contact. Wanneer de adhesiekracht wordt berekend op basis van alleen de capillaire krachten met de Young-Laplace en Kelvin vergelijkingen voor verschillende RH, leidt dit tot een onderschatting van de totale adhesiekracht. De resultaten van het model worden vergeleken met experimenten op een puntcontact voor verschillende waardes van RH, variërend van droge (hoog vacuüm, 20 °C en 10^{-6} mbar) tot vochtige omstandigheden. De experimenten zijn uitgevoerd op een nieuw ontworpen vacuüm gebaseerde adhesie- en wrijvingstester opererend in een vacuüm omgeving (VAFT; Vacuum-based Adhesion and Friction Tester). De experimentele data komt goed overeen met het model, gebruikmakend van ruwheidseffecten als schalingsfactor.

De invloed op de adhesiekracht van andere parameters als de normaalbelasting, contacttijd en –grootte en de ruwheid van de bal, wordt bestudeerd. Het blijkt dat sommige parameters onderling afhankelijk zijn. Wanneer het contact wordt verbroken na een korte contacttijd verhoudt de adhesiekracht zich tot de $2/3^{e}$ macht ten opzichte van de normaalkracht bij kamertemperatuur en –druk. De adhesiekracht neemt toe met toenemende contacttijd in een bepaald gebied voordat er stabilisatie optreedt. Deze toename wordt verklaard met behulp van een exponentiele functie die gerelateerd is aan de condensatie van water als functie van de tijd. Zowel de effecten van de normaalbelasting als de contacttijd worden niet waargenomen als de metingen onder een hoog vacuüm (HV)

worden uitgevoerd. De invloed van de contactgrootte is ook experimenteel onderzocht, er is aangetoond dat de adhesiekracht lineair afhankelijk is van de grootte van de bal voor een contact tussen een bol en een vlak. Dit is in overeenstemming met de theoretische voorspellingen.

Verder wordt het wrijvings- en 'stick'gedrag van een puntcontact uitgelegd aan de hand van modellen en experimenten. Verschillende parameters als de statische wrijvingskracht, de statische wrijvingscoëfficiënt (COSF; Coefficient Of Static Friction), micro-slip en schuifspanningen worden berekend en gemeten voor verschillende materiaalcombinaties. De meetresultaten laten zien dat deze parameters afhankelijk zijn van de normaalbelasting en de theoretische trends volgen. De COSF wordt zowel in omgevingsomstandigheden gemeten als in HV condities. De COSF neemt af onder HV condities. Middels deze experimenten wordt Mindlin's model voor lage contactdrukken geverifieerd. Mindlin's model kan worden gebruikt om de micro-slip en schuifspanningen te berekenen als de contactdruk kleiner is dan 100 MPa. Echter, de invloed van de adhesiekracht wordt ook waargenomen in de meetresultaten voor de lage contactdrukken.

Ook wordt een methode voor de interpretatie van gecombineerde metingen van de adhesie- en statische wrijvingskracht besproken. Deze methode wordt gebruikt om het juiste adhesieve regime en het bijbehorende contactmodel te analyseren. Verder kan deze aanpak worden gebruikt om de adhesie-arbeid en schuifspanning in het contact te berekenen, gebruikmakend van de gemeten adhesie- en statische wrijvingskracht. Het in de eerste stap gekozen contactmodel blijkt heel goed overeen te komen met de gemeten statische wrijvingskracht als functie van de aangebracht normaalbelasting.

Hoewel dit proefschrift het adhesieve- en statische wrijvingsgedrag van een puntcontact beschrijft, kunnen de modellen en de experimentele resultaten worden gebruikt om het inzicht in deze fenomenen voor ruwe oppervlakken te ontwikkelen. Het werk kan bijdragen aan de verbetering van de prestatie parameters van positioneringsmechanismen in zeer nauwkeurige positioneringsmechanismen.

SUMMARY

Adhesion and friction behaviour of contacting interfaces in positioning mechanisms affects performance parameters like positioning accuracy, repeatability and reliability of said mechanisms. To understand the adhesion and friction phenomena at the interface at asperity level requires the help of models and experiments. This thesis investigates adhesion and friction models for single asperity contact, along with the verification of these models through experiments.

First, a model to calculate the adhesion force as a function of relative humidity (RH) is developed. The model shows different transitions in the adhesion force when the RH is changed for hydrophilic materials. The transitions in the adhesion force correspond to the transitions in the dominant adhesive phenomena of the contact. It is seen that the value of the adhesion force calculated by considering only capillary forces, using the Young-Laplace and Kelvin equations at different RH, underestimates the total adhesion force. The modelling results are compared with the experiments performed for a single asperity contact at different RH from dry (high vacuum (20°C and 10^{-6} mbar)) to humid conditions. The experiments were performed on a newly designed vacuum-based adhesion and friction tester (VAFT). The experimental data fits very well with the model by considering the roughness effects as a scaling factor.

The influence of other parameters like normal load, contact time and size and roughness of the ball on the adhesion force is studied. It is found that some parameters are interdependent on each other. If the contact is broken after a short contact time, a normal load to the power of 2/3 dependent adhesion force is seen when measured in ambient conditions. The adhesion force increases with the increase of the contact time in a certain range before stabilizing. This increase is explained by an exponential function related to the condensation of water with time. Both the normal load effects and contact time effects are not present when the measurements are performed in high vacuum (HV) conditions. The size effects on the adhesion force are also experimentally studied and it is shown that the adhesion force is linearly dependent on the size of the ball in a ball-flat contact. This is in agreement with the theoretical predictions.

Further, static friction and pre-sliding behaviour of a single asperity contact is explained using models and experiments. Different parameters like static friction force, coefficient of static friction (COSF), preliminary displacement and shear stress are calculated and measured for different material combinations. The measurement results show that these parameters are normal load dependent and follow the theoretical trends. The COSF is measured in ambient as well as in HV conditions and the COSF decreases when the interface is operating in HV. Verification of Mindlin's model for low contact pressures is performed. It is seen that the Mindlin model can be used to calculate the preliminary displacement and shear stress when the contact pressure is kept below 100 MPa. However, the influence of adhesion force is also seen in the measurement results at low contact pressures.

A method to interpret the adhesion and static friction force measurements performed at different values of applied normal load is also discussed. This method is used to analyse the appropriate adhesive regime and the corresponding contact model. Further, the approach can be used to calculate the work of adhesion and shear stress using the adhesion and static friction force measurements. It is seen that the selected contact model from the first step fits very well with the measured static friction force data as a function of the applied normal load.

This thesis investigates the adhesion and static friction behaviour of single asperity contact. The models and the experimental results can be used to further develop the insight of these phenomena for rough surfaces. The work can contribute in increasing the performance parameters of the positioning mechanisms in high precision positioning mechanisms.

ACKNOWLEDGEMENTS

A phase of my life is ended with the end of this thesis and I would like to take this opportunity to recall the four years I spent to complete this thesis. Looking back in time, there were many moments when a lot of people helped me out in carrying out my work smoothly. I would like to thank all who made these four years of my life easy, joyful and unforgettable.

Materials innovation institute (M2i) is thanked for arranging all the practical matters and providing me the opportunity to start my PhD in a unique environment. The ideology of M2i in simple terms "bridging the gap between the industry and the university" enhances the active involvement of the industrial partners in each and every project, which makes it more exciting, interesting and challenging. The possibility of follow-up of a research project in an application or valorization project helps to focus on the practical and rational approach. The continuous training provided by M2i on personal and professional development throughout the four years is also greatly appreciated.

I would also like to thank Edwin Gelinck and Hartmut Fischer from TNO for exchanging their knowledge and expertise on the topic and providing assistance in performing experiments at TNO. I would also like to acknowledge Professor Jeff de Hosson and Derk Bol, cluster leader of cluster 7 and program manager at M2i, respectively for showing interest in the research topic.

During these years most of my time was spent at the Surface Technology and Tribology Group at the University of Twente. A lot of people in this group have been a regular source inspiration for me. Professor Dik Schipper as a group leader and a project leader has been one of them. His powerful insight to the physical problems and his experience in solving those problems have always inspired me. Encouragement and guidance provided by him were always moral boosting and motivating. Matthijn de Rooij as my daily supervisor is gratefully acknowledged as well. He has always been available for guiding me in the right direction during these years. The discussions with you on variety of topics during travelling and coffee breaks will be remembered for a long time. I thank you Matthijn for being so patient, supportive, encouraging as well as being reachable even after office hours. I would also like to express my deep

appreciation to Eric and Walter for helping me out in the lab with the technical assistance and with building up of the test setup by exchanging amazing ideas. Specially, when I am looking for something on short notices and on the Friday afternoons they both made it possible to be arranged in time. I would also like to thank Belinda for her assistance in practical matters and Willie and Dedy for providing technical support.

Some of the moments during these four years left indelible marks on my memory and those moments I will always cherish. Thanks to my colleagues in the group: Adriana, Agnieszka, Dinesh, Dariush, Ellen, Fabin, Gerrit, Ioan, Julien, Lydia, Mahdiar, Marc, Mark, Martijn, Milad, Natalia, Noor, Radu, Rob, Sheng, Xiao, Yan and Yibo. Together with all of you I have spent remember able time and enjoyed the "fruitful" and "scientific" discussions in the coffee and lunch breaks.

I am thankful to my Pakistani friends; Hammad Nazeer, Naveed Kazmi, Sohail Niazi, Waqqar Ahmed, Mudassir, Saifullah Amir, Farrukh Qayyum, Mehdi Askari, Saqib Subhan, Imran Fazal, Rahim, Khurram, Akram Raza, Tariq, Hammad and all others who were a part of a small family we had here in Enschede. The cultural events and cricket matches organized by Pakistani Student Association at University of Twente have certain place in my memory.

My wife Rafia who came all the way to Netherlands to join me in this endeavour of life. I thank you for your love, trust, encouragement and steadfast support during these years. To my lovely and adorable son Izaan whose smile, love and energy has always been a source of solace and reinforcement.

Finally, to my parents who have supported me in every way to bring my dreams come true. I thank you both for your unconditional love, support and encouragement. I would also like to thank my brothers, sister and aunt who have hugely contributed in shaping me what I am today.

NOMENCLATURE

List of Roman Symbols

Symbols	Description	Units
A	Contact area	(m^2)
A_H	Hamaker constant	(J)
$A_{(JKR)}$	Contact area JKR	(m^2)
$A_{(DMT)}$	Contact area DMT	(m^2)
a	Contact radius	(m)
$\overline{a}$	Normalized contact radius	(-)
c	Radius of the adhesive zone	(m)
$\overline{c}$	Normalized radius of the adhesive zone	(-)
C	Dispersion interaction constant	(Jm^6)
C_{BET}	BET constant	(-)
c'	Speed of light	(m/sec)
D	Separation distance	(m)
D_h	Diameter of the hole hinge	(m)
D_i	Position of the Z-axis stage (i =1, 2…)	(m)
D_s	Surface diffusion coefficient	(m^2/sec)
d_l	Distance between two hole hinges	(m)
E	Young's modulus	(Pa)
E^*	Equivalent Young's modulus	(Pa)
E_{Al}	Young's modulus of Aluminium	(Pa)
F_a	Adhesion force	(N)
$F_a(T_c)$	Contact time dependent adhesion force	(N)
$F_{a(eq)}$	Adhesion force at equilibrium	(N)
F_{a0}	Initial Adhesion force	(N)
F_{cap}	Capillary force	(N)
F_c	Humidity dependent capillary force	(N)
F_N	Applied normal load	(N)
F_t	Maximum tangential load to start gross slip	(N)
F_f	Applied tangential load	(N)
$F(D)_{s\text{-}f}$	Dispersion force between sphere and flat	(N)
$F(D)_{Casimir\ s\text{-}f}$	Casimir force between sphere and flat	(N)

F_s	Surface tension force	(N)
F_p	Force due to capillary pressure	(N)
F_{vdw}	Van der Waals force	(N)
F_{el}	Electrostatic force	(N)
$F_{S\text{-}vdw}$	Van der Waals force for solid-solid contact	(N)
$F_{W\text{-}vdw}$	Van der Waals force for adsorbed water layers contact	(N)
G	Shear modulus	(Pa)
G^*	Equivalent shear modulus	(Pa)
h	Plank's constant	(-)
k	Boltzmann's constant	(-)
k_{tot}	Total stiffness of the hinges	(N/m)
k_h	Stiffness of one hole hinge	(N/m)
k_r	First order rate constant	(sec^{-1})
m	Ratio of radius of adhesive zone to contact radius	(-)
m_A	Diameter of a adsorbed molecule	(m)
n	Refractive index	(-)
n_{mon}	Number of molecules in one full monolayer per unit area	($molecules/nm^2$)
$\overline{P}$	Normalized applied normal load	(-)
P_{cap}	Capillary pressure	(Pa)
p	Vapour pressure	(Pa)
p_s	Saturation vapour pressure	(Pa)
Q_1	heat of adsorption of the first layer	(J)
Q_i	heat of condensation of the adsorbate	(J)
R	Radius of the sphere	(m)
R_g	Universal gas constant	(J/K.mol)
r	Distance between two atoms	(m)
r_1	Radius of the meniscus (azimuthal)	(m)
r_2	Radius of the meniscus (meridional)	(m)
r_k	Mean radius of the meniscus (Kelvin radius)	(m)
s	Radius of the stick zone	(m)
T	Temperature	(K)
T_c	Contact time	(sec)
T_f	Film thickness	(m)
t	Diffusion time	(sec)
t_h	Thickness of the hole hinge	(m)
V_m	Molar volume	(m^3)
V_i	Velocity of the positioning stage (i =1, 2…)	(m/sec)
$W(D)_{s\text{-}f}$	Interaction energy between a sphere and a flat	(J)

$W(D)_{f\text{-}f}$	Interaction energy per unit area for a flat-flat	(J/m^2)
W_{12}	Work of adhesion between two materials	(J/m^2)
w_h	Width of the hole hinge	(m)
$w(r)$	Bohr's energy between two atoms	(J)
X_1	Distance moved by X-axis positioning stage	(m)
z_0	Equilibrium separation in the Lennard–Jones potential	(m)
z	Separation distance in Lennard–Jones potential	(m)

List of Greek Symbols

Symbol	Description	Units
α_0	Electronic polarizability	C^2m^2/J
α	COS parameter	(-)
β	Mean asperity radius	(m)
γ_i	Surface energy of the material (i = 1, 2, 3, …)	(J/m^2)
γ_L	Surface tension of liquid	(J/m^2)
γ_{12}	Interfacial surface energy	(J/m^2)
δ	Deformation or indentation depth	(m)
$\overline{\delta}$	Normalized indentation depth	(-)
δ_t	Preliminary displacement before gross slip	(m)
δ_{tmax}	Maximum preliminary displacement	(m)
δ_{t1}	Calculated maximum preliminary displacement	(m)
δ_{t2}	Measured maximum preliminary displacement	(m)
δ_{tc}	Complete preliminary displacement	(m)
ε_0	Dielectric permittivity of free space	(-)
ε_i	Dielectric constant of medium (i = 1, 2, 3, …)	(-)
φ	Filling angle of the meniscus	(rad)
Λ	Diffusion length	(m)
λ	Maugis parameter	(-)
λ_c	Modified Maugis parameter	(-)
μ	Coefficient of static friction	(-)
μ_f	Coefficient of friction	(-)
μ_T	Tabor parameter	(-)
ν	Orbiting frequency of the electron	(Hz)
ν_e	Electronic absorption frequency	(Hz)
ν_p	Poisson's ratio	(-)
θ_i	Contact angle (i = 1, 2, 3, …)	(º)
ρ_i	Number density of the molecules in a solid (i = 1, 2, 3, …)	(m^3)

σ	Standard deviation of the surface roughness	(-)
σ_0	Adhesive stress outside the contact	(Pa)
σ_A	Cross sectional area of the adsorbed molecule	(m^2)
τ	Shear stress	(Pa)
τ_{JKR}	Shear stress calculated using JKR model	(Pa)
τ_{DMT}	Shear stress calculated using DMT model	(Pa)

List of Abbreviations

Abbreviations	Description
AC	Alternating current
AFM	Atomic force microscope
ATR	Attenuated total reflection
BET	Brunauer, Emmett and Teller
FFM	Friction force microscope
COF	Coefficient of friction
COSF	Coefficient of static friction
DC	Direct current
DMT	Derjaguin, Muller and Toporov
ECD	Eddy current damping
emf	Electromotive force
FMM	Force measuring mechanism
HV	High vacuum
JKR	Johnson, Kendal and Roberts
M-D	Maugis-Dugdale
MEMS	Micro electro mechanical systems
NEMS	Nano electro mechanical systems
NEXAFS	Near edge X-ray absorption fine structure spectroscopy
RH	Relative humidity
rms	Root mean square
SFA	Surface force apparatus
VAFT	Vacuum based adhesion and friction tester
XPS	X-ray photoelectron spectroscopy

Chapter 1
INTRODUCTION

In the modern era, many mechanical systems require more stringent requirements in terms of performance and reliability. The applications of these systems can be found in medical instrumentation, electron microscopes, lithography systems, as well as in aviation and space applications. Instruments like Scanning Electron Microscope (SEM), Atomic Force Microscope (AFM), Scanning Tunnelling Microscope (STM) and many others enable us to perform experiments on an atomic scale. The mechanical systems in these instruments require high reliability and accurate performance. On the other hand, the revolution in the semiconductor industry calls for more rigorous requirements for the machines in order to manufacture smaller and smaller structures accurately. Similarly, the increasing demand of developing Micro Electro Mechanical Systems (MEMS) and Nano Electro Mechanical Systems (NEMS) forces the designers and researchers to think of those phenomena that are not important on macro scale. One of the important building blocks of these scientific instruments and industrial machines is the positioning mechanism. These mechanisms are used to manoeuvre the samples or products precisely and accurately in the order of a few nanometres. Therefore, achieving the precision and accuracy in positioning in the order of a few nanometres in these machines is an important target for designers and control engineers.

1.1 High precision positioning mechanisms

The well-functioning of positioning mechanisms is dependent on the stiffness, mass and damping of the mechanism, but also on the properties of the mating materials as well as on frictional behaviour. At the start-stop positions or another position where velocity changes sign, a transition from (temporary) slip to stick and vice versa between the two contacting bodies takes place. The actual frictional behaviour in terms of slip to stick transitions will, for example, influence the exact stop position and influence the preservation of a fixed position, i.e. drift-control, in positioning mechanisms. Another important effect on the positioning is the presence of adhesion between the mating materials.

The adhesion behaviour can directly or indirectly influence the frictional behaviour.
High precision positioning mechanisms are often found to be operating in medium to high vacuum conditions in the above-mentioned applications. There are several reasons why these mechanisms are operating in a vacuum environment. First, the application of positioning mechanisms, like in electron microscopes and space applications, restricts their use to high vacuum conditions. Secondly, to avoid the influence of the contaminants and the environmental variations on the performance of the positioning mechanisms, they are operating in vacuum conditions. In normal environmental conditions friction and wear is controlled by adding a liquid lubricant to the system. In a vacuum environment the use of liquid lubricants is neither possible nor desired since they could evaporate and cause contamination of the whole system.
MEMS based positioning mechanisms are severely affected by the adhesion and frictional behaviour of the surfaces in contact. High adhesion can permanently malfunction the mechanism and is described as *stiction* in the MEMS field. Similarly, high friction can cause severe damage to the contacting surfaces and can cause wear that eventually forces the mechanism to fail. Therefore, it is important to understand the adhesion and friction behaviour in ambient as well as in vacuum conditions of the surfaces in contact in high precision positioning mechanisms.

1.2 Surfaces in contact

Two or more surfaces in contact with each other are found almost everywhere around us. The nature of the contact, although different, depends on various factors such as material properties, environmental conditions, the forces that are involved as well as surface properties of the contacting surfaces. A simple example of two surfaces in contact is shown in Figure 1.1. The surfaces are brought into contact by applying a normal load on the upper block. If this normal load is removed, the surfaces remain in contact due to the presence of *adhesion force*. The adhesion force is the force developed due to the interaction of the surfaces in contact and is typically characterized by the pull-off force, the force required to separate the surfaces in normal direction. On the other hand, when the lower block is dragged with respect to the upper block, there is an opposing force to the motion of the block. This opposing force is called the *friction force* and is equal in magnitude to the applied tangential load to drag the block, but opposite in direction. If the contact surfaces of these blocks are carefully examined under the microscope a profile as shown in Figure 1.1(ii) and Figure 1.1(iii) can be seen with *a, b, c, d* and *e* as some of the points under consideration. It can be seen that the *apparent* area of contact shown in Figure

1.1(i) is much larger than the *real* area of contact between the two surfaces as shown in Figure 1.1(ii) and Figure 1.1(iii).The profile of the surfaces shown in Figure 1.1(ii) and Figure 1.1(iii) is called the *surface roughness* of the material. On microscopic scale every surface has a certain roughness and a large number of micro-contacts are formed. To determine the adhesion and frictional behaviour between the two surfaces and its impact on positioning accuracy, the adhesion and friction of a single micro-contact or simply a *single asperity contact* is focused in this study.

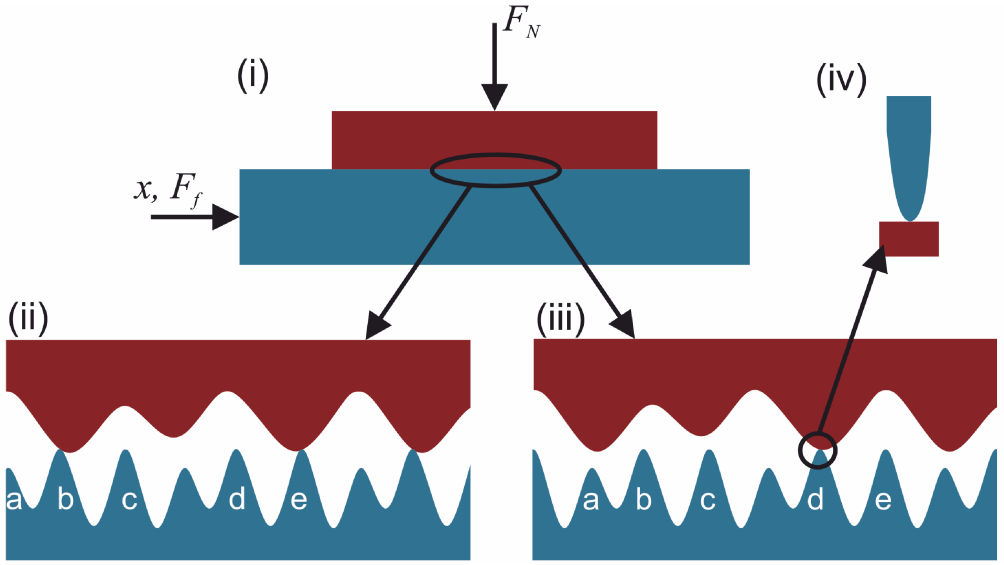

Figure 1.1: (i) Two surfaces in contact under an applied normal load F_N. A schematic microscopic view of the two surfaces in contact with multiple asperities with (ii) and without (iii) applied tangential force F_f and displacement x. (iv) A microscopic view of the single asperity contact.

A single asperity contact is defined in a simplified way as a spherical surface in contact with a flat surface as shown in Figure 1.1(iv). During the sliding movement of the block this single asperity can be in contact or it can be some distance apart from the flat counter surface. Therefore, in reality, these asperities are undergoing stick–slip and slip–stick transitions during motion of the surfaces. Similarly, the adhesion behaviour of a single asperity contact is different if it is in contact as compared to if it is a very small distance apart. The adhesion and friction behaviour of a single asperity contact is important to understand the overall adhesion and friction behaviour of surfaces in contact. Therefore, this study is focused on developing adhesion and friction models for a single asperity contact and validating them through experiments.

1.3 Adhesion and friction behaviour of single asperity contact

As defined above, the adhesion and friction forces are present when the surfaces are in contact under an applied normal load and are subjected to a lateral (tangential) motion. The friction force can be divided into two regimes, the *static friction regime* and the *dynamic friction regime*. This study focuses on studying the static friction behaviour of the surfaces in contact. There are many factors which influence the behaviour of adhesion and the static friction force. The humidity of the environment influences the adhesion force between two *hydrophilic* materials [1-6]. A hydrophilic material is defined as a material which attracts the water molecules on its surface. A material which repels the water on its surface is termed as *hydrophobic* material. The adhesion force is influenced by the presence of water in the ambient environment by the formation of the meniscus around the contact. In HV conditions the adhesion force is expected to be contributed predominantly by van der Waals interactions. Therefore, it is expected to have different adhesion and friction behaviour for the same system when it is operating in high vacuum (HV) conditions as compared to ambient conditions.

On the other hand, the surface roughness of the interface also plays an important role in determining the adhesion force between the interface. It is known that the adhesion force decreases considerably if the surface roughness is increased [5, 7-10]. However, the friction force can increase as the surface roughness is increased. One of the reasons for this can be due to the interlocking between the asperities as shown in Figure 1.1. Similarly, the effect of contact time/ rest time on the adhesion and friction force is also not clearly known [9-12]. The effect of applied normal load is also an important parameter both for adhesion and frictional behaviour.

Before sliding occurs, so during the static friction regime, there is always a displacement in the order of nanometres present when a tangential load is applied to move the two surfaces relative to each other in lateral direction [13-15]. This displacement is termed as *preliminary displacement* or micro-slip, which will be explained in Chapter 2 and Chapter 6. The presence of this preliminary displacement causes positioning errors at start/stop positions.

It is therefore required to analyse adhesion, friction and preliminary displacement of a single asperity contact both qualitatively and quantitatively using models and experiments. This will help to enhance the performance of positioning mechanisms. Furthermore, the relation between adhesion and friction force is not very well understood. The friction force is acting in lateral direction, whereas the adhesion force is acting in normal/oblique direction and

both phenomena may influence each other. The schematic representation of the two forces for a ball in contact with a flat surface is shown in Figure 1.2.

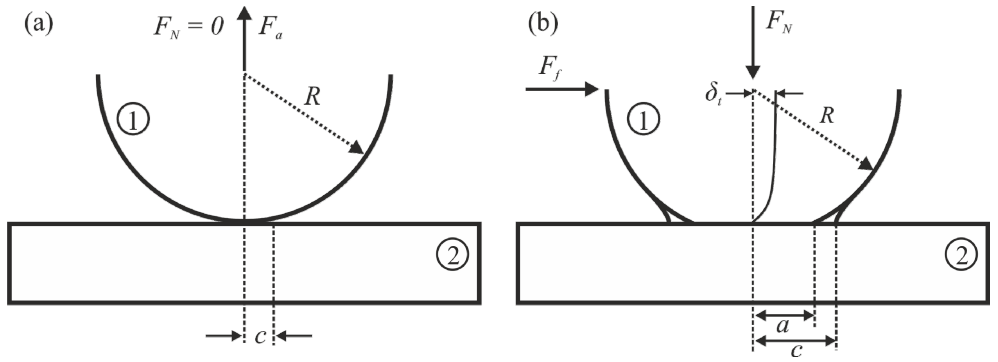

Figure 1.2: (a) A spherical surface of radius R being pulled away from a flat surface with a pull-off force F_a when the applied normal load is zero. (b) Similar surface in contact with a flat surface with a normal load F_N and an applied tangential load F_f to move the ball over the flat surface.

1.4 Objectives of this research

The aim of this study is to understand the adhesion and frictional behaviour at asperity level of the surfaces in contact in ambient and high vacuum environments. The main objectives of this research can be formulated as follows:

- Development of an adhesion model for single asperity contact explaining the potential effects of van der Waals and capillary forces in ambient and HV conditions. The effects of RH on the adhesion force need to be considered.

- Modelling the pre-sliding behaviour of a single asperity contact in order to quantify the static friction behaviour and the preliminary displacement.

- Validation of the adhesion models through experiments at single asperity contact level under ambient and HV conditions.

- Performing sliding experiments in order to verify the pre-sliding behaviour as modelled.

The materials used in this study are limited to glass and ceramics.

1.5 Outline of the thesis

In this thesis the focus is on the adhesion and static friction behaviour of a single asperity contact. In this chapter, the problem has been formulated along with the aims and objectives considering the application of this research i.e. the effect of adhesion and static friction on the performance of high precision positioning mechanisms operating in vacuum environments. Adhesion and friction mechanisms, as well as the concept of single asperity contact, have also been briefly explained.

In Chapter 2, a detailed explanation of the adhesion and friction force mechanisms for a single asperity contact is outlined. The surface forces that contribute to the total adhesion force and the theory behind these forces are discussed in detail. Different contact mechanics models with and without contribution of an adhesion force are also elaborated. A discussion then follows on the importance of the role that surface properties and the surrounding environment have on determining the nature and the magnitude of the adhesion force. Similarly, the mechanism of friction and especially static friction is presented.

The experimental setup developed to study the adhesion and friction behaviour of single asperity contact both in ambient and high vacuum (HV) conditions is described in Chapter 3. The detailed design and analysis of the vacuum based adhesion and friction tester (VAFT), along with the methods to reduce disturbances on the measurements, is discussed. The properties of the materials used in this study are also elaborated in this chapter. Furthermore, the methods and procedures by which the adhesion and static friction force measurements were performed are presented.

In Chapter 4, the influence of parameters such as relative humidity (RH), applied normal load and contact time/rest time, on the adhesion force for a single asperity contact is studied. Mathematical models are presented to show the effect of these parameters on the adhesion force. A newly developed model to describe the influence of RH on the adhesion force for hydrophilic materials is discussed in detail. The model is compared with the experimental data from the literature on nano scale contacts. The interdependency of normal load and contact time effects is discussed and their effect on adhesion force is studied.

The experimental validation of the models discussed in Chapter 4 is explained in Chapter 5. The parameters like RH, applied normal load, contact time/rest time, surface roughness and size of the asperity are studied in detail. For this purpose, experiments have been performed on VAFT for single asperity contact

using different material combinations. The effect of RH on the adhesion force has been experimentally studied and compared with the newly developed model explained in Chapter 4. The measurement results fit very well to the model if the effect of surface roughness is taken into account. Similarly, the effects of contact time on the adhesion force is studied by performing adhesion experiments with short and long contact times. Size and surface roughness effects are also studied and it can be seen that both effects are interconnected for the material combinations used in the experiments.

Chapter 6 deals with the static friction model for single asperity contact and its verification with the help of static friction experiments. The model can be used to calculate the preliminary displacement and the shear stress in the contact before full slip. The experiments are performed to study the parameters like static friction force, coefficient of static friction, preliminary displacement and shear stress. The experiments are performed with different material combinations and the results show good agreement with the theoretical calculations. The magnitude of preliminary displacement during pre-sliding can be used to define the positioning error in the positioning of a single asperity contact.

The relation between adhesion and static friction is discussed in Chapter 7. The selection of the appropriate contact model applicable for a set of friction measurements is performed using Maugis-Dugdale contact model. Two sets of measurements in ambient as well as in HV conditions have been used to formulate the relation between adhesion and friction along with the verification of the selected contact model. Important parameters like work of adhesion and shear stress can be calculated using the adhesion and static friction force measurements performed at different normal loads. The analysis procedure shows that the selected contact model fits very well to the measured data.

Finally, the conclusions of this research are drawn in Chapter 8 along with a discussion and recommendations for future research.

Chapter 2
ADHESION AND FRICTION FORCE MECHANISMS

2.1 Introduction

In this chapter the focus will be on the adhesion and friction force mechanisms for a single asperity contact. The contribution of different surface forces like van der Waals force and capillary force to the adhesion force are discussed in section 2.2. In section 2.3 different contact mechanics theories are discussed explaining the contact models incorporating adhesion force. In section 2.4 mechanics of friction force and the theories involved in describing the static friction force are presented.

2.2 Adhesion force–Role of surface forces

When two surfaces are brought closer to each other or make contact with each other, different types of surface forces are present between them. The combination of these surface forces gives rise to adhesion force. The magnitude of these forces is dependent on the complete contact and involves parameters like:

- Size and shape of the contacting surfaces
- Materials combination/coatings
- The environment through which they act or are dominant
- Separation distance over which they act or are dominant (contact/non-contact)
- Deformation mode in the surface (elastic, elastic-plastic, plastic)

The main contributors to the short and long–range surface interactions are often the *van der Waals forces* [5, 7]. Van der Waals interactions can be both attractive and repulsive. There are different kinds of van der Waals interactions present depending on the properties of the materials. In the case of a vapour environment as the third medium (e.g., atmospheric air containing water), one

has also to consider modifications as compared to dry conditions due to surface adsorption. This can lead to force modification or additional forces such as the strong attractive *capillary forces* [5, 7, 16]. The analytical equations involved for calculating these forces under different conditions and different assumptions are presented in section 2.2.1 till section 2.2.2.

2.2.1 Van der Waals force

The van der Waals force is the attractive or repulsive force between atoms or molecules other than those due to covalent bonds or to the electrostatic interaction of ions. Van der Waals forces also act between neutral molecules. They are caused by correlations in the fluctuating polarizations of nearby particles [7]. Van der Waals forces are of different types depending on the properties of the material. As shown in Figure 2.1 the molecules having permanent dipoles have *dipole–dipole (Keesom) forces*, the molecules having permanent dipoles interacting with neutral molecules give rise to *induced dipole (Debye) forces* and the interaction of two non–polar molecules would give rise to *dispersion or London forces* [5]. All these three types of surface forces have the same separation distance dependency [16]. Casimir and Polder [17] introduced the retardation effect to the London forces which is known as the *Casimir forces*. The van der Waals force between any two materials in vacuum is always attractive; the force between two identical materials is also always attractive; and the force between two different materials in a liquid medium can be repulsive [18]. In the following sections only dispersion force will be discussed in more detail because the materials under consideration in this study are non-polar by nature.

2.2.1.1 Dispersion force

The dispersion force is the force which acts between molecules or atoms that are non-polar by nature. Due to charge fluctuations of the atoms there is an instantaneous displacement of the centre of positive charge against the centre of negative charge. Thus at a certain instant a dipole exists and induces a dipole in another atom. Therefore non-polar atoms (e.g. neon) or molecules attract each other. Dispersion force is perhaps the most important contribution to the total van den Waals force between atoms and molecules [5, 7] as shown in Figure 2.1. These forces are always present in contrast to the other types of forces that may or may not be present depending on the type of molecules. These forces are the source of the important phenomena such as adhesion, surface tension, physical adsorption, wetting, properties of gases liquids and thin films etc. Their main features are summarized as follows [5, 7].

1- They are long-range forces and, depending on the situation, can be effective from large distances (greater than 10 nm) down to inter-atomic spacing (about 0.2 nm).

2- These forces may be repulsive or attractive.

3- The dispersion interaction of two bodies is affected by the presence of other bodies nearby.

4- The dispersion force is always present between materials.

5- The dispersion force does not decrease with temperature, unlike the orientation force.

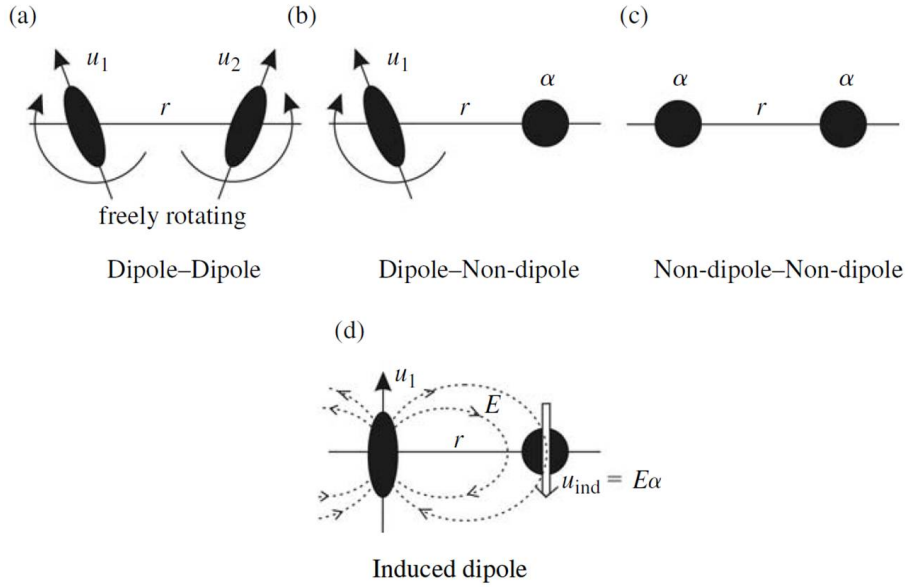

Figure 2.1: Schematic of the three types of van der Waals interactions between molecules: (a) *Dipole-Dipole interaction* between two freely rotating polar molecules. (b) *Dipole-Induced Dipole interaction* between a polar and a non-polar molecule. (c) *Dispersion interaction* between two non-polar molecules. (d) Illustrates how the electric field E of a polar molecule induces a dipole in a non–polar molecule [5].

There are two different theories, *pairwise additivity* and *Lifshitz*, to calculate the van der Waals interaction between two molecules or between two materials. Both theories are based on different physical phenomena and take some assumptions into consideration. In the following sections a brief introduction to these theories has been discussed.

2.2.1.1.1 Theory of pairwise additivity

The attractive energy of the interaction of two Bohr atoms in vacuum is explained in [7] and is given by:

$$w(r) \approx -\frac{\alpha_0^2 h\nu}{(4\pi\varepsilon_0)^2 r^6} \tag{2.1}$$

Where, α_0 is the electronic polarizability of the second Bohr atom, h is the Plank's constant and ν is the orbiting frequency of the electron, ε_0 is the dielectric permittivity of free space and r is the distance between the two atoms. It can be seen that the energy is inversely proportional to the r^6. The equation given by London's theory was the same as given by Bohr except for the numerical factor of *3/4* [7]. Therefore, London introduces a constant factor termed as London's constant for dispersion interaction or simply interaction constant C defined as [7]:

$$C = \frac{3\alpha_0^2 h\nu}{4(4\pi\varepsilon_0)^2} \tag{2.2}$$

So Eq. (2.1) can be written as:

$$w(r) \approx -\frac{C}{r^6} \tag{2.3}$$

To find the van der Waals interaction energies in vacuum for macroscopic bodies, one may sum (integrate) the energies of all atoms in one body with all the atoms in the other (*simple pairwise additivity*). The interaction energy between a macroscopic sphere and a flat surface (Figure 2.2) can then be calculated as [7]:

$$W(D)_{s-f} = -\frac{A_H R}{6D} \tag{2.4}$$

Similarly, the interaction energy between two flat surfaces per unit area is given by:

$$W(D)_{f-f} = -\frac{A_H}{12\pi D^2} \tag{2.5}$$

Where, R is the radius, D the distance between the sphere and the flat surface. The interaction constant A_H, is called *Hamaker constant,* defined as [7]:

$$A_H = \pi^2 C \rho_1 \rho_2 \tag{2.6}$$

Where, C is the interaction and ρ_i is the number density of the molecules in the solid (i = 1, 2). Typical values for the Hamaker constants of condensed phases, whether solid or liquid, are about 10^{-19} *J* for interaction across *vacuum*. The Hamaker constants of most condensed phases are found in the range $(0.4–4)\times10^{-19}$ *J*. Hamaker constants of some similar media interacting with each other calculated using Eq. (2.6) (pairwise additivity) are shown in Table 2.1 [7]. The interaction force can then be calculated as:

$$F(D) = -\frac{dW(D)}{dD} \tag{2.7}$$

Therefore the interaction force can be calculated by differentiating Eq. (2.4) for a sphere flat interaction and Eq. (2.5) for two flat surfaces.

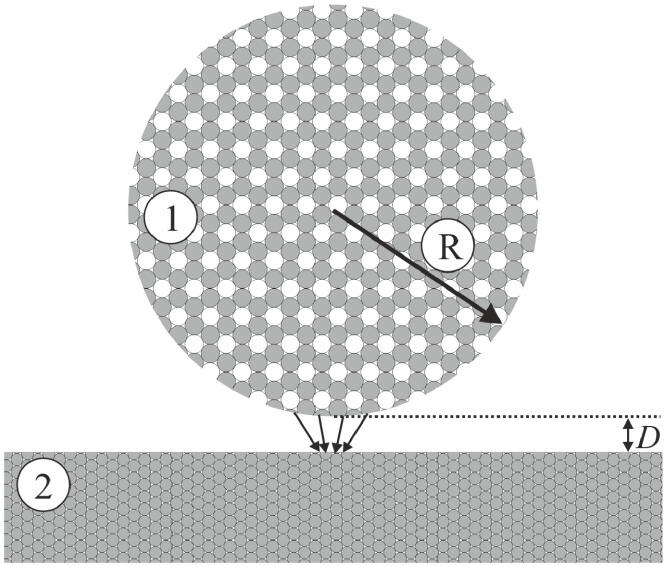

Figure 2.2: A spherical surface of radius R separated by distance D from a flat surface. The arrows indicate schematically the attractive force between two surfaces.

Table 2.1: Hamaker constant of similar media interacting with each other determined from pairwise additivity [7].

Medium	C **(10^{-79} Jm^6)**	ρ **(10^{28} m^{-3})**	A_H **(10^{-19} J)**
Hydrocarbon	50	3.3	0.5
CCl_4	1500	0.6	0.5
H_2O	140	3.3	1.5

The forces between the macroscopic bodies are often easier to measure and of greater interest than their interaction energies. Therefore, it is desirable to approximately relate forces between two curved surfaces to the interaction energy of two planar surfaces. This approximation is a very useful tool, since it is usually easier to derive the interaction energy for two planar surfaces rather than for curved surfaces. This approximation is called the *Derjaguin Approximation* [5, 7, 16]. For example, if we have two large spheres of radii R_1 and R_2 a small distance D apart and if $R_1 \gg D$ and $R_2 \gg D$, then the force between two spheres can be obtained by integrating the force between small circular regions assumed to be locally flat. The force between two spheres in terms of the energy per unit area of two flat surfaces at the same separation D is given as [7]:

$$F(D)_{s-s} = 2\pi\left(\frac{R_1 R_2}{R_1 + R_2}\right)W(D)_{f-f} \tag{2.8}$$

A sphere near a flat surface is a special case of two spheres with one sphere very much larger than the other $R_2 \gg R_1$.

$$F(D)_{s-f} = 2\pi R W(D)_{f-f} \tag{2.9}$$

The Derjaguin Approximation is applicable to any type of force law, whether attractive, repulsive or oscillatory as long as the range of interaction and the separation D is much less than the radii of spheres. Substituting Eq. (2.5) in Eq. (2.9) we get:

$$F(D)_{s-f} = -\frac{AR}{6D^2} \tag{2.10}$$

2.2.1.1.2 Lifshitz theory of van der Waals force

Another theory of van der Waals forces is the *Lifshitz Theory* in which the forces between macroscopic bodies are treated as continuous media and are represented in bulk properties of materials such as dielectric constants ε and refractive indices n [5, 7, 16]. The Lifshitz theory avoids the assumption of additivity. The theory of additivity does not incorporate the influence of neighbouring atoms on interaction energy or force between any pair of atoms. In other words, the assumption of the additivity ignores the existence of multiple reflections. Multiple reflections occur when atom A induces a dipole in atom B. At the same moment the field of atom A polarizes also another atom C.

This induced dipole of atom C, influences atom B. Therefore the field of atom A reaches atom B directly and via reflection from atom C.
The Hamaker constant calculated using Lifshitz theory is dependent on the phases and interacting medium across the bodies. The Hamaker constant for two macroscopic phases 1 and 2 interacting across a medium 3 is given as [7]:

$$A_H \approx \frac{3}{4}kT\left(\frac{\varepsilon_1-\varepsilon_3}{\varepsilon_1+\varepsilon_3}\right)\left(\frac{\varepsilon_2-\varepsilon_3}{\varepsilon_2+\varepsilon_3}\right)+\frac{3h}{4\pi}\int_{\nu_1}^{\infty}\left(\frac{\varepsilon_1(i\nu)-\varepsilon_3(i\nu)}{\varepsilon_1(i\nu)+\varepsilon_3(i\nu)}\right)\left(\frac{\varepsilon_2(i\nu)-\varepsilon_3(i\nu)}{\varepsilon_2(i\nu)+\varepsilon_3(i\nu)}\right)d\nu \quad (2.11)$$

Here, k is the Boltzmann's constant and T is the temperature. If the adsorption frequencies of all the three media are assumed to be the same, the following approximate expression can be achieved:

$$\begin{aligned} A_H &= A_{H\nu=0} + A_{H\nu>0} \\ &\approx \frac{3}{4}kT\left(\frac{\varepsilon_1-\varepsilon_3}{\varepsilon_1+\varepsilon_3}\right)\left(\frac{\varepsilon_2-\varepsilon_3}{\varepsilon_2+\varepsilon_3}\right)+\frac{3h\nu_e}{8\sqrt{2}}\frac{\left(n_1^2-n_3^2\right)\left(n_2^2-n_3^2\right)}{\sqrt{\left(n_1^2+n_3^2\right)\left(n_2^2+n_3^2\right)}\left\{\sqrt{\left(n_1^2+n_3^2\right)}+\sqrt{\left(n_2^2+n_3^2\right)}\right\}} \end{aligned} \quad (2.12)$$

For the symmetric case of two identical phases 1 interacting across medium 3, the above equation reduces to a simple expression [7]:

$$A_H = A_{H\nu=0} + A_{H\nu>0} = \frac{3}{4}kT\left(\frac{\varepsilon_1-\varepsilon_3}{\varepsilon_1+\varepsilon_3}\right)^2+\frac{3h\nu_e}{16\sqrt{2}}\frac{\left(n_1^2-n_3^2\right)^2}{\left(n_1^2+n_3^2\right)^{3/2}} \quad (2.13)$$

Where, $A_{H\nu=0}$ and $A_{H\nu>0}$ are the contribution in the Hamaker constant for zero-frequency energy and the dispersion energy of the van der Waals interaction respectively. Also the ε_i and n_i are the dielectric permittivity and refractive index of the medium i (i = 1…3). The h and ν_e (3×10^{15} s^{-1}) are the Plank's constant and electronic absorption frequency respectively. The above expressions for A_H apply to any of the macroscopic geometries. The non–retarded Hamaker constant for two identical media interacting across vacuum is shown in Table 2.2. It can be seen from Table 2.1 and Table 2.2 that the Hamaker constant calculated with pairwise additivity is one order of magnitude higher than the one calculated with the Lifshitz theory. The Hamaker constant for water with pairwise additivity is 1.5×10^{-19} J, whereas with Lifshitz theory it is 3.7×10^{-20} J.

The above analysis applies to dielectric or non-conducting materials. For interactions involving conducting media such as *metals,* their static dielectric constant is *infinite*. The Hamaker constant for two metals interacting across vacuum is given by [7]:

$$A_H \approx \left(3/16\sqrt{2}\right) h\nu_e \approx 4\times10^{-19} J \tag{2.14}$$

The separation distance D in the van der Waals force expression Eq. (2.10) plays a very important role in estimating the total van der Waals force. At distances beyond 5 nm the dispersion contribution $A_{H\nu>0}$ to the total van der Waals force begin to decay more rapidly due to *retardation effects* [7]. This effect is negligible for the interactions between molecules. However, for interactions between macroscopic bodies, where the forces can still be significant at such large separations, the effect of retardation must be taken into account. Eq. (2.12) and Eq. (2.13) give the relationship for the non–retarded

Table 2.2: Non–retarded Hamaker constant for two identical media interacting across vacuum [7].

Medium	Hamaker constant A_H (10^{-20} J)	
	Eq. (2.13) $\varepsilon_3 = 1$	Eq. (2.11) Exact solutions
Water	3.7	3.7, 4.0
Hydrocarbon (crystal)	7.1	–
Alumina (Al_2O_3)	14	–
Iron oxide (Fe_3O_4)	21	–
Zirconia (n–ZrO_2)	27	–
Silicon carbide	44	–
Metals (Au, Ag, Cu)	25–40	30–50

Hamaker constant. Efforts have been made to compute the van der Waals force at all distances by solving the full Lifshitz equation but this requires numerical computation methods [7]. Figure 2.3 shows the dispersion force as a function of separation distance of a sphere and a flat surface. As the separation distance is increased the van der Waals force begins to decay more rapidly.

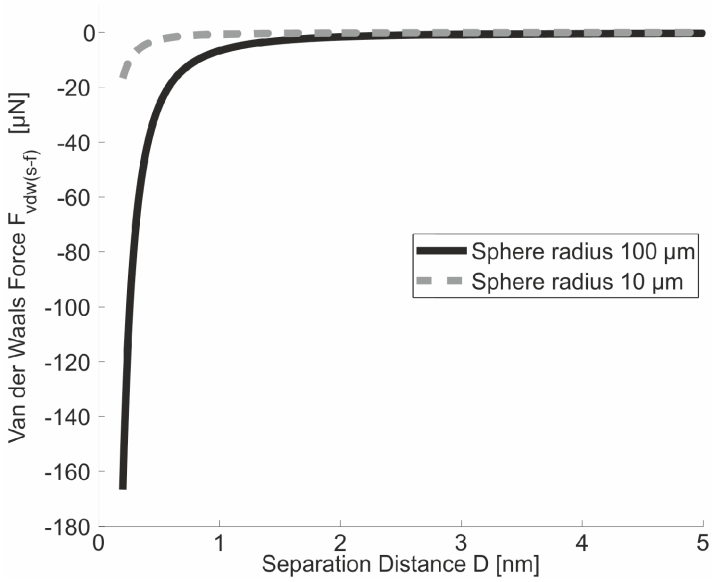

Figure 2.3: Relation between separation distance and van der Waals dispersion force with two different sized spheres.

It is important to mention the significance of van der Waals forces between surfaces with thin absorbed layers. If we have two similar surfaces (say metal) with absorbed layers (say water) across a certain medium, the van der Waals interaction depends on the separation distance. At large separation distance they are dominated by the properties of material of the surface, whereas at separation distance less than the thickness of the absorbed layers they are dominated by the properties of the absorbed layers [7]. The reason behind this is the strong dependency of the interaction force on the separation distance.

2.2.1.2 Casimir force

The Casimir effect is the interaction of a pair of neutral, parallel conducting planes due to the disturbance of the electromagnetic field in vacuum. A vacuum always contains fluctuating electromagnetic fields, which are normally the same everywhere. Due to this variation in electromagnetic field, attractive or repulsive interaction is observed. As mentioned in Section 2.2.1.1 the van der Waals force starts to decay as the separation between two atoms is increased; this is called the retardation effect. The finite force per unit area acting between the two parallel neutral plates derived by Casimir is as follows [19]:

$$F(D)_{Casimir\ f-f} = -\frac{\pi}{480}\frac{hc'}{D^4} \tag{2.15}$$

Where, c' is the speed of light. An important feature of the Casimir effect is that even though it is quantum by nature, it predicts a force between macroscopic bodies. For two plane parallel metallic plates of area $1\ cm^2$ separated by a large distance (on the atomic scale) of $D = 1\ \mu m$ the value of the attractive force given by Eq. (2.15) is $F(D)_{Casimir} \approx 1.3\times10^{-7}\ N$. The Casimir force is strongly dependent on the shape and geometry of the interacting surfaces [19]. The Casimir force acting between a flat and a sphere is given in [19] as:

$$F(D)_{Casimir\,s-f} = -\frac{\pi^2 hc'R}{720D^3} \tag{2.16}$$

Casimir and Polder have generalized the London forces to include the retarded regime [10]. In Section 2.2.1.1 the non-retarded van der Waals energy and forces for a sphere-planar geometry are explained. From Eq. (2.10) we can see that the non-retarded force is proportional to $1/D^2$ and from Eq. (2.16) we can see that the Casimir force is proportional to $1/D^3$ which is applicable for large distances as proposed by Casimir and Polder [17]. It is also clear from Figure 2.3 that the van der Waals force is retarded at a distance of 2 nm whereas in Figure 2.4 the Casimir force is still significant at the same distance. This is in agreement with the citation that the Casimir force is actually the retarded van der Waals force between two surfaces, which acts at large separation distances (on atomic scale).

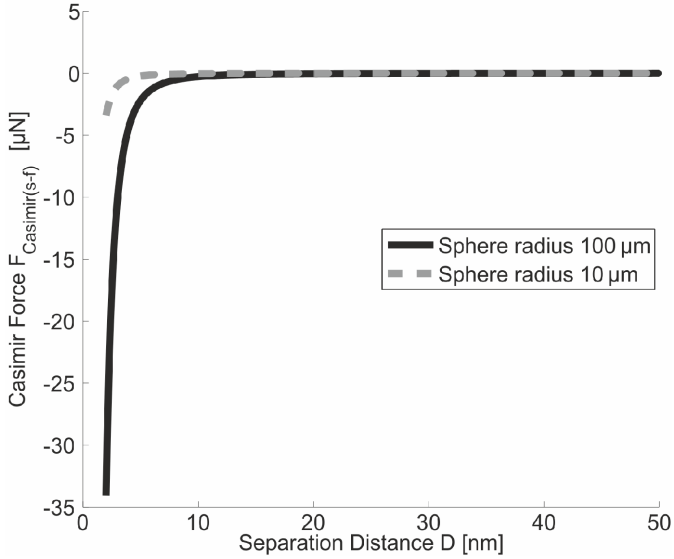

Figure 2.4: Casimir force as a function of separation distance for two different sized spheres.

2.2.2 Capillary force

Capillary forces are meniscus forces due to condensation. The capillary forces or the meniscus forces are present when the surfaces are in contact or are close to each other under humid conditions. This force can be attractive or repulsive, meaning that the two surfaces can attract or repel each other depending on the materials of the surfaces [5]. The capillary or meniscus force can be larger than the expected van der Waals force. However, control of the ambient conditions such as working under dry nitrogen, in vacuum, or in liquids, often eliminates this meniscus effect [18]. But even when maintaining a vacuum of 6×10^{-5} *mbar* and/or dry argon atmosphere at room temperature or after purging with dry nitrogen, the removal of water vapours is often not successful [3, 20]. The capillary force originates from the capillary pressure P_{cap} generated by the curvature of the meniscus surface acting over the area of the meniscus. The P_{cap} is given by the equation of Young and Laplace [5]:

$$P_{cap} = \gamma_L \left(\frac{1}{r_1} + \frac{1}{r_2} \right) \approx \frac{\gamma_L}{r_1} \qquad r_2 >> r_1 \tag{2.17}$$

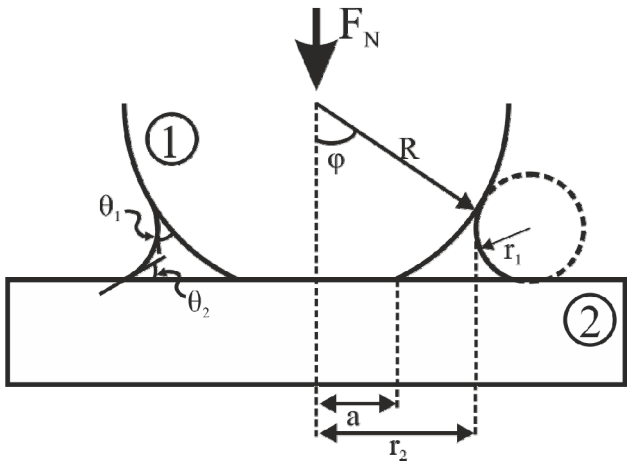

Figure 2.5: A sphere in contact with a flat surface under a certain applied normal load F_N in a humid environment. The solid–solid contact radius a and the meniscus radius r_2 are also shown.

Where, r_1 and r_2 are the two principal radii of curvature that define the curved surface as shown in Figure 2.5 and γ_L is the surface tension of the liquid (water). The capillary force is strongly influenced by the nature of the surfaces under consideration. The capillary force is given as:

$$F_{cap} = -2\pi R\gamma_L \left(\cos\theta_1 + \cos\theta_2 \right) \tag{2.18}$$

Where, R is the radius of the sphere and $\theta_{1,2}$ are the contact angles at the surfaces. The negative sign shows that the force is attractive. This means that the capillary force is directly influenced by the contact angles at the surfaces. Eq. (2.18) indicates that the capillary force increases with decreasing contact angle (increasing hydrophilicity) of the surfaces [9]. It is important to mention here that Eq. (2.18) shows that the capillary force is independent of RH and does not consider contact deformation between the probe and substrate and also ignores the adsorption layers on the surfaces [3]. Furthermore, there is strong experimental evidence of RH dependence of the capillary force [1, 3, 4, 6]. From the *Kelvin equation* the *Kelvin radius* r_k, which is the mean radius of curvature of the condensed meniscus, is given as [5]:

$$\left(\frac{1}{r_1}+\frac{1}{r_2}\right)^{-1} = r_k = -\frac{\gamma_L V}{R_g T \log\left(\frac{p}{p_s}\right)} \tag{2.19}$$

Where, p/p_s is the relative humidity (RH), V is the mol volume, R_g the gas constant and T is the absolute temperature. For water, $\gamma_L=73\ mJ/m^2$ at $T=293\ K$ and this gives $\gamma_L V/R_g T = 0.54\ nm$. Consequentially, the Kelvin radius for 90% RH is approximately *100 Å*. This also means that at 90% relative humidity the meniscus is formed when the surfaces are approximately *200 Å* apart. The force acting on the sphere due to meniscus formation when the meniscus is in equilibrium is written as [1]:

$$F_c = F_s + F_p \tag{2.20}$$

$$F_s = -2\pi\gamma_L r_2 \sin(\theta_1+\varphi) = -2\pi\gamma_L R \sin\varphi \sin(\theta_1+\varphi) \tag{2.21}$$

$$F_p = -P_{cap}\pi\left(r_2{}^2 - a^2\right) = -\left[-\frac{R_g T}{V_m}\log\left(\frac{p}{p_s}\right)\right]\pi\left(R^2\sin^2\varphi - a^2\right) \tag{2.22}$$

Where, F_s is the surface tension force which is attractive and F_p is the capillary pressure force which is also attractive because the pressure in the liquid is lower than in the outer vapour phase. The negative sign shown in Eq. (2.22) with log (p/p_s) term is due to the fact that log (p/p_s) < 0.

The validity of Kelvin's equation is a concern at low humidity levels. At RH = 10% the Kelvin radius is 5.4 Å which is approaching the size of water molecule [21]. Therefore, the Kelvin's equation at very low RH (RH<10%) cannot be applied [21]. Similar argument was also reported in [3] that the existing theories based on continuum mechanics are not sufficient for precise computation of

capillary forces at very low RH values. Moreover, it was shown that during adhesion experiments the water bridge stretches to a certain distance before the contact is ruptured and this distance is much larger than $2r_k$ [22, 23]. The experiments were conducted at RH = 15% and T = 20°C which results in $2r_k$ = *13 Å*. The snap–in and breakup occurs at *4 nm* and *15 nm* respectively [23]. Therefore, it was concluded that the snap–in and breakup distances are not related to the Kelvin radius but were related to the volume of the water bridge formed at the contact [23].

It has been reported that in general there are three regimes in a relationship between relative humidity and adhesion force for hydrophilic interfaces [24]. Hydrophilicity is the property of a material to absorb or attract water molecules. It has also been claimed that in regime I (1–40% RH) no capillary neck is developed, and the adhesion force is dominated by van der Waals interactions [24]. A capillary neck is formed at about 40% RH and here the adhesion force is a superposition of van der Waals and capillary force. It can be seen from Figure 2.6 that in regime II (40–70% RH) the adhesion force increases with increasing RH. In regime III (70–100% RH) the adhesion force decreases with increasing RH. This decrease is due to the screening of the van der Waals force due to the presence of water in the gap [7].

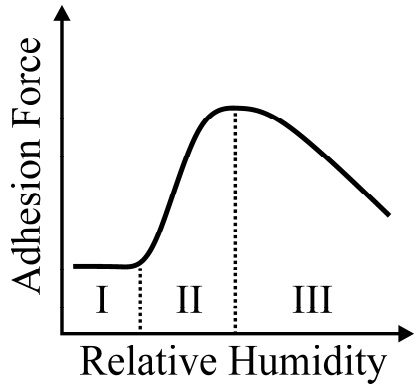

Figure 2.6: Generic sketch of the relationship between the adhesion force and relative humidity. Regimes I, II and III represent the van der Waals regime, superposition of van der Waals and capillary regime and capillary regime decreased by repulsive force due to chemical bonding, respectively [24].

2.2.2.1 Influence of surface roughness

The surface roughness of the contacting interfaces also plays a very vital role in developing the capillary force. Eq. (2.18) is valid for relatively smooth surfaces with rms roughness of < *3 nm* [9]. For rough surfaces (rms roughness > *6 nm*) in contact the nanosize capillary bridges are formed with a radius of about *50 nm* [9]. The capillary force is larger than the van der Waals/ Casimir and/or

electrostatic force for smooth surfaces [25]. If the rms roughness is increased a few nanometers in the range *1–10 nm*, the capillary force decreases considerably by more than two orders of magnitude [25]. Similarly, the value of the adhesion force as a function of rms roughness has been reported to be decreasing by a factor of *5* if the rms roughness is increased from *0.2–4 nm* and for higher roughness values it stabilizes [8, 26].
In another study, the adhesion force is decreased to a factor of *5* if the rms roughness of the glass sphere is changed from *0.17 nm* to *1.6 nm* [27]. However, using the same rms roughness of an AFM tip the adhesion force decreases by a factor of *1.5* [27]. In [1] the calculated adhesion force values as a function of RH and rms roughness have been shown. The transitions in the adhesion force as shown in Figure 2.6 have been reported with experimental data in [2-4, 6, 24]. The experimentally reported data is in contrast with the calculated results in [1], where no transitions follow the modelling effects. It was also reported that at low normal load, for a rough sphere, the sphere makes contact with multiple nanosized asperities. This leads to a significant decrease in the adhesion force as compared to an atomically smooth sphere [24]. It was also shown that the adhesion force is influenced by the rms roughness of different materials of different degrees of hydrophilicity. In other words, the rms roughness for less hydrophilic materials does not significantly influence the adhesion force, whereas for more hydrophilic materials it increases with increased roughness [9]. Therefore, we can say that the influence of roughness on the adhesion force is material dependent.

2.2.2.2 Influence of contact time

The contact time is defined as the time for which the surfaces under consideration are in contact with each other. It should also be mentioned here that the typical time of capillary condensation is dependent on the size of the sphere radius. It was shown that the typical bridge stabilization time is *1s* for a sphere radius of *400 nm* and for a sphere radius of *50 nm* the bridge stabilization time is much smaller i.e. *5 msec* [23]. Similarly, the stabilization times for a *100 μm* sphere is reported to be in the order of *100 sec* [9] which is in contrast with the stabilization times predicted in the model explained in [11].

2.3 Adhesion force–Contact mechanics

When two solid bodies have been pressed together under applied load, a normal force is generated at the contact surfaces. In many cases, however, the contact holds even if the applied normal force has reached zero, which means that to pull the two surfaces apart an additional tensile force, usually defined as negative in value, has to be applied. This phenomenon, known as *pull–off*, is a

manifestation of adhesion. This force is generally caused by the superposition (expressed in Eq. (2.23)) of different kinds of surface forces like van der Waals forces, electrostatic forces, capillary forces and other interacting surface forces, which are explained in the previous chapter.

$$F_a = F_{vdw} + F_c + F_{el} + \ldots \tag{2.23}$$

Where, F_a is adhesion force, F_{vdw} is van der Waals force, F_c is capillary force and F_{el} is electrostatic force. Furthermore, these forces may contribute to the additional deformation in the contact area. In this section different contact mechanics models with and without adhesion for single asperity contact will be discussed.

2.3.1 Hertz theory

The classical relationship derived by Hertz can be used to predict the elastic deformation in point contacts [28]. At high normal loads the contact area closely fits with this model but the model fails to predict the area of contact at very low or zero normal load [29]. Nevertheless, the Hertzian model does not consider the dependence of adhesive forces on the contact area [7, 18]. If we have an elastic contact between a sphere of radius R and a flat surface as shown in Figure 2.5, the contact area with radius a is given by [30]:

$$A = \pi\left(\frac{3}{4}\frac{R}{E^*}\right)^{2/3} F_N{}^{2/3} \tag{2.24}$$

$$\frac{1}{E^*} = \left(\frac{1-\nu_{ps}^2}{E_s} + \frac{1-\nu_{pf}^2}{E_f}\right) \tag{2.25}$$

Where, E^* is equivalent Young's modulus of sphere and plane E_i *(i = s, f)* and v_{pi} is Poisson's ratio. From Eq. (2.24) it can be seen that $A \propto F_N{}^{2/3}$ which is in contrast with the typical behaviour of random rough surfaces where $A \propto F_N$ [31]. In real situations the surfaces in contact were found to adhere, i.e. under load the contact area exceeded that predicted by the Hertz theory. Also, a contact area of finite size was seen at zero loads and a tensile force was required to pull the surfaces apart.

2.3.2 JKR, DMT and M-D theory

There are different theories for the adhesion and separation of a spherical elastic contact under the action of purely normal forces. Adhesion between rigid spheres where the surface forces are governed by the Lennard–Jones potential, which gives the force–separation relation, was analysed by Bradley in 1932 [32, 33]. Corresponding theories taking elastic deformation into account were presented by Johnson, Kendall & Roberts (JKR) in 1971 and by Derjaguin, Muller & Toporov (DMT) in 1975 [33]. A model of the adhesion force developed by Bradley for rigid sphere against flat is given as [32]:

$$F_N = -\frac{8\pi W_{12} R}{3}\left[\frac{1}{4}\left(\frac{z}{z_0}\right)^{-8} - \left(\frac{z}{z_0}\right)^{-2}\right] \tag{2.26}$$

Where, z_0 is the equilibrium separation in the Lennard–Jones potential. At this distance, the attractive and repulsive interactions cancel each other out. The work of adhesion W_{12} is given by [7]:

$$W_{12} = \gamma_1 + \gamma_2 - \gamma_{12} \tag{2.27}$$

Here, γ_1 and γ_2 are the surface energies of the two materials in contact and γ_{12} is the interfacial energy between the two materials. Considering only dispersion forces responsible for the interaction between two solid materials, the work of adhesion can be approximated by [7, 18]:

$$W_{12} = 2\sqrt{\gamma_1 \gamma_2} \tag{2.28}$$

For two similar solid surfaces in contact, the work of adhesion is given as:

$$W_{12} = 2\gamma_1 \tag{2.29}$$

The corresponding pull–off force occurs when $z=z_0$ and is given by:

$$F_a = 2\pi W_{12} R \tag{2.30}$$

A modified Hertz model was developed to account for attractive surface forces in lightly loaded contacts by Johnson, Kendall and Roberts [29]. The Johnson–Kendall–Roberts (JKR) model describes the effect of strong short–range interactions between materials with relatively low elastic modulus and large radius of curvature [18, 34]. This model shows that there is a finite contact area

between surface under zero normal load and it also predicts that there is an external force required to separate two bodies of given surface energies and geometry [29, 30]. Eq. (2.24) is modified according to the JKR model as follows [30]:

$$A_{(JKR)} = \pi\left(\frac{3R}{4E^*}\right)^{2/3}\left(F_N + 3\pi W_{12}R + \sqrt{6\pi W_{12}RF_N + (3\pi W_{12}R)^2}\right)^{2/3} \quad (2.31)$$

The JKR model assumes that the adhesive forces are confined inside the contact area and thus give the pull–off force [18, 32]:

$$F_a = 1.5\pi W_{12}R \quad (2.32)$$

The surface energy γ or work of adhesion W_{12} can be measured using the theory of JKR in two ways. First, it can be measured using Eq. (2.32), if the adhesion force or pull–off force, F_a, needed to separate two surfaces from a contact is known. Eq. (2.31) also shows that two solids continue to adhere even under negative loads ($F_N < 0$) but the surfaces separate spontaneously once F_N reaches the pull–off force (F_a) given by Eq. (2.32) [35]. The JKR model reduces to the Hertzian model at high loads. One of the limitations of the JKR and Hertz theories is that they assume perfectly smooth surfaces. Most practical surfaces are rough having asperities as small as 1–2 nm. This can lower the adhesion significantly, but there is no satisfactory theory for such a contact yet [7].
In contrast to JKR the Derjaguin–Muller–Toporov (DMT) model depicts the effect of long–range interactions between materials with high elastic modulus and small radius of curvature [18, 34]. The contact area for the DMT model can be calculated with the following expression:

$$A_{(DMT)} = \pi\left(\frac{3R}{4E^*}\right)^{2/3}\left(F_N + 2\pi W_{12}R\right)^{2/3} \quad (2.33)$$

The DMT model assumes that the adhesive forces act outside of the contact area and predicts that the pull–off force or adhesion is given as [18, 32]:

$$F_a = 2\pi W_{12}R \quad (2.34)$$

A dimensionless parameter μ_T, called the Tabor parameter representing the ratio between the gap outside the contact zone and the equilibrium distance between atoms has been presented in [36]. In mechanical terms, this parameter represents the ratio of the magnitude of the elastic deformation to the range of

adhesive forces. This parameter established the range of applicability of the two models and suggested that the JKR and DMT models are at the limiting cases of μ_T.

$$\mu_T = \left(\frac{RW_{12}^2}{E^{*2} z_0^3} \right)^{1/3} \tag{2.35}$$

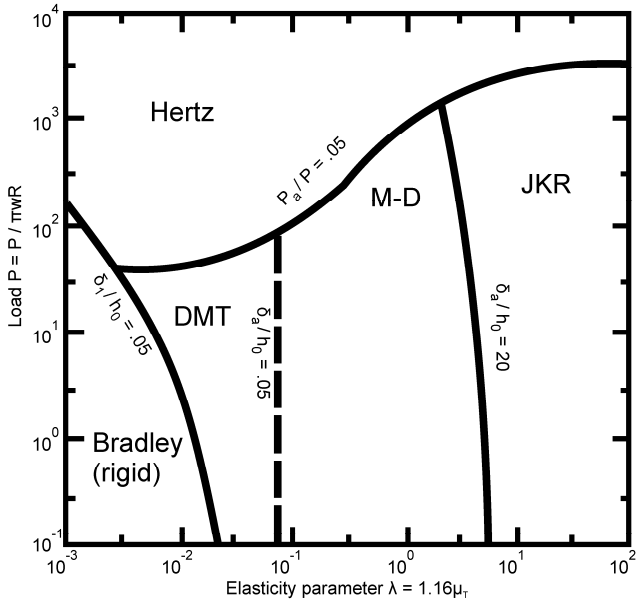

Figure 2.7: Adhesion map for elastic spheres based on the Maugis–Dugdale model. In the Hertz zone adhesion forces are negligible. The Bradley, DMT and JKR asymptotic theories may be used in the zones as marked [34].

Maugis [37] provided a solution to the contact problem with interactions inside and outside the contact zone using the Dugdale approximation (constant adhesive stress outside the contact zone) and is known as Maugis–Dugdale (M–D) model. The M–D model showed the transition of a contact problem from DMT to JKR as two opposite ends of a continuous spectrum based on a parameter λ (the Maugis parameter), which is equivalent to the Tabor parameter *($\lambda = 1.16\mu_T$)*. An adhesion map (cf. Figure 2.7) has been reported by Johnson and Greenwood [34, 38] based on the Maugis model. If $\lambda > 5$, the JKR analysis becomes appropriate and when $\lambda < 0.1$, the DMT model is applicable. In the intermediate range $0.1 > \lambda > 5$ the Maugis model has to be applied [30, 32, 33]. The M–D equations are more difficult to utilize, since Maugis' formulation lacks a single expression relating only a and F_N. Eq. (2.36) to (2.39) are needed to solve the M–D model [37]:

$$\frac{\lambda\bar{a}^2}{2}\left\{\left(m^2-2\right)\sec^{-1}m+\sqrt{m^2-1}\right\}+\frac{4\lambda^2\bar{a}}{3}\left\{\sqrt{m^2-1}\sec^{-1}m-m+1\right\}=1 \quad (2.36)$$

$$\bar{P}=\bar{a}^3-\lambda\bar{a}^2\left\{\sqrt{m^2-1}+m^2\sec^{-1}m\right\} \quad (2.37)$$

$$\bar{\delta}=\bar{a}^2-\frac{4}{3}\lambda\bar{a}\left\{\sqrt{m^2-1}\right\} \quad (2.38)$$

Where;

$$\bar{a}\equiv a\left(\frac{4E^*}{3\pi W_{12}R^2}\right)^{1/3};\quad \bar{c}\equiv c\left(\frac{4E^*}{3\pi W_{12}R^2}\right)^{1/3};\quad m=c/a;\quad \bar{P}\equiv\frac{F_N}{\pi W_{12}R};\quad \bar{\delta}\equiv\delta\left(\frac{16E^{*2}}{9\pi^2 W_{12}^2 R}\right)^{1/3}$$

$$\lambda\equiv\sigma_o\left(\frac{9R}{2\pi W_{12}E^{*2}}\right)^{1/3} \quad (2.39)$$

In these equations, a is the radius of the contact and c is the radius of the adhesive zone (same as r_2) as shown in Figure 2.5, δ is the deformation, λ and σ_o are the Maugis (elasticity) parameter and constant adhesive stress outside the contact respectively. If $\sigma_o = 1.03W_{12}/z_0$ is assumed then $\lambda=1.16\mu_T$.

2.3.3 Modified M-D model incorporating capillary effects

A modified M–D model incorporating the meniscus forces has been developed in [39]. This modification of the model is required since the JKR, DMT and M–D models are assuming solid–solid adhesive contacts where van der Waals forces are dominant. However, if two hydrophilic surfaces are brought into contact with each other under humid environmental conditions the meniscus forces will dominate the adhesive interaction [1, 7]. The M–D model has been modified using the Kelvin and Young–Laplace equation and has been used to calculate the contact areas for dry as well as humid contact conditions. In the analysis, Eq. (2.39) can be used to calculate the Maugis' parameter for a solid–solid (dry) contact, but Eq. (2.39) needs to be modified if the adhesive interaction is due to meniscus forces. A modification in this respect is given in [39], using the Kelvin equation. As explained above, the M–D model used the Dugdale approximation of constant adhesive stress outside the contact. Therefore, the adhesive stress due to capillary formation inside the meniscus is also considered constant. This adhesive stress is the capillary pressure or

Laplace pressure which is given by the Young–Laplace equation [39] (see Eq. (2.17) and Eq. (2.19)):

$$\sigma_o = P_{cap} = \frac{\gamma_L}{r_k} \tag{2.40}$$

Here, r_m is the mean radius of the meniscus, Putting Eq. (2.19), (2.29) and (2.40) in (2.39) we get the modified Maugis parameter λ_{cap} as:

$$\lambda_{cap} = \left(\frac{9R\gamma_L^2}{4\pi E^{*^2} r_m^3} \right)^{1/3} \tag{2.41}$$

$$\lambda_{cap} = \left(-\frac{9RR_g^3T^3\left[\log\left(p/p_s\right)\right]^3}{4\pi E^{*^2} V_m^3 \gamma_L} \right)^{1/3} \tag{2.42}$$

2.4 Mechanics of friction force

When a lateral force is applied to move a body in contact with another body, the resistance in this relative motion is termed as friction. The magnitude of this opposing force is dependent on the applied normal load and is defined as:

$$F_f = \mu_f \cdot F_N \tag{2.43}$$

Where, F_f is the friction force, μ_f is the coefficient of friction (COF). The COF is strongly affected by the physical and chemical characteristics of the contacting surfaces. The coefficients of friction have been reported between countless couples of materials under different conditions, from liquid ambient to ultra–high vacuum. In the case of dry contacts, friction is generally divided into two components such as ploughing and adhesive component. The ploughing component is present if plastic deformation of the surfaces is expected. However, the adhesive component plays an important role if the surfaces are subjected to low applied normal loads. In this study the ploughing component of dry friction is neglected since the loads and normal pressures are kept well within the elastic limits of the surfaces in contact.

2.4.1 Friction laws and static friction

Leonardo da Vinci first gave the laws of friction, which were then published by Guillaume Amontons and Charles Augustin Coulomb. These classical friction laws state that:

1. The force of friction is directly proportional to the applied load.
2. The force of friction is independent of the apparent area of contact.
3. The kinetic friction force is independent of the sliding velocity.

Recently, with the research focusing on micro and nano domain with a variety of materials like ceramics and polymers, experiments show that these laws are only applicable to the macro domain with classic materials. For instance, the coefficient of friction for polymers and ceramics is sometimes found to decrease with the increase in the normal load; this is in contradiction to the first law. Similarly, the third law also fails when polymers are involved in the contact. In the case of micro and nano experiments these laws are not obeyed and the system is dominated by adhesion-influenced contact mechanics [40]. On a microscopic scale every surface is rough. If two surfaces are brought into contact, only their asperities touch each other, and the real area of contact is a few orders of magnitude smaller than the apparent area of contact [30].

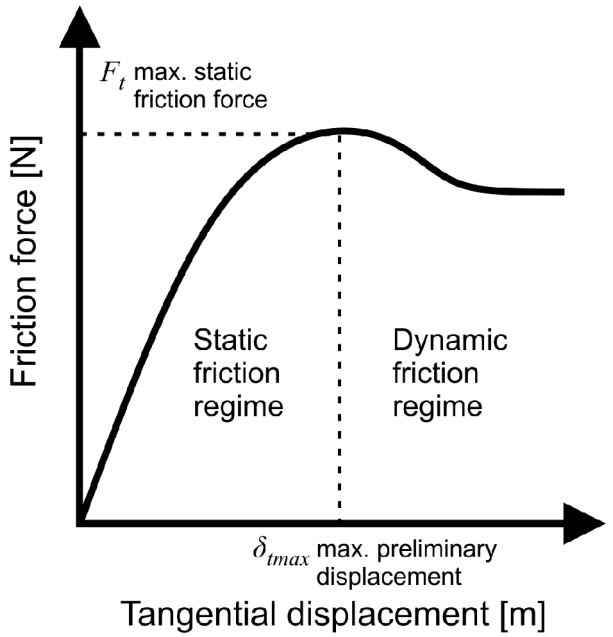

Figure 2.8: A force-displacement curve showing the friction force against tangential displacement. The static and dynamic friction regions are also shown.

The friction force is divided into two regimes, *static* and *dynamic* friction as schematically shown in Figure 2.8. When a tangential load is applied to one surface, in contact with another, the surface starts to slip. However, there is evidence that at the start of the motion there is always a small lateral displacement between the interacting surfaces before full or gross slip occurs [14, 15, 41]. The regime before the start of gross slip is called the static friction regime and the one after the gross slip is called the dynamic friction regime. The maximum tangential force required to slide the surface is called *maximum static friction force* and the corresponding lateral displacement is called *maximum preliminary displacement*. The ratio of static friction force and the applied normal load is termed as the *coefficient of static friction (COSF)*. Experiments show that static friction is somewhat greater than dynamic friction as shown in Figure 2.8.

In 1950 Bowden and Tabor presented their model of friction [30, 33]. When a finite normal load F_N is applied on the sphere there is elastic and/or plastic deformation in the system. If the deformation is fully plastic, Amontons' law is obeyed: $F_f = \mu_f \times F_N$ where, F_f is proportional to real contact area A, and the shear strength τ: $F_f = \tau \times A$. Similarly, when there is plastic deformation the contact pressure reaches a certain yield pressure $p=H$ (also called hardness of the material) when a normal force F_N is applied: $F_N = H \times A$. This gives us $\mu_f = \tau/H$ which is a constant and is independent of contact area [30]. However, if we have elastic deformation the real contact area is not the same as with plastic deformation. The model proposed by Bowden and Tabor has been regarded as the most successful one for presenting a simple and logical theory capable of explaining Amontons' friction law [30, 42]. However, over the past few years reservations concerning the two fundamental assumptions in the model have been gradually raised. Friction has been attributed, in Bowden and Tabor's model, to the adhesion between asperities in contact and torn–off of the adhesive junctions when the shear stress exceeds a critical value. This implies that plastic flow and surface destruction may occur at the moment of slip, and that friction is dominated by the shear strength of the adhesive contact, which is material dependent. However, fully plastic deformation during sliding provokes huge damage in a short time, which usually is not observed [30, 42]. The energy losses due to friction are mostly converted into heat, and only a small part contributes to the material damage and wear. It has been frequently observed in practice that friction exists or remains quite high sometimes, even when the wear rate is very small or nearly zero [42]. This provides evidence that the elastic processes also have an important role in contact mechanics and friction. In this study, the focus will be on the elastic deformation of the contact since low applied contact pressures are chosen.

2.4.2 Static friction force

Many static friction models have been presented in the literature. The influence of different parameters, like material combination, deformation, contact pressure, roughness and contact time, has been studied. The value of static friction typically increases as the two surfaces stay in stationary contact for a longer period of time [5]. This increase in static friction is because of increase in the contact area [5]. The increase in contact time will affect the adhesion and consequently the COSF. However, the COSF can either decrease or increase with increasing contact time [43]. This increase or decrease in the COSF is dependent on the contamination and cleanliness of the contact. If the low shear stress elements contaminate the contact, then the COSF decreases with the increase in contact time. On the other hand, if the contact is clean then the interfacial bonding between the surfaces will increase and as a result the COSF increases with the contact time [43].

Catteneo and Mindlin have studied the partial stick and slip behaviour for an elastic single asperity contact. In 1938, Cattaneo studied the partial slip regime for an elliptical Hertzian contact area, where firstly a constant normal load is applied and then the tangential force is increased [28]. A few years after, Mindlin [14] and Mindlin together with Deresiewicz [15] extended this problem to different loading conditions. They assumed that by varying the normal and the tangential loads the changes in tangential traction and displacements can be seen. The tangential loading problem is often referred to as the Cattaneo-Mindlin problem [28]. Interaction between bodies under tangential displacement was also studied by Johnson [28, 44] and Ciavarella [13]. Johnson investigated the preliminary displacement between a hard steel ball and the flat end of a hard steel roller under the action of steady and oscillating tangential forces lower than the static friction force. The results of the experiments were in good quantitative agreement with the Mindlin theory.

Mindlin theory was developed for two elastic bodies in contact under a certain applied normal load and also loaded with a tangential load. When a normal load F_N and a tangential load is applied on a ball and flat contact as shown in Figure 2.9(a), the preliminary displacement and the tangential traction is produced. As the tangential load is increased the preliminary displacement is increased until the ball is in the full slip regime. The top view of the contact is also shown in which the area of the stick zone decreases with the increase of tangential load. Similarly, by the decrease of the stick area the annulus of slip is increasing until the ball is in the full slip regime. If it is assumed that there is no slip between the ball and a flat, the distribution of the shear stress goes asymptotically to infinite at the boundary of the contact. However, in practice this is not the case, so this infinite shear stress has to be relieved in some way. Therefore, this

infinite shear stress is relieved in the slipping of the surfaces over an annulus of slip as shown in Figure 2.9(b).

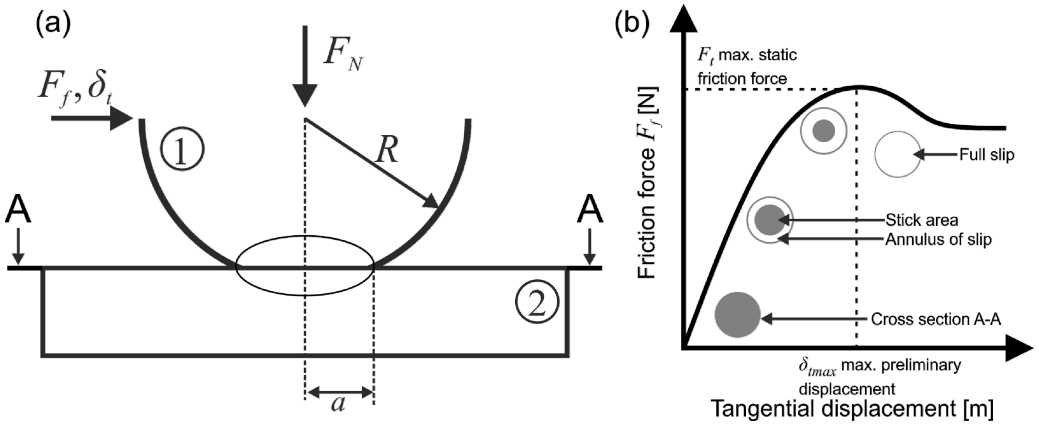

Figure 2.9: (a) A ball in contact with a flat surface loaded with normal load F_N and tangential load F_f. (b) A force-displacement curve showing the friction force against tangential displacement. The top view of the contact area shows the stick area and the annulus of slip.

For a ball in contact with the flat as shown in Figure 2.9(a), according to Hertz [28] the circular area with contact radius a can be calculated. The preliminary displacement δ_t at any instance, when constant applied normal load F_N is applied, can be calculated as [15]:

$$\delta_t = \frac{3 \cdot \mu \cdot F_N}{16 \cdot a \cdot G^*} \left[1 - \left(1 - \frac{F_f}{\mu \cdot F_N} \right)^{2/3} \right] \tag{2.44}$$

Where μ is coefficient of static friction, G^* is reduced shear modulus, a is the contact area and F_f is applied tangential load. Eq. (2.44) shows that the preliminary displacement is dependent on the material properties, applied normal load, applied tangential load, coefficient of friction and contact radius. The shear stress at a particular value of the contact area for the stick and slip zones when the tangential load is increasing is given by [15, 28]:

$$\tau(r) = \begin{Bmatrix} 3 \cdot \mu \cdot \dfrac{F_N}{2 \cdot \pi \cdot a^3} \cdot \left(a^2 - r^2 \right)^{1/2} & \text{if } s \le r \le a \quad \text{Slip} \\ 3 \cdot \mu \cdot \dfrac{F_N}{2 \cdot \pi \cdot a^3} \cdot \left[\left(a^2 - r^2 \right)^{1/2} - \left(s^2 - r^2 \right)^{1/2} \right] & \text{if } 0 \le r \le s \quad \text{Stick} \end{Bmatrix} \tag{2.45}$$

Eq. (2.45) is used to calculate the tangential traction $\tau(r)$ when the ball-flat contact is loaded with a certain normal load F_N and the tangential load ($\mu \times F_N$) is increased. Here, a is the contact radius shown in Figure 2.9(a), s is the radius of the stick zone and r is the instantaneous value of the radius defined in Eq. (2.45).

2.5 Summary

In this chapter, basic physical principles and mechanisms of adhesion and static friction force were discussed. Different types of important surface forces responsible for contributing to the adhesion force were discussed in detail. The dispersion force is always present between different material combinations. The dispersion force is termed as a short-range surface force and it is being retarded as the separation distance is increased. The Casimir force is a relatively long-range surface force and is indeed a retarded dispersion force. Analytical expressions have also been discussed to calculate these forces. The capillary force, if present, is the dominant surface force over the dispersion and the Casimir forces. They are also considered as long-range surface forces. The RH dependence of capillary force was briefly explained and it can be seen that for hydrophilic materials the capillary force is not independent of RH. The surface roughness and the contact time also influence the capillary force. By increasing the rms roughness the capillary force decreases and with the increase in contact time the capillary force increases.

Different contact mechanics theories were briefly elaborated considering the adhesion force. JKR, DMT and M-D models were discussed and it was shown that these models only incorporate deformation of the contact. A modified M-D model incorporating the capillary force has been discussed and the analytical expressions for solving this model were explained.

The mechanics of the friction force and specially the static friction force has also been elucidated. The parameters of the static friction regime are defined in terms of static friction force, coefficient of static friction, preliminary displacement and maximum preliminary displacement. The Mindlin theory was regarded as the suitable model to explain the pre-sliding and the static friction behaviour.

Adhesion behaviour in different environmental conditions has been reported in the literature. However, it is not always clear which surface is dominant under certain conditions. Similarly, the friction behaviour and specially the static friction and stick-slip phenomenon is not very well understood. Moreover, the influence of adhesion on static friction and vice versa is not available in the literature.

Chapter 3
EXPERIMENTAL SETUP, MATERIALS AND PROCEDURES[1]

To study the behaviour of adhesion and friction for a single asperity contact in high vacuum (HV) conditions in comparison to ambient conditions, a novel test setup was designed and manufactured. There were several reasons to design a complete new test setup to study adhesion and friction. Atomic Force Microscope (AFM), Friction Force Microscope (FFM) and Surface Force Apparatus (SFA) are some of the examples which have contributed to the understanding of adhesion and friction at nanoscale, see Israelachvili [7]. However, the AFM is used for adhesion and friction measurements typically with nanometre sized tips and normal load of a few hundreds of nano-Newtons. On the other hand, SFA is used to measure the adhesion forces with smooth surfaces with typical tip radius of 1 cm, see Israelachvili [7]. The use of nanometre-sharp AFM tips in friction measurements hinders the quantitative comparison between the experimental data and the contact model calculations for elastically deforming interfaces, see Grobelny et al. [3]. Secondly, to the best of our knowledge there is no commercial test setup available that can measure adhesion and friction on micro scale in ambient as well as in high vacuum conditions. Furthermore, a custom-made setup gives more liberty to adapt to different kinds of measurements.

The main aim of this setup is to perform adhesion and friction measurements at micro scale in ambient (*20°C*, *1 bar* and *50%* Relative Humidity (RH)) as well as in special environments like HV (*20°C* and 10^{-6} *mbar*) and dry nitrogen. The complete assembly of the Vacuum Adhesion and Friction Tester (VAFT) along with the placement of vacuum pumps and chamber is shown in Figure 3.1. A stainless steel vacuum chamber collar with total *8* ports is used with *4 100CF* and *4 40CF* flanges. The diameter of the chamber is *450 mm* with the thickness of *150 mm*. The vacuum chamber consists of three main parts. The first is the collar with *8* ports and a vertically fixating support. The second is the back plate on which the VAFT is mounted and this back plate is supported by a linear guiding (rails). The rails are used to provide easy access for assembling

[1]Reproduced from: M.A. Yaqoob, M.B. de Rooij and D.J. Schipper, Design of a Vacuum Based Test Rig for Measuring Micro Adhesion and Friction Force, *High performance structures and materials*, VI, pp. 261-274, 2012.

and disassembling the VAFT. The third is the front-hinged door with a viewport. It is used to provide easy access for changing samples.

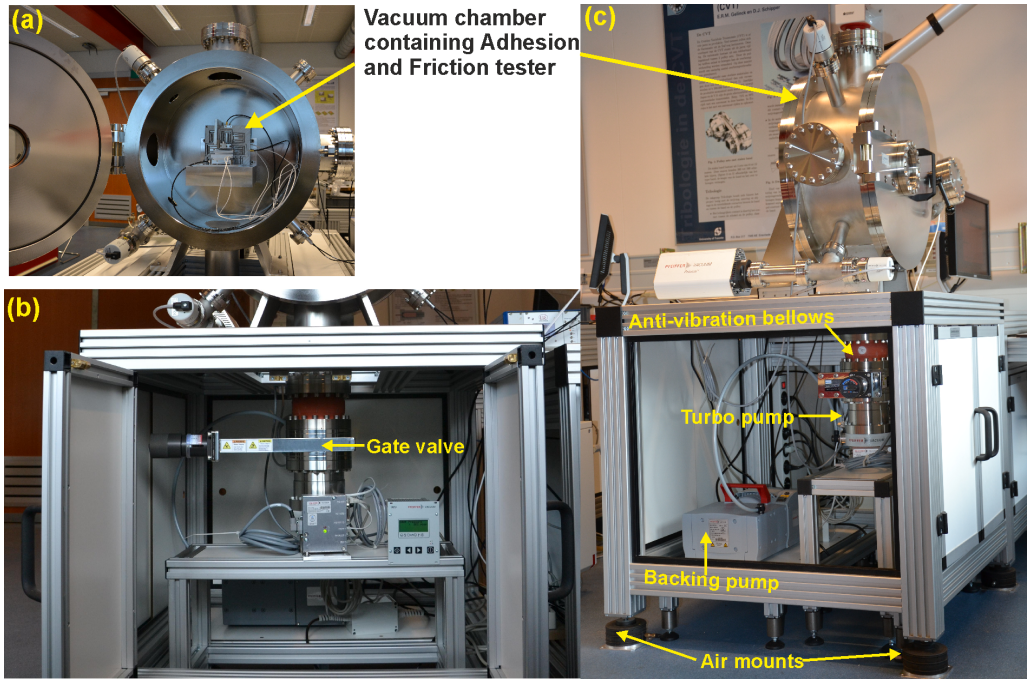

Figure 3.1: (a) Adhesion and friction tester mounted inside the vacuum chamber. (b) Mounting and placement of vacuum pumps and vacuum chamber. (c) Description of components mounted to reduce vibrations.

Mechanical disturbances are the major potential source of instability and inaccuracy in the system. These disturbances are mainly categorized as ground vibrations, vibrations from the vacuum pump and vibrations induced due to dynamic effects of the moving Z positioning stage. The ground vibrations are caused by the traffic around the lab and the structural vibrations of the building. A three-step vibration isolation and damping technique has been used in this setup to reduce the impact of mechanical disturbances. First, the backing pump, turbo pump and the vacuum chamber are placed on three different platforms. These platforms will help to isolate the vibrations from the backing pump and turbo pump. The pump is attached to the bottom flange of the chamber with an anti-vibration bellows as shown in Figure 3.1(c). These specially designed bellows are used to dampen the vibrations transferred from the turbo pump to the vacuum chamber. The manufacturer's specifications of reduction in the vibration amplitudes by using these bellows is by a factor of 10 [45]. Secondly, all the platforms have damping pads and air mounts under their feet, as shown in Figure 3.1(c), which will also help to reduce the disturbances from ground vibrations. Thirdly, introducing an eddy current damper diminishes the

vibrations induced by the Z positioning stage. The principle of eddy current damper will be explained in detail in section 3.1.
An inline gate valve is also used between the turbo pump and the anti-vibration bellows as shown in Figure 3.1(b). This valve will be used to maintain the desired vacuum and to perform tests after the vacuum pump is turned off. This will help to figure out the effects of vibrations from the pump on the measurements. The other flanges are used to provide feedthroughs for linear stages, capacitive sensors and dry nitrogen. The vacuum level in the chamber is measured using a pirani/cold cathode transmitter and the partial pressure of the gases present in the vacuum chamber in high vacuum is measured using a mass spectrometer.

3.1 Vacuum adhesion and friction tester (VAFT)

The VAFT comprises three positioning stages and two capacitive sensors along with a force measuring mechanism as shown in Figure 3.2(a). The setup has a ball on flat configuration and represents a single asperity contact. The ball is mounted on the sample holder and the sample holder along with the force measuring mechanism (FMM) is mounted on one of the positioning stages, which can move in Z direction (not visible in Figure 3.2(a)). This positioning stage is used to make contact with the flat surface and to apply the normal load. The flat surface is placed on an XY stage. The X positioning stage is used to apply a tangential displacement for friction force measurements. The accuracy of both X and Z stage is *20 nm* with a stroke of *20 mm*. The Y stage is used to perform multiple parallel measurements on the flat surface and has a stroke of *20 mm* as well.
The measuring range of the capacitive sensors is *50 μm* with an accuracy better than *1 nm*. The capacitive sensors are mounted on the FMM and are used to measure the deflection in the FMM in X and Z directions. The stiffness of the FMM is calibrated, and then the force can be calculated by measuring the deflection of this mechanism with the help of capacitive sensors. The maximum applied normal load with this setup is *100 mN* with an accuracy of *8 μN*.
A permanent magnet was placed near the indenter that has been mounted on the aluminium beam as shown in Figure 3.2(a). The magnet used is a rare earth metal magnet NdFeB. These magnets are considered to be one of the strongest magnets available. This beam is mounted on the FMM and the whole assembly was mounted on the Z-axis positioning stage. As described earlier, the dynamic effects of the positioning stage will induce disturbances to the FMM and these disturbances need to be reduced to get the desired accuracy of the force signal.
There are many methods of adding damping to a vibrating structure; however, very few can function without coming into contact with the structure. One such

method is eddy current damping (ECD). This magnetic damping method functions through the eddy currents that are generated in a nonmagnetic conductive material when it is subjected to a time-changing magnetic field. The magnitude of the magnetic field on the conductor can be varied through movement of the conductor in a stationary magnetic field, by movement of a constant intensity magnetic source or by changing the magnitude of the magnetic source with respect to a fixed conductor, see Sodano et al. [46]. The schematic concept of the ECD is shown in Figure 3.2(b).

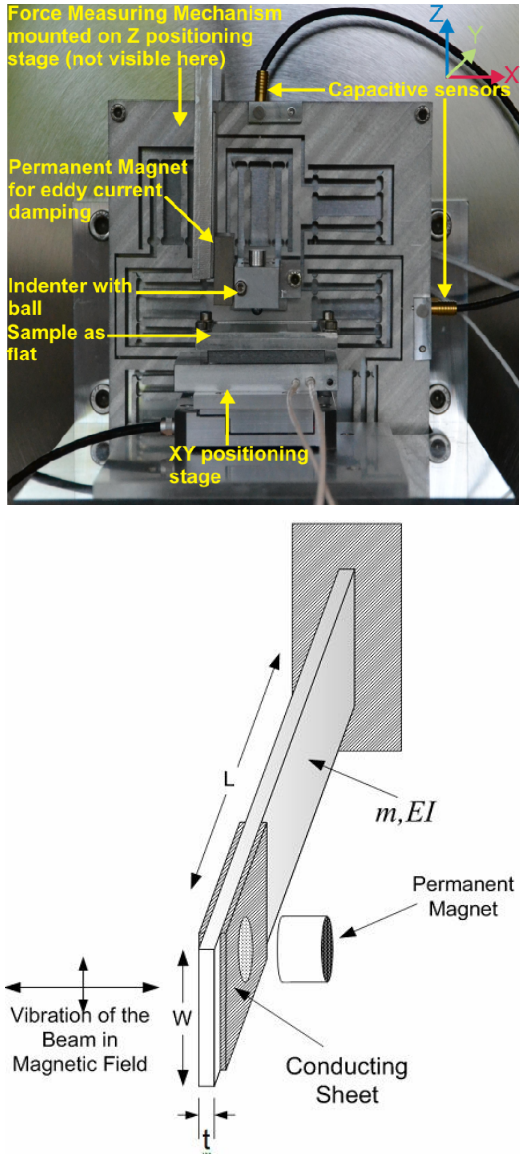

Figure 3.2: (a) An internal view of VAFT showing all the components. (b) Schematic representation of eddy current damping on a vibrating beam, Sodano et al. [46].

Once the eddy currents are generated, they circulate in such a way that they induce their own magnetic field with opposite polarity of the applied field causing a resistive force. However, due to the electrical resistance of the conducting material, the induced currents will be dissipated into heat at the rate of I^2R. In the case of a dynamic system, the conductive metal is continuously moving in the magnetic field and experiences a continuous change in flux that induces an electromotive force (emf), allowing the induced currents to regenerate [46]. The process of the eddy currents being generated causes a repulsive force to be produced that is proportional to the velocity of the conductive metal. Since the currents are dissipated, energy is being removed from the system, thus allowing the magnet and the conductor to function like a viscous damper. The eddy current damper consists of a permanent magnet and a conducting metal. The important advantage of the proposed eddy current damper is that it does not require any electronic devices and external power supplies, see Bae et al. [47]. The most useful property of an eddy current damper is that it forms a means of removing energy from the system without ever contacting the structure. This means that unlike other methods of damping, such as constrained layer damping, the dynamic response and material properties are unaffected by its addition into the system.

The vibrations from the beam in X and Z directions form a dynamic system where the nonmagnetic conducting beam is moving in the stationary magnetic field. This movement will cause the eddy current to flow in the beam and thus will generate an opposing magnetic field around the beam. A combination of these two opposing magnetic fields will form a viscous damper.

Measurements were performed to see the effect of ECD on our system as shown in Figure 3.3. The measurements were performed in vacuum with and without the magnet placed near the beam. The reason for performing these measurements in the vacuum conditions is because the Z positioning stage induces amplified disturbances to the system in vacuum conditions as compared to ambient conditions. This is the characteristic of the positioning stage as was described by the manufacturer due to a difference in the friction coefficient of the piezo actuators when operated in vacuum.

The measurement signal between the applied vertical displacement and the measured vertical deflection of the FMM is shown in Figure 3.3. The measurement graph can be separated into two parts, first when the ball makes and breaks the contact (the horizontal lines) and the second, when the ball is in contact with the flat surface (linear part). The insets in both Figure 3.3(a) and Figure 3.3(b) show the zoomed-in area of the measurement graph when the ball snaps onto the flat surface. The magnetic damping is seen to be effective as can be seen in insets of Figure 3.3. The variations in the signal are at the resonance frequency of the elastic hinge mechanism, which is around 25-28 Hz, as can be seen in the insets of Figure 3.3. In Figure 3.3(a) the measurement without the

magnet is shown and the variation in the loading signal (green) is approximately *8 nm*. By contrast, in Figure 3.3(b) the measurement with the magnet is shown and it can be seen that the variations in the loading signal (green) are approximately *2 nm*. Therefore, from these results it can be concluded that the ECD has reduced the high frequency variations approximately *4* times. ECD shows some promising results in our system and it has been used to increase the accuracy of the system. Using ECD, the accuracy in the measurement of displacements is around *2 nm* in vacuum. Given the stiffness of the mechanism, this corresponds to a force of *8 μN*.

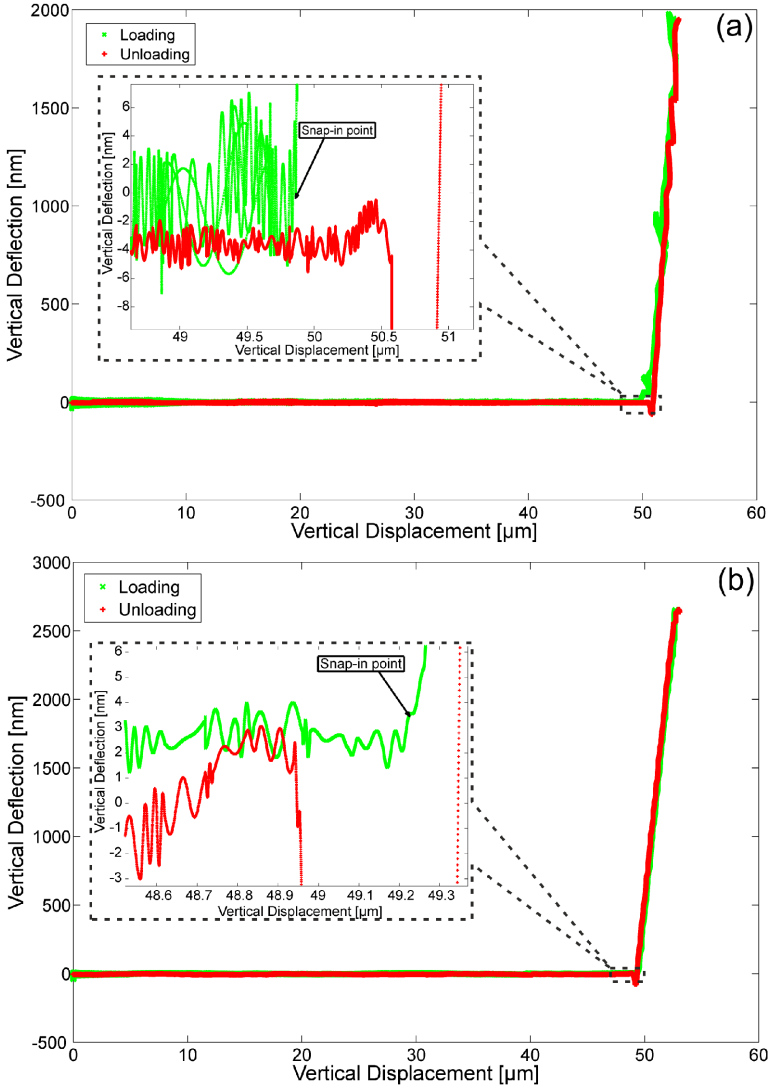

Figure 3.3: Effect of ECD on the measurements performed in vacuum (a) without magnet and (b) with magnet.

3.2 Force measuring mechanism (FMM)

The heart of the VAFT is the force measuring mechanism (FMM). The mechanism is designed to have two DOFs for measuring the normal and the friction force. The conceptual design of this mechanism was explained by Awtar et al. [48]. It was required to have a mechanism that can measure the two perpendicular forces independently as much as possible. The mechanism consists of 8 compound parallelogram frictionless hole–hinge flexure mechanisms.

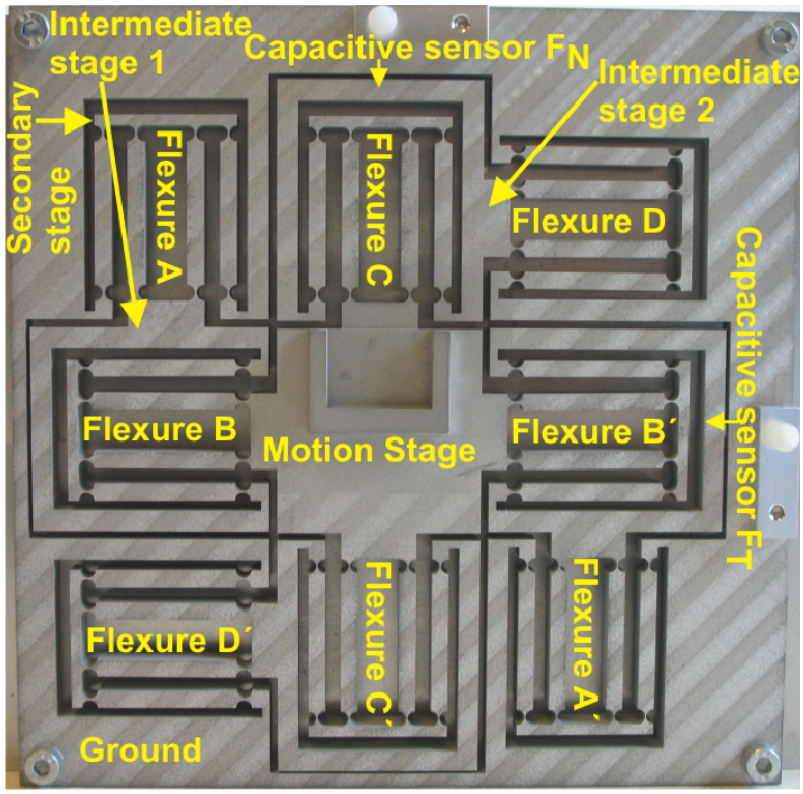

Figure 3.4: Detailed illustration of the force measuring mechanism (FMM) showing different compound parallelogram flexure hinges.

In the mechanism, there are four rigid stages: ground, motion stage, and two intermediate stages as shown in Figure 3.4. The intermediate stages are necessary to decouple and isolate the motion of the two axes. The four compliant units are called Flexure A, B, C and D and their respective mirrored compliant units are Flexure A´, B´, C´ and D´. When the normal force is applied the Flexure B, B´ and D, D´ would bend to give the desired displacement and Flexure A, A´ and C, C´ are in tensile/compressive load.

Similarly, when the lateral force is applied Flexure A, A′ and C, C′ deflects to give the desired motion and Flexure B, B′ and D, D′ are in tensile/compressive load. Any parasitic errors due to bending of compound flexures are compensated by the secondary motion stage. Furthermore, this force measuring mechanism is relatively insensitive to thermal disturbances and manufacturing errors due to its symmetry.

The FMM was calibrated and the stiffness of the mechanism was calculated. Different calibrated masses were placed to apply the load on the FMM and the corresponding deflection of the FMM was measured. In Figure 3.5 the deflection of the hinges measured by the capacitive sensor on the application of normal load is shown. The calibrated stiffness of the FMM calculated by the slope of the force-displacement curve of Figure 3.5 is *3.75 mN/µm*.

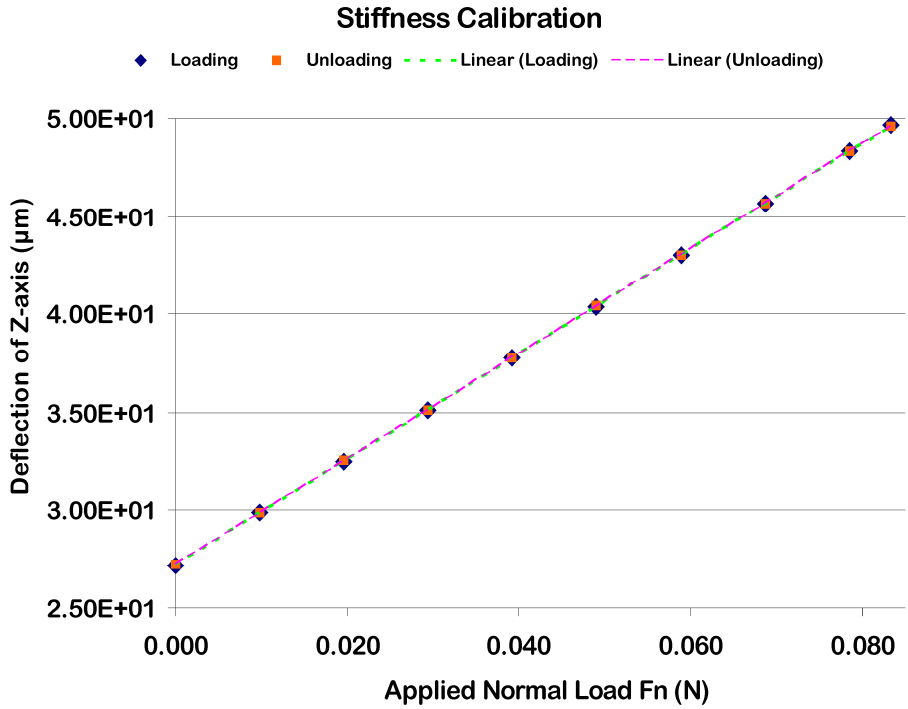

Figure 3.5: Force–displacement curve for calibrating the stiffness of the force measuring mechanism.

3.3 Simulation and analysis of FMM

3.3.1 Analytical static analysis of FMM

The FMM comprises many compound parallelogram flexure mechanisms with hole hinges as flexures, as was explained in the previous section. The static analysis was first analytically performed to calculate the desired stiffness and the dimensions of the hole hinges. The requirement is to have a force resolution of *10 μN* or less considering that the capacitive sensor is capable of measuring the distance with an accuracy of *2 nm*. The building block of this FMM is a hole hinge. The dimensions and the stiffness in weak direction of a hole hinge will be discussed. The material used in this analysis is Aluminium with Young's modulus E_{Al} of *70 GPa* and Poisson's ratio of *0.34*.
The total stiffness of four compound parallelogram flexure mechanisms in one direction is k_{tot}. Thus, if we consider vertical stiffness we can say that this stiffness is the addition of Flexure B, B′, D and D′ since they are in parallel as shown in Figure 3.4.

$$k_{tot} = k_B + k_{B'} + k_D + k_{D'} \tag{3.1}$$

Also,

$$k_B = k_{B'} = k_D = k_{D'} \tag{3.2}$$

Thus,

$$k_{tot} = 4k_B \tag{3.3}$$

It can be seen from Figure 3.4 that each compound parallelogram flexure mechanism consists of *8* hole hinges and the stiffness of each compound parallelogram flexure mechanism k_B is given in terms of stiffness of the hole hinge in adjustable direction k_h as:

$$k_B = \frac{k_h}{2} \tag{3.4}$$

Finally, we can write the total stiffness in terms of k_h as:

$$k_{tot} = 2k_h \tag{3.5}$$

The stiffness values in tensile and shear direction as given in Appendix A and the stiffness of the hole hinge in adjustable direction is given as [49]:

$$k_h = \frac{0.093}{d_l^{\,2}} \sqrt{\frac{t_h}{D_h}} E_{Al} t_h^{\,2} w_h \tag{3.6}$$

Where, t_h is the thickness of the hole hinge, D_h is the diameter of the hole hinge, w_h is the width of the hole hinge and d_l is the distance between two hinges. If we take $t_h = 0.2\ mm$, $D_h = 3\ mm$, $w_h = 7\ mm$ and $d_l = 30\ mm$ we get:

$$k_h = 2.1\,\mathrm{mN/\mu m} \tag{3.7}$$

From here we can compute the total stiffness of the FMM as:

$$\begin{aligned} k_{tot} &= 2k_h \\ k_{tot} &= 4.2\,\mathrm{mN/\mu m} \end{aligned} \tag{3.8}$$

These analytical calculations show that the total stiffness of the FMM in one direction with the above-mentioned dimensions of hole hinges can give the desired force resolution. Now the FEA simulations will be performed to see whether the design has any reasonable discrepancy with the analytical calculations.

3.3.2 Finite element static analysis of FMM

FEA simulations were performed in the CosmosWorks simulation package with SolidWorks. The FMM was designed in SolidWorks with the dimensions mentioned above. A force of *10 mN* is applied in the vertical direction and a mesh control is applied at the circular surfaces of the hinges to refine the mesh in critical areas. The result of this simulation is shown in Figure 3.6. The plot shows a vertical displacement and it can be seen that the maximum displacement with an applied load of *10 mN* is *2.017 μm*. Thus the value of vertical stiffness is *4.95 mN/μm*. This value is close to the calculated value of vertical stiffness as shown above.

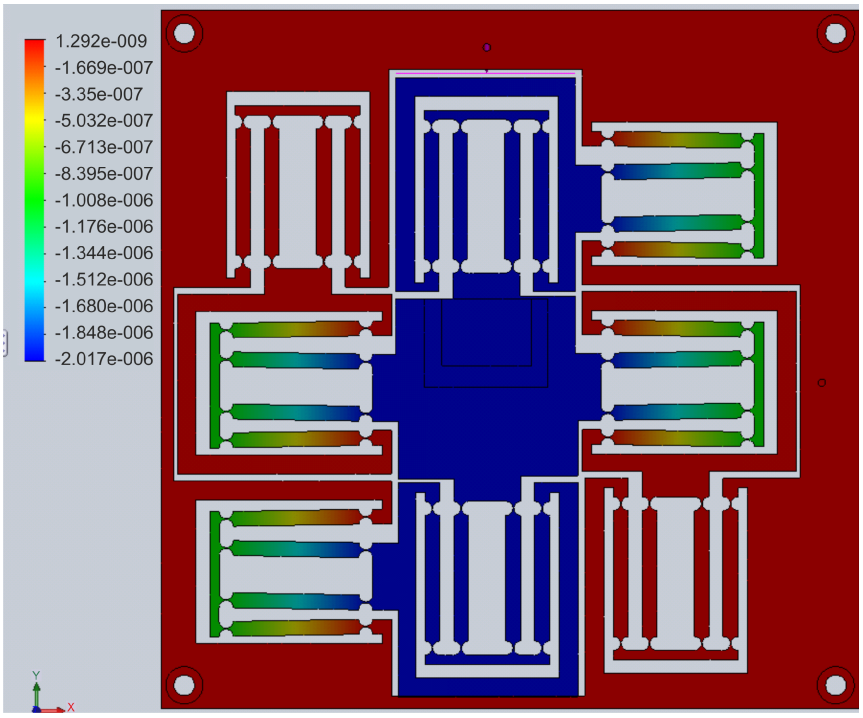

Figure 3.6: FEA simulations with applied load in vertical direction. The vertical stiffness is *4.95 mN/µm.*

3.3.3 Finite element dynamic analysis of FMM

The FEA dynamic analysis in CosmosWorks was used to compute the mode shapes and modal frequencies. The first three mode shapes and modal frequencies were computed and are shown in Figure 3.7. It can be seen that the first two eigen modes are almost equal as expected since the dimensions of the hole hinges are the same and as a result the stiffness in both X and Z direction is kept equal. The Mode 3 is the higher order torsion mode. The first two modes are in the direction of the degree of freedom of the FMM. It is important to mention here that these simulations were performed without adding the mass of the beam and the indenter to the FMM.

In section 3.1 the measured resonance frequency of the FMM was shown and section 0 discussed the measured stiffness of the FMM. The difference in the values simulated and the values measured is first because of the added mass of the beam and the indenter, which will reduce the resonance frequency. Secondly, reducing the mesh size in the critical areas of the FMM can perform more accurate simulations. However, this will increase the simulation time considerably. Thirdly, there may be some manufacturing errors in the FMM and it can be seen from Eq. (3.6) that the stiffness is proportional to the thickness $h^{5/2}$. Therefore, a *10%* decrease in the thickness of the hole hinge will decrease the stiffness of the hinge by approximately *25%*.

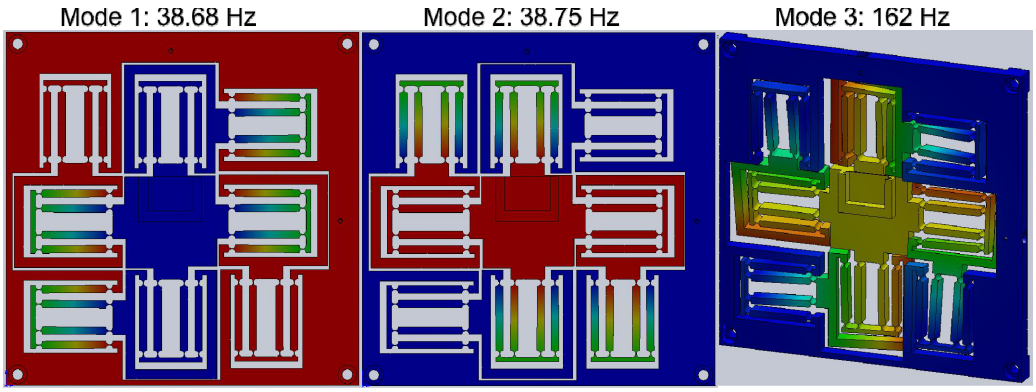

Figure 3.7: First three eigen frequencies of FMM also showing the mode shapes.

3.4 Materials used in the measurements

A list of materials was used to study the adhesion and friction force behaviour in ambient and in HV conditions. A selection of ceramic and glass materials was made based on the requirement from TNO, the industrial partner for this project. To form a single asperity contact between a ball and a flat surface it was required to have either nanometre sized spherical tips or very smooth micro/millimetre sized diameter balls. The nanometre sized spherical tips are easy to get since the AFM tips are commercially available. However, the disadvantage is the limited material choice for AFM tips since they are mostly available in SiO_2 or Si_3N_4. Moreover, the VAFT can measure the adhesion force with an accuracy of *5 μN* and it is known that the adhesion force decreases with the decrease in the diameter of the tip, therefore, a nanometre sized tip cannot be used in this setup. Furthermore, if a nanometre sized tip is used in the contact experiments the contact pressure will be high enough to plastically deform the surfaces. Therefore, the quantitative comparison of the experiments

and contact mechanics theories based on elastically deforming bodies will not be possible.

On the other hand, the second option of using a very smooth micro/millimetre sized ball allows us to compare the theory and experiments as the contact pressure will not lead to plastic deformation of the surfaces. The spherical tips have been divided into two categories, millimetre sized and micrometre sized, which will enable us to study the size effects of the adhesion and friction force. There were also some problems: the first was to find very smooth *1–2 nm* rms rough balls in micrometre size and second was to glue these balls to the sample holder. The millimetre-sized balls were easy to handle and were glued on the indenter and the rms roughness of these balls is within tens of nanometres. To avoid interlocking between the ball and the flat surface due to surface irregularities, it was also required to have a smooth flat surface. The ZrO_2 and Al_2O_3 balls and the flat surfaces (Ceratec Technical Ceramics BV) are relatively rough and the SiO_2, Sapphire, and Si balls (IPS Optics Corp.) are very smooth. Therefore, a smooth flat float glass was used as a counter surface to remove any mechanical interlocking. In Table 3.1 a summary of materials used in this study along with their properties has been presented and the data has been taken from [50-53].

Table 3.1: The material properties of the materials used for adhesion and friction force measurements.

Materials		Radius R (mm)	Elastic modulus E (GPa)	Poisson's ratio ν_p (-)	Shear modulus G (GPa)	Surface energy γ (mJ/m^2)
Single crystalline	SiO_2 (fused silica)	2.5, 0.2, 0.1	73.6	0.17	31.4	44.1±3.1
	Al_2O_3 (sapphire)	2.5, 0.4, 0.2	462.6	0.309	144.3	41.1
Poly crystalline	SiO_2 (float glass)	∞	64	0.2	26	83.4
	Al_2O_3	∞	370	0.22	150	41.1
	Si	2.5	112	0.28	44	44.1±3.1*
	ZrO_2	0.4, 0.2, ∞	205	0.312	81	45.6

* The surface energy values are the same because of the presence of the native oxide on the Si surface

3.5 Adhesion and friction force measurement procedure

To perform adhesion and friction measurements with the VAFT it was required to develop some procedures with which the results can be obtained. LabView was used to develop the complete control interface of the VAFT. One of the most important and difficult problems in contact measurements is to find the point of contact accurately. This is a well-known problem in, for example, nano hardness measurement equipment. If the point of contact is not measured accurately there is always a difference in measured and actual force applied to the sample. There are different techniques that have been used in solving this problem and one of them is force modulation technique, which is implemented by superimposing a small sinusoidal AC force on the DC applied load, see Asif et al. [54]. As discussed above in section 3.1, the system has intrinsic deviations and can be used to find the contact. The deflection signal has variations and as soon as there is a contact the variations are changed both in frequency and amplitude. This can be correlated to the force modulation technique. However, to find the contact accurately the two-step method will be used.

The first step is to find the contact roughly while approaching the sample with a certain velocity. The accuracy of the contact point depends on the approach velocity of the indenter. However, if the approach velocity is too low the measurement time increases. To reduce this time the approach distance has been divided into two parts. First the indenter starts from the home position and approaches the sample with the higher velocity V_1. The velocity of the approach changes to a low velocity V_2 a few microns before the contact.

During this approach the data from the capacitive sensors is logged and the power spectrum of this data will be taken. From the power spectrum the frequency and amplitude information of the variation in the signal can be seen. When the indenter is not in contact a peak at *25–28 Hz* can be seen in the power spectrum, which is the resonance frequency of the hinges. As the indenter makes the contact this peak shifts to a higher frequency of about *80–85 Hz* and the amplitude of the peak also diminishes. This is understandable since the contact stiffness contributes to the total stiffness of the system and the resonance frequency and the amplitude are shifted due to increased stiffness of the system. The position D_1 of the indenter where the resonance frequency is shifted is stored. The power spectrum of the capacitive sensor data measured before and after the contact is shown in Figure 3.8.

In the second step the indenter is retracted to the home position and moved with higher velocity V_1 till the distance D_2 that is $50\ \mu m$ less than the distance (D_1) stored when the contact was detected in the first step. The indenter is moved further downward with low velocity V_2 to a distance D_3 ($50\ \mu m$ + the desired

applied force (F_N) / stiffness of the hinges (k_{tot})). The indenter is then retracted from the sample with the same velocity V_2 till the distance D_3 and finally to the home position with the higher velocity V_1. In this way one single adhesion measurement can be obtained. For multiple adhesion measurements the retraction with higher velocity V_1 is only performed at the end of the measurement. All these steps are implemented in the control software of the VAFT developed in LabView.

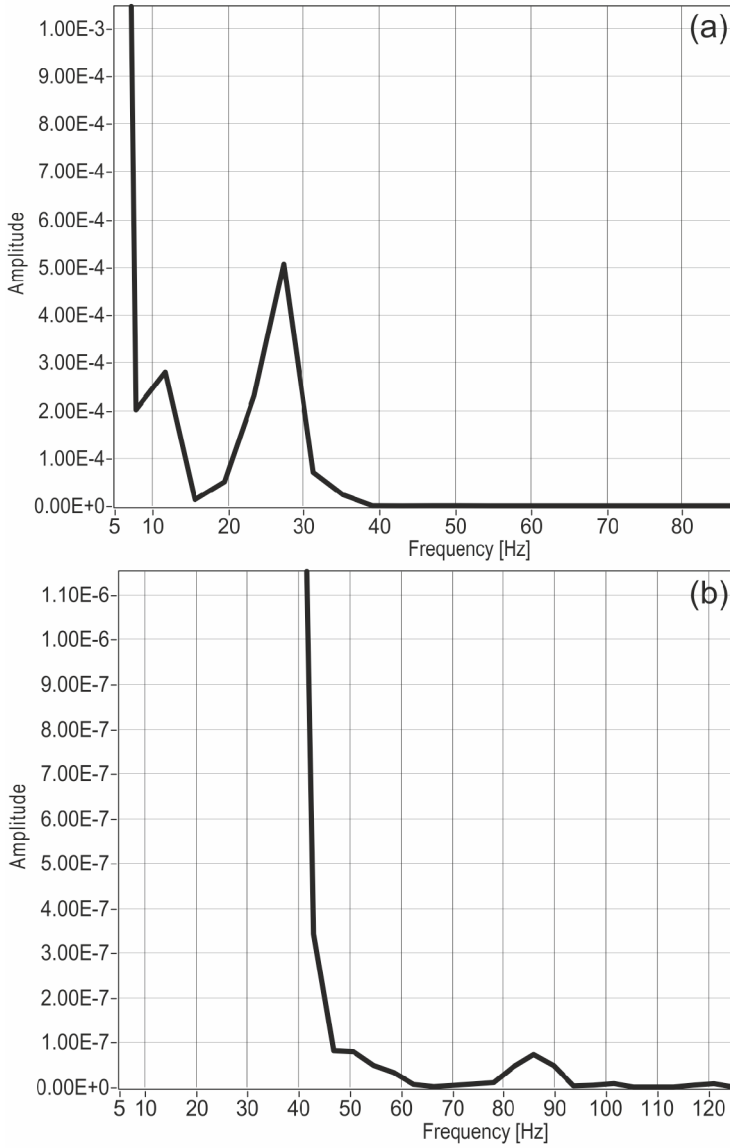

Figure 3.8: Power spectrum of the normal load (capacitive sensor), (a) when the ball is not in contact with the flat surface and (b) when the ball is in contact with the flat surface.

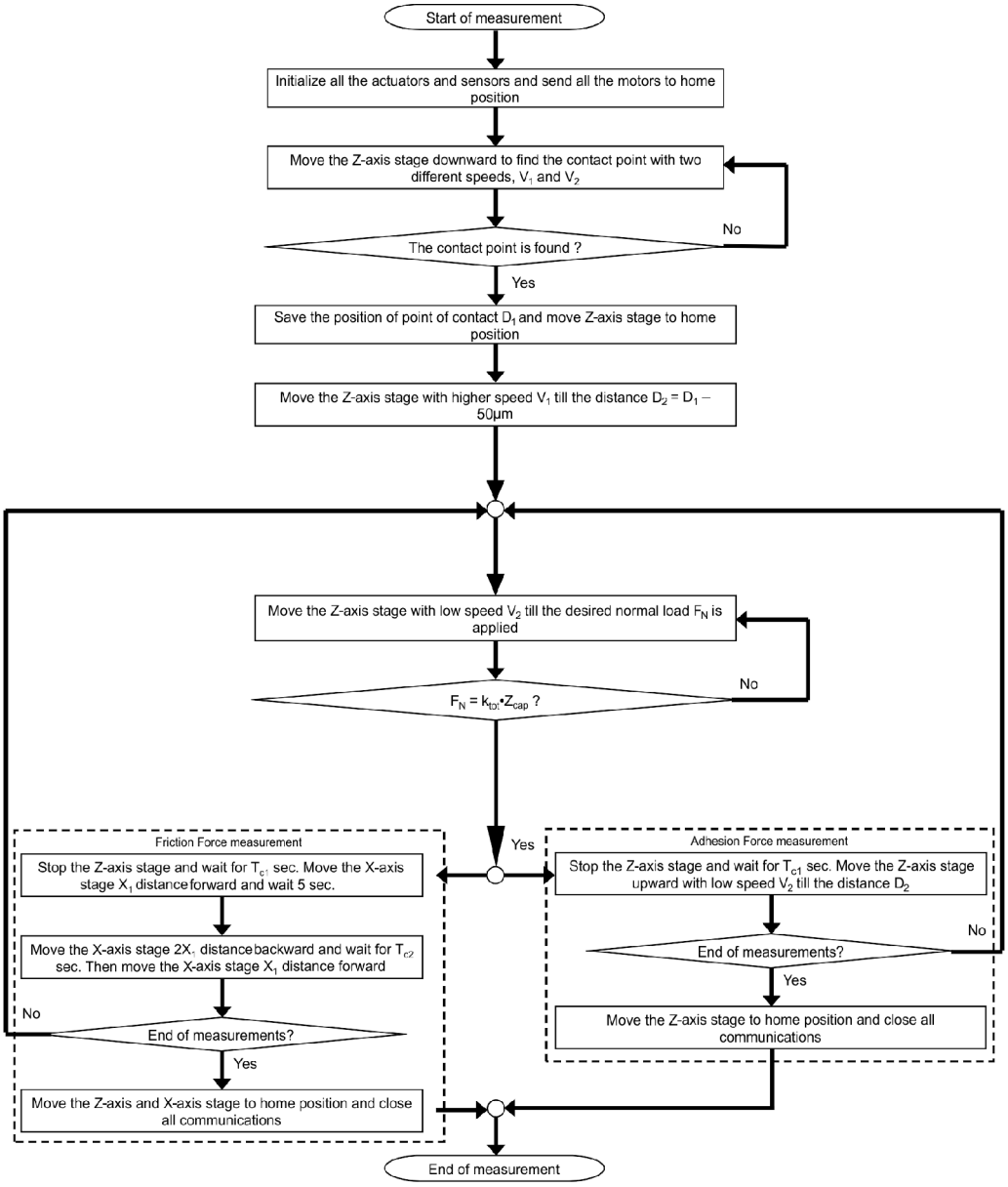

Figure 3.9: Flow chart elaborating the measurement sequence for measuring the adhesion force and the friction force.

Similarly, the friction measurement procedure contains the contact finding technique. After the contact is made the X positioning stage is moved with a certain velocity for a distance of X_1 to the right and back to zero to the left. To make one complete friction loop the X positioning stage has to move the distance X_1 to the right, then the distance X_1 to the left and then again the distance X_1 to the right to reach the zero position. A generic flow chart

explaining the measurement procedure for the adhesion force and the friction force measurements is shown in Figure 3.9. The results of the experiments performed on VAFT will be discussed in detail in Chapter 5, Chapter 6 and Chapter 7.

3.6 Summary

The design of a novel vacuum-based adhesion and friction tester was discussed in detail. It has been shown that the VAFT is capable of measuring the adhesion and the friction force in ambient as well as in HV conditions. The whole setup was designed to reduce the disturbances due to different vibrating sources. The eddy current damping is one of the essential parts of the setup by which the accuracy of the measurements has been increased. The force measuring mechanism was designed to measure the normal and tangential loads independently as much as possible. The stiffness of the FMM has been calculated analytically as well as by using finite element analysis. Furthermore, the stiffness has been calibrated and all the values are in reasonable agreement. The properties of the materials used in the experiments have been presented. The measurement procedures were explained, which are adapted in the control software of the VAFT.

Chapter 4
MODELLING THE ADHESION FORCE FOR SINGLE ASPERITY CONTACT[1]

4.1 Introduction

An introduction with respect to the adhesion force and some main surface force contributions to the adhesion force was described in section 2.2. In section 2.3 the most important contact mechanics models and aspects of the adhesion force were briefly introduced. In this chapter the adhesion force under humid conditions will be discussed in detail. Furthermore, a transition model explaining the transitions of water from a layered structure at low relative humidity (RH) to bulk form at higher RH will also be elaborated. It was discussed earlier in section 2.2.2 that the adhesion force due to capillary interaction between two hydrophilic surfaces is strongly dependent on the partial pressure of water and is often calculated using the Kelvin equation. The validity of the Kelvin equation is questionable at low RH, like in high vacuum (HV) and dry nitrogen environments, where the water is only present as layers several molecules thick at the surfaces.

A transition model for calculating the adhesion force as a function of the partial pressure of water has been developed. The model shows three transitions in the total adhesion force in the whole range of RH (*0–100%*). At very low RH the dry situation is assumed and only solid–solid contact is formed. In this region only the van der Waals force is contributing to the total adhesion force. At the intermediate RH region the van der Waals force due to adsorbed water layers will also contribute to the total adhesion force. In this region the water acts like a solid since the water molecules on the surface are in an ordered form. As the RH increases further the capillary force due to capillary formation of the bulk water will also contribute to the total adhesion force. At higher RH the total adhesion force decreases due to the screening of the van der Waals force.

Furthermore, the effect of the applied normal load on the adhesion force in humid conditions will also be discussed. Similarly, the transient effect on the

[1]Reproduced from: M.A. Yaqoob, M.B. de Rooij and D.J. Schipper, On the transition from bulk to ordered form of water: A theoretical model to calculate adhesion force due to capillary and van der Waals interaction, Submitted to: *Tribology Letters*, 2012.

adhesion force is discussed and an exponential function has been used to represent these transient effects. It was shown that the contact time dependence of the adhesion force is also influencing the normal load dependence of the adhesion force and the two effects are coupled with each other. Moreover, the model has been developed for a single asperity contact neglecting the quantitative effect of the surface roughness on the adhesion force.

4.2 Effects of RH on the adhesion force

An adhesion force is present between two surfaces when they are in contact with each other. The work of adhesion is the work needed to separate these two surfaces and can be used to calculate the magnitude of the total adhesion force present in the system. Capillary forces or meniscus forces are present when the surfaces are in contact or are close to each other under humid conditions. This force strongly depends on RH, roughness of the contacting bodies, radius of the sphere and the hydrophilicity of the contacting bodies. The RH dependence of the capillary force has been reported for several material combinations [1, 3, 4, 6]. In other studies it was seen that due to a high surface roughness the adhesion due to capillary condensation is small compared to other surfaces with low surface roughness [9, 21, 26]. On the other hand, the validity of the Kelvin's equation under these conditions is questionable and the reasons were discussed in section 2.2.2. Therefore, a model for calculating the adhesion force at low RH is required, which can also incorporate the effect of adsorbed layers on the surface.

4.2.1 Adsorption

The accumulation of a certain material (gas or liquid) on the surface of another material (solid) is termed as the *adsorption* phenomenon [16]. The material attached to a surface in the adsorbed state is called *adsorbate* and the same material when not attached to the surface is *adsorpt* or *adsorptive*. The surface onto which the adsorption takes place is called the *adsorbent* as shown in Figure 4.1. The Langmuir, BET and Polanyi theories are some of the important theories to describe the adsorption phenomena [16]. The adsorption behaviour of solid-gas interface only be discussed and will consider water vapour present in the air as gas. The water molecules adsorb and desorb on the surfaces and the thickness of the resulting adsorbed water layer can be calculated as a function of RH. Brunauer, Emmett and Teller extended the Langmuir monolayer adsorption model to a more practical multilayer adsorption model. The model is called the BET adsorption model or BET adsorption isotherm [16]. The BET model can be used to estimate the film thickness on the surface as a function of

the RH. There are some assumptions used in this model, which limits its applicability in the whole range of RH, however, for the first estimate of the adsorbed film thickness this model is suitable. On the other hand, experiments have been performed to measure the adsorption layers on surfaces using Attenuated Total Reflection (ATR) infrared spectroscopy [55]. Verdaguer et al. [56] studied the growth and structure of water on SiO_2 by several techniques, like surface potential measurements using an atomic force microscope (AFM) and ambient pressure X–ray photoemission and near edge X–ray absorption fine structure spectroscopies (XPS and NEXAFS). The measurement results also followed the BET adsorption isotherm between *5-40%* RH, which indicates the applicability of the model in this range.

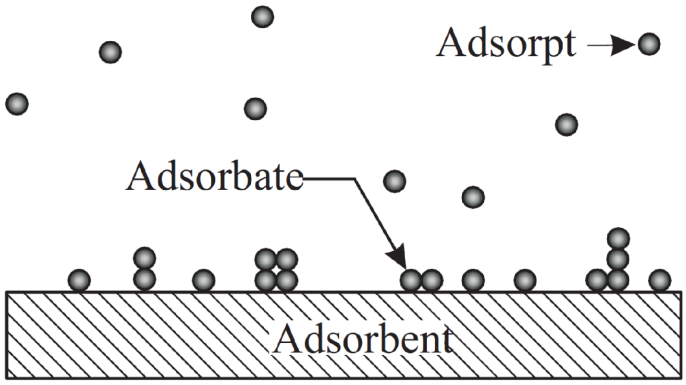

Figure 4.1: Illustration of the definitions of adsorpt, adsorbate, and adsorbent [16].

As the amount of water content in the environment increases, the amount of adsorbed water molecules on the surfaces will also increase. The thickness of this adsorbed water layer can be calculated using BET adsorption isotherm [16]. According to the model, the film thickness T_f as a function of RH is given as [16]:

$$T_f = \frac{C_{BET} \cdot n_{mon} \cdot m_A \cdot \sigma_A}{\left(1 - \frac{p}{p_s}\right) \cdot \left[1 + \left\{\frac{p}{p_s} \cdot \left(C_{BET} - 1\right)\right\}\right]} \cdot \frac{p}{p_s} \qquad \because C_{BET} = e^{(Q_1 - Q_i)/R_g T} \qquad (4.1)$$

Where, C_{BET} is called the BET constant dependent on the Q_1 and Q_i which are the heat of adsorption of the first layer and heat of condensation of the adsorbate (here water) respectively. R_g and T are the gas constant and Temperature, respectively and p/p_s is the relative humidity. The n_{mon} is the number of adsorbed molecules in one full monolayer per unit area, σ_A is the cross sectional area and m_A is the diameter of the adsorbate molecule (for water, σ_A is *0.77 nm*^{2} and m_A is approximately *2.75 Å*) [57, 58]. The typical values of

C_{BET} and n_{mon} for different materials have been measured and it was shown that the film thickness is strongly dependent on the hydrophilicity of the adsorbent [59]. The C_{BET} values used further for non–porous α-alumina and silica are *28* and *11* and the corresponding n_{mon} values are *6.5* and *3.6* molecules per nm^2 respectively [16, 59].

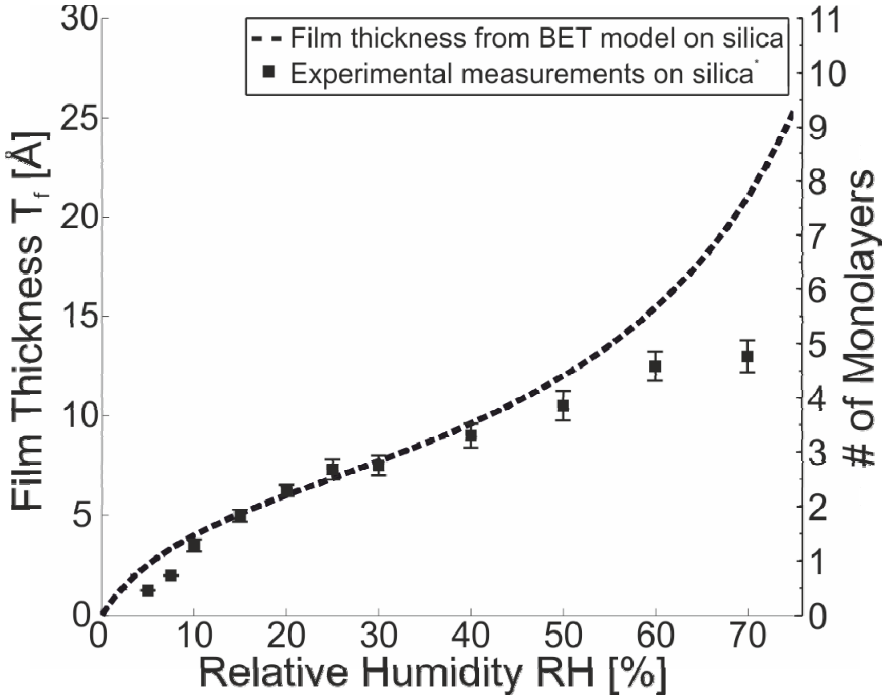

Figure 4.2: Water film thickness as a function of RH on silica surface calculated using BET adsorption isotherm. The theoretical values have been compared with the measurement results from the literature [55]*.

The BET isotherm for silica is shown in Figure 4.2 and is compared with the values of measured film thickness from the literature [55]. It can be seen that the measured values fit well until *50%* RH which is strong evidence to use the BET isotherm for calculating film thickness until *50%* RH for silica. The first monolayer forms at about 10% RH, therefore, we can consider solid–solid contact before *10%* RH. After *10%* RH the monolayer starts to grow in multilayers and at about *30%* RH 3 monolayers are formed. The water will be considered as bulk only if the number of monolayers is greater than 3 [55, 56]. So, water will be in an ordered form from 10% to *30%* RH. The film thickness keeps on growing slowly and there is a transition from ordered to bulk form of water between *30%* and *60%* RH. After *60%* RH the meniscus will be formed around the sphere–flat contact and the water layers can be considered as bulk. However, the increase in the amount of water in the contact will decrease the

van der Waals force due to more adsorbed layers of water. This is called the screening of the van der Waals force [7].

4.2.2 Transition model for the adhesion force

The capillary force for the sphere–plane geometry, as shown in Figure 4.3 can be calculated using the following equation (Eq. (2.18) rewritten).

$$F_{cap} = -2\pi R\gamma_L\left(\cos\theta_1 + \cos\theta_2\right) \tag{4.2}$$

The capillary force is directly influenced by the contact angles of the surfaces. Similarly, from Eq. (4.2) it can also be seen that there is no RH dependence on the capillary force. However, there is strong experimental evidence of RH dependence of the capillary force [1, 3, 4, 6]. There are several reasons which restrict the applicability of Eq. (4.2) like the filling angle $\varphi \approx 0$ if the $R \gg r_2 \gg r_1$ [6, 39]. First, the filling angle is dependent on the RH where the meniscus radius r_2 increases with an increase in RH. As the amount of water in the system increases the meniscus will grow and will increase the meniscus radius r_2. Secondly, for a small tip radius R e.g. an AFM tip the $R \gg r_2 \gg r_1$ approximation fails [6]. Thirdly, there is no contribution from the surface tension force in the total capillary force shown in Eq. (4.2), which is again an important contribution for small radii tips.

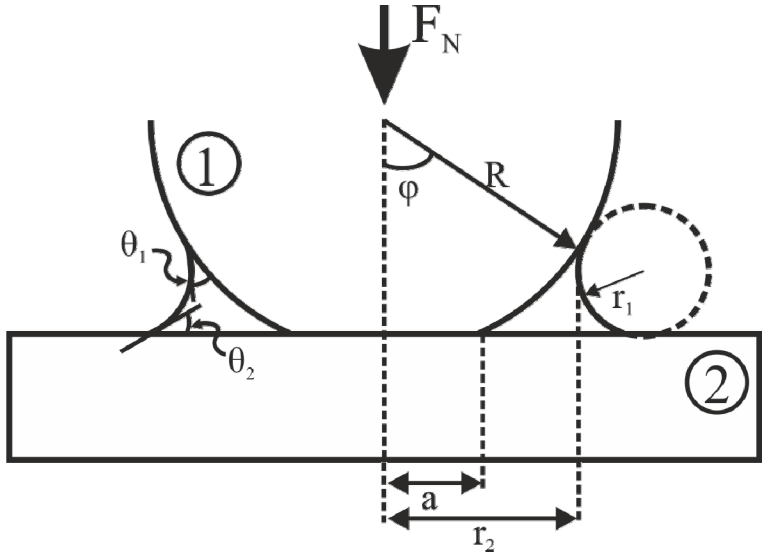

Figure 4.3: A sphere in contact with a flat surface under a certain applied normal load F_N in a humid environment. The solid–solid contact radius a and the meniscus radius r_2 are also shown.

The water is considered in a structured form or an ordered form until 3 monolayers of water molecules. Only at higher thickness values there is a transition from ordered to bulk behaviour and consequently meniscus behaviour [55]. Therefore, the Kelvin equation cannot be used to calculate the adhesion force for low RH. The force acting on the sphere due to meniscus formation when the meniscus is in equilibrium was shown in section 2.2.2 and is rewritten as:

$$F_c = F_s + F_p \tag{4.3}$$

$$F_s = -2\pi\gamma_L r_2 \sin(\theta_1 + \varphi) = -2\pi\gamma_L R \sin\varphi \sin(\theta_1 + \varphi) \tag{4.4}$$

$$F_p = -\Delta p \pi\left(r_2{}^2 - a^2\right) = -\left[-\frac{R_g T}{V_m}\log\left(\frac{p}{p_s}\right)\right]\pi\left(R^2\sin^2\varphi - a^2\right) \tag{4.5}$$

In Eq. (4.5) the capillary pressure Δp is given by using the Young–Laplace and Kelvin equations. R_g is the universal gas constant, T is the absolute temperature, V_m is the molar volume, p and p_s are the equilibrium and saturation vapour pressures of the liquid, respectively and a is the contact radius for solid–solid contact which can be calculated by e.g. Hertz theory [28].
It can be seen that the total capillary force F_c can be calculated if the filling angle φ is known. This filling angle can be calculated implicitly using the Young–Laplace and Kelvin equations along with the geometrical analysis of the contact situation shown in Figure 4.3 and is given as [6]:

$$\frac{\Delta p}{\gamma_L} = \left(\frac{1}{r_1} + \frac{1}{r_2}\right) = -\frac{R_g T}{V_m \gamma_L}\log\left(\frac{p}{p_s}\right) \tag{4.6}$$

$$-\frac{R_g T}{V_m \gamma_L}\log\left(\frac{p}{p_s}\right) = \frac{\cos(\theta_1 + \varphi) + \cos\theta_2}{D + R(1 - \cos\varphi)} + \frac{1}{R\sin\varphi} \tag{4.7}$$

Here D is the distance between the sphere and the flat (not shown in Figure 4.3) which is assumed to be *0.2 nm* when the sphere and flat are in contact [7]. It can be seen that by simplifying Eq. (4.5) using the assumptions explained above, the basic equation (Eq. (4.2)) can be obtained.
In the solid–solid contact, without the meniscus, the van der Waals force will only contribute to the total adhesion force. This solid–solid contact situation can also be termed as the dry contact situation when there will be very little water present (very low RH) in the environment like in High Vacuum (HV) or Ultra

High Vacuum (UHV). The van der Waals force for sphere–flat geometry can then be calculated by [7]:

$$F_{S-vdw} = -\frac{A_{132}R}{6D^2} \tag{4.8}$$

Where, A_{132} is the Hamaker constant between sphere 1 and flat 2 in medium 3 (here vacuum). As mentioned earlier the separation distance D is assumed to be *0.2 nm* when the surfaces are in contact, therefore the van der Waals force due to solid–solid contact is a constant for a certain set of materials of constant geometry.
The contact situations representing three different regions of RH are schematically shown in Figure 4.4. The van der Waals force between 10% and 30% RH considering the adsorbed layer system between a sphere and a flat surface $F_{W\text{-}vdw}$ as shown in Figure 4.4(b) is given by [7]:

$$F_{W-vdw} = -\frac{R}{6}\left[\frac{A_{waw}}{D^2} - \frac{\sqrt{A_{1w1}A_{awa}}}{\left(D+T_{f1}\right)^2} - \frac{\sqrt{A_{2w2}A_{awa}}}{\left(D+T_{f2}\right)^2} + \frac{\sqrt{A_{2w2}A_{1w1}}}{\left(D+T_{f1}+T_{f2}\right)^2}\right] \tag{4.9}$$

Where, T_{f1} is the water film thickness on the sphere 1, T_{f2} is the water film thickness on flat 2, *w* represents water and *a* represents air or vacuum.
It is important to mention here that the Hamaker constant A_{waw} or A_{awa} has been calculated using pairwise additivity rather than using Lifshitz theory. This is because the water molecules in *10%* to *30%* RH cannot be considered as bulk and the Lifshitz theory considers materials to be in bulk form and uses bulk properties. However, the transition region for other materials can be different as explained above depending on the trend of film thickness as a function of RH.

4.2.3 Results and discussion

The above theory can be used to calculate the total adhesion force for a wide range of RH. Considering the above analysis, Eq. (2.23) can be rewritten as:

$$F_a = \begin{cases} F_{S-vdw} & T_f \le 1\,\text{monolayer} \\ F_{S-vdw} + F_{W-vdw} & 1\,\text{monolayer} < T_f \le 3\,\text{monolayers} \\ F_{S-vdw} + F_{W-vdw} + F_c & T_f \ge 3\,\text{monolayers} \end{cases} \tag{4.10}$$

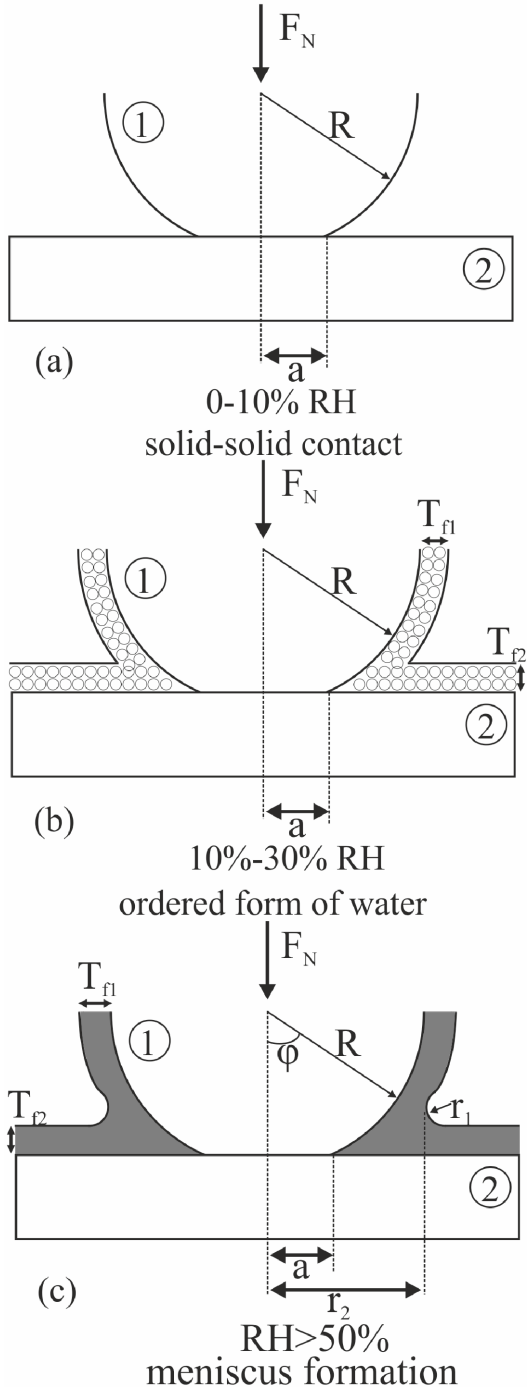

Figure 4.4. Schematic representation of different contact situations for different regions of RH. The solid–solid contact depicts the completely dry situation, the ordered form of water shows the monolayer formation due to adsorption and meniscus formation shows a bulk water forming meniscus.

Using Figure 4.2 we can correlate the number of monolayers with the RH. It can be seen that there are two transitions in the adhesion force as shown in Eq. (4.10). The first transition is from solid–solid to solid–solid + adsorbed layered system and the second one is from solid–solid + adsorbed layered to solid–solid + adsorbed layered + meniscus. An S–shaped function has been used in both the transitions since it is physically realistic. It is important to mention here that the emphasis is on the adhesion force levels (e.g. F_{S-vdw} and F_{W-vdw} etc.) rather than the exact shape of the transitions. From Figure 4.2 it can be seen that the first monolayer on silica is formed at approx. *10%* RH and three monolayers are formed at about *30%* RH. For the first transition, for example, this S–shaped curve in terms of RH could be given as:

$$F_{atran1} = \begin{cases} F_{S-vdw} & x \le RH_0 \\ F_{S-vdw} + \left[\left(F_{W-vdw} - F_{S-vdw} \right) \cdot \left(2 \cdot \left(\dfrac{x - RH_0}{RH_1 - RH_0} \right)^2 \right) \right] & RH_0 \le x \le \dfrac{RH_0 + RH_1}{2} \\ F_{W-vdw} - \left[\left(F_{W-vdw} - F_{S-vdw} \right) \cdot \left(2 \cdot \left(\dfrac{RH_1 - x}{RH_1 - RH_0} \right)^2 \right) \right] & \dfrac{RH_0 + RH_1}{2} \le x \le RH_1 \\ F_{W-vdw} & x \ge RH_1 \end{cases} \tag{4.11}$$

Where, F_{atran1} is the adhesion force in the transition region RH_0–RH_1, RH_0 is the start of the transition from the dry situation to the first monolayer situation, RH_1 is the relative humidity where one complete monolayer is formed and x is the humidity level between RH_0 and RH_1. Similar expressions have been used for the RH_2–RH_3 and RH_4–RH_5 transition regions shown in Figure 4.5.

The results show that the adhesion force calculated using the Young–Laplace and Kelvin equations at low (*5–30%*) RH is underestimated as can be seen from Figure 4.5. The calculated total adhesion force shows changes when the RH is changed from *0–100%*. In dry conditions, at RH below *10%*, the total adhesion force is contributed by the van der Waals interaction due to solid–solid contact. The total adhesion force then increases at relatively high RH and remains constant. The total adhesion force further increases slowly with the increase in RH and then decreases at very high RH. This change in adhesion force occurs from solid–solid interaction to ordered form of water at low RH and from ordered form to bulk form of water at high RH along with the screening effect of van der Waals interaction.

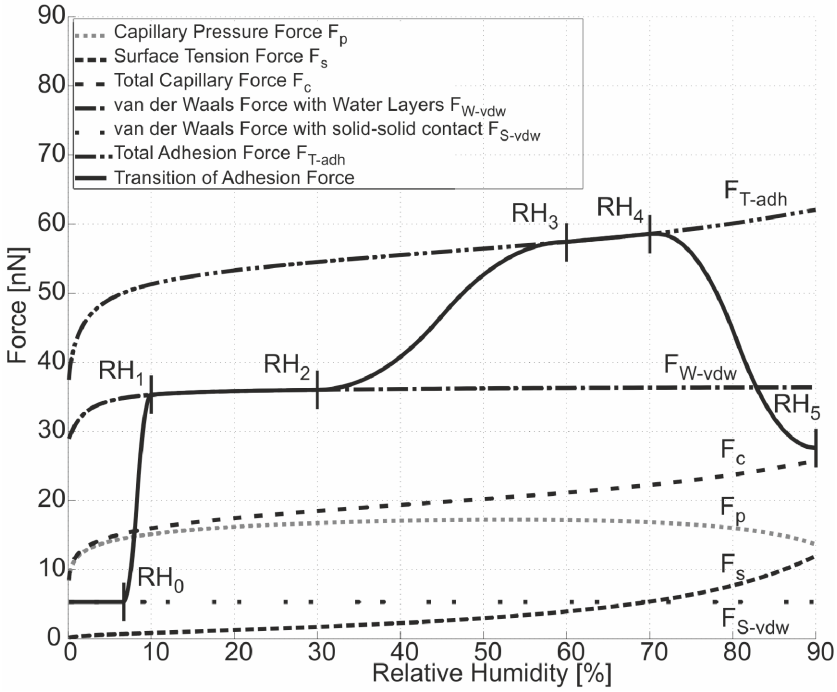

Figure 4.5. Simulation results of the trends of different surface forces as a function of RH for a *20 nm* radius Si ball and a glass flat. The solid–solid contact $F_{S\text{-}vdw}$ depicts a completely dry situation, the ordered form of water $F_{W\text{-}vdw}$ shows the monolayer formation due to adsorption and meniscus formation F_c shows bulk water forming meniscus. The transition line shows the transition in adhesion force at different RH.

Two different sizes of Si ball were used to calculate the adhesion behaviour of SiO_2-glass interface. It is important to mention here that the Si ball has a native oxide on the surface, hence "SiO_2-glass" terminology has been used in this chapter. The adhesion force has been calculated for 20 nm and *2.5 mm* radius balls against a flat surface. The results from the model for a Si ball of 20 nm with a native oxide and a glass surface are shown in Figure 4.5. This size of the contact geometry is used in comparison with the results from the literature.

AFM pull-off measurements for different RH between SiO_2 and 100 nm radius Si_3N_4 tip had been reported by Xiao and Qian [6]. Similar results were shown by Jones et al. [4] between *20 nm* radius SiO_2 ball and using glass and SiO_2 as counter surfaces and by He et al. [24] between Si and *20 nm* radius Si_3N_4 tips. Furthermore, the results from the literature mentioned above do not show pull–off measurements at RH < *10%*. The results from the literature have been summarized in Figure 4.6 and they show good agreement with the proposed model. The experimental data from the different literature sources is not quantitatively in mutual agreement as shown in Figure 4.6. There are many possible reasons for these differences since the measurements were performed with different material combinations and experimental setups. However, from

Figure 4.6 it is clear that the model predicts the same order of magnitude of all these measurements.

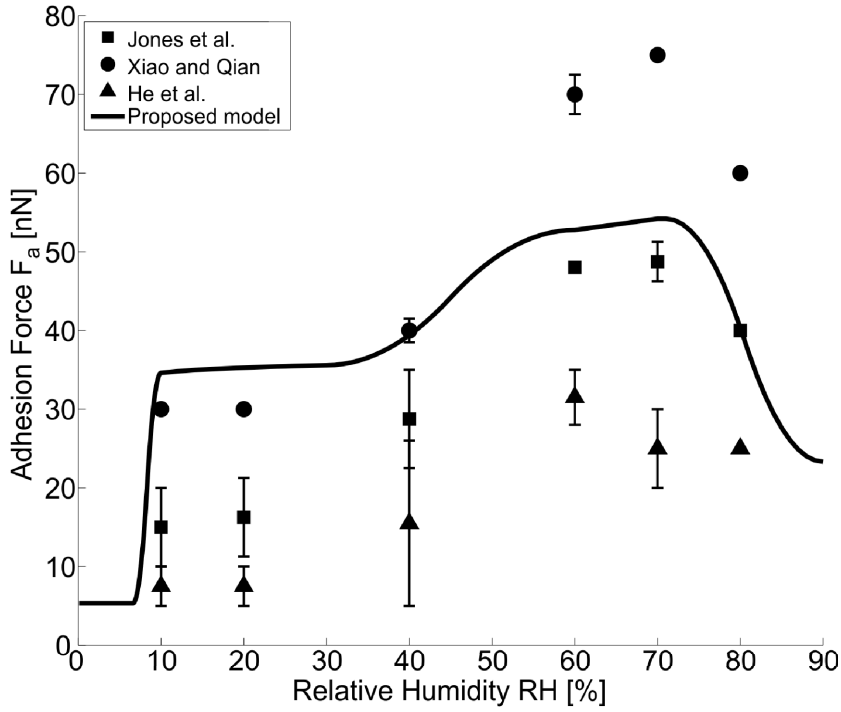

Figure 4.6. Comparison of the adhesion force measured by Jones et al. [4], Xiao and Qian [6], He et al.[24] and calculated by the proposed model.

Three distinctive regions are shown in Figure 4.5 and Figure 4.6 which depend on the RH of water. At very low RH < *5%* there is no water, as can be seen from Figure 4.2, then the adhesive force is contributed by the van der Waals force between the two solid surfaces and therefore called solid–solid contact. In the region from *5%* < RH < *10%* the water molecules start to adsorb more rapidly and at *10%* RH the first monolayer is formed. In this region the transition is shown from solid–solid to an ordered layered system. From *10%* to *30%* RH there will be an ordering effect where the adhesive force is contributed by the van der Waals forces of adsorbed water layers on the surfaces. When RH > *30%* a slow transition will start from ordered to bulk and at *60%* the transition completes as the fourth monolayer is formed. At this stage the meniscus will be formed and the total adhesive force is contributed by the superposition of van der Waals force due to solid–solid contact, van der Waals force due to adsorbed water layers and capillary force which can be calculated using equation (4.3). Furthermore, it can also be seen that at nano scale the surface tension force F_s cannot be neglected. As the RH increases the screening of the van der Waals force can be seen above *70%*.

It is important to mention here that these simulations were performed by considering the contact between two smooth surfaces. Furthermore, it was assumed that there are no transient effects, i.e. the contact time was considered constant for all the measurements. It can be seen that the total capillary force F_c calculated with equation (4.3) using the Kelvin equation underestimates the total adhesion force and does not predict the transition regions in the total adhesion force. The total adhesion force $F_{T\text{-}adh}$ is the superposition of all the adhesive forces present in the system. The transition curve (solid line) shows the transition between the three distinct regimes as shown in Figure 4.4.
Similar simulations were carried out for a Si ball of 5 mm diameter in contact with a glass flat surface. The calculated adhesion forces with the model are shown in Figure 4.7. It can be seen that the contribution of the surface tension force F_s to the total capillary force F_c can be neglected for this radius. Therefore, the total capillary force is equal to the capillary pressure force F_p. These simulations were carried out to compare the results to the adhesion measurements performed with VAFT discussed in detail in Chapter 3. The measurement results fit well with the model for a *5 mm* diameter ball by considering the influence of surface roughness and will be discussed in detail in Chapter 5.

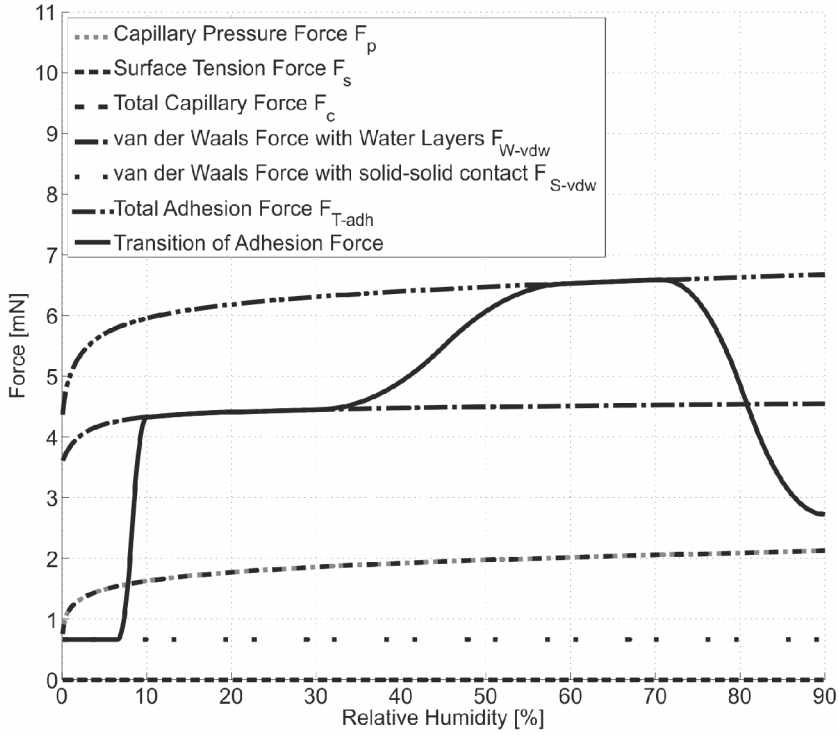

Figure 4.7: Simulation results of the trends of different surface forces as a function of RH for a 5 mm diameter Si ball against a glass flat.

4.3 Normal load and contact time effects on adhesion force

It was mentioned in section 4.2 that the effect of RH was studied by considering smooth contact under constant applied normal load and contact time. However, the normal load and contact time can also influence the adhesion force and, therefore, will be discussed. Furthermore, the interdependency of normal load and contact time is important to consider and will be addressed.

In section 2.3 different contact models were discussed that could be used to calculate the contact area of the interface. Hertz theory explains the deformation of the materials in contact without considering the adhesion force. JKR, DMT and M-D models explain the influence of adhesion force on the contact area. However, according to these models the adhesion force influences the deformation of the contact and the contact area. The influence of the presence of the capillary force is, however, not clearly incorporated in these models as they typically assume van der Waals adhesive behaviour. Efforts have been made to incorporate the meniscus force in the contact models, which was also discussed in section 2.3.3. In this model the influence of RH on the adhesion force has been elaborated but the effect of normal load on the adhesion force was not explained. Moreover, Eq. (2.32) and Eq. (2.34) shows that the adhesion force is independent of the normal load. It has previously been explained that the capillary force, if present, dominates the adhesion force in a contact. Furthermore, it has been shown that there is a dependency of the normal load on the adhesion force in humid environment [60, 61]. However, Ferreira et al. [60] suggested that the change in the adhesion force by changing the normal load is due to the plastic deformation of an AFM tip.

For a sphere-flat contact as shown in Figure 4.3 under humid conditions the capillary pressure force is given by Eq. (4.5). It can be seen that capillary pressure force is a function of the square of the contact radius a and the radius of the meniscus r_2. It was shown before in Chapter 2 from Hertz theory that the contact radius is a function of applied normal load and the radius increases with the power *1/3* as the normal load increases. However, the Hertz theory does not incorporate adhesion effects, which are important to consider at low applied normal loads as explained by Johnson [34]. The normal load dependency of the contact area as explained by Hertz remains more or less the same in JKR and DMT theories. Therefore, to estimate the normal load dependency of the contact area even when adhesion plays an important role the, Hertz theory can be used. This means that a *2/3* power dependency of normal load on the adhesion force is expected.

The second important aspect is related to the time needed to form an equilibrium meniscus at pull-off. During the pull-off experiments, at a certain

pull-off force the contact radius a goes to zero and the surfaces remain in contact due to the presence of liquid meniscus. Further retraction of the surfaces will finally break the contact. It is known that the capillary condensation and evaporation is a thermally activated process [62], therefore, it is dependent on the contact time and the loading/unloading rate by which the surface is brought in contact. If the surfaces are kept in contact for longer periods of time the adhesion behaviour changes. Similarly, if the surfaces are moved apart very slowly there will be enough time for the water meniscus to diffuse between the gap and the meniscus will be elongated with the surfaces. After a certain distance the meniscus will no longer be stable and the surfaces will break away from each other.

The time required by the water to diffuse between the surface can be calculated by the following expression for the diffusion distance [63]:

$$\Lambda = 2\sqrt{D_s t} \tag{4.12}$$

Where, Λ is the distance on which the diffusion has to take place, t is the time required to complete the diffusion and D_s is the surface diffusion coefficient. In [64] the diffusion coefficient of water on mica has been reported to be $3.85\times10^{-16}\ m^2/sec$. The surface diffusion coefficients have been reported to be in the range from 10^{-16} to $10^{-11}\ m^2/sec$. If we apply a load of $10\ mN$ on a Si-glass interface the contact radius according to Hertz is calculated to be $9\ \mu m$ for a ball of $5\ mm$ diameter. If this is the distance on which the diffusion has to take place by the water when the two surfaces are pulled apart, then the time required to complete the diffusion using Eq. (4.12) can be calculated. If we assume the surface diffusion coefficient of $10^{-13}\ m^2/sec$, the time required to diffuse the water is approximately $250\ sec$, which corresponds to typical stabilization times for other studies, see Chapter 2. If the contact is broken faster than the diffusion time the radius of the meniscus r_2 will remain more or less unchanged and therefore, a normal load dependent adhesion force behaviour can be expected. However, if the contact is broken slower than the diffusion time then there will be enough time for water to diffuse resulting in a reduction in the size of a meniscus radius and the adhesion force will be independent of normal load. It is important to mention that this behaviour is only plausible when the interface under study is operated in humid conditions. If the interface is operated in HV conditions the normal load dependency of the adhesion force cannot be expected as there is no meniscus formation and diffusive effects do not play a significant role.

Similarly, the transient effects on the adhesion force in a humid environment have also been reported [65-67]. The time for which the two surfaces remain in contact influences the adhesion force. If the contact is pulled off too quickly

there will not be enough time to form a meniscus around the contact. However, on the other hand if the contact time is large enough the equilibrium in the capillary condensation will be reached. It has also been reported that the time required by the adhesion force to reach the steady state depends on the size of the contact [10]. A sphere-flat contact with the smaller sphere radius will reach the equilibrium much faster than with the larger sphere radius. As it has been discussed before, capillary condensation is also a thermally activated first order gas-liquid phase transition [62, 68]. Therefore, the contact time effects on the adhesion force have been modelled using a simple exponential function given as:

$$F_a(T_c) = F_{a(eq)} - F_{a0}e^{(-k_r T_c)} \tag{4.13}$$

Where, $F_a(T_c)$ is the contact time dependent adhesion force, $F_{a(eq)}$ is the adhesion force at the equilibrium, i.e. when a meniscus is in steady state, F_{a0} is the initial adhesion force, k_r is the rate constant and T_c is the contact time. The schematic representation of Eq. (4.13) is shown in Figure 4.8. This expression will be used in experiments explained in Chapter 5 to validate the contact time dependency of the adhesion force.

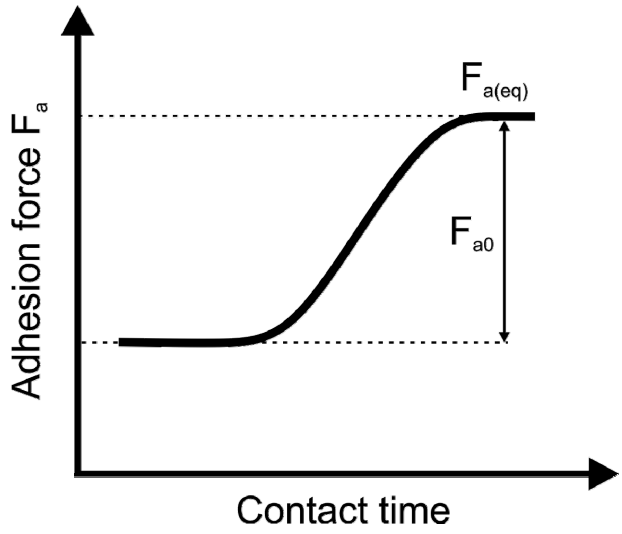

Figure 4.8: Schematic representation of contact time dependence of adhesion force using an exponential function shown in Eq. (4.13).

4.4 Summary

A transition model for calculating the adhesion force as a function of RH was developed using the BET adsorption isotherm. The results of the calculated adhesion force show that the Kelvin equation cannot be used below a certain RH. The results also show that the Kelvin equation cannot predict the transition behaviour of the adhesion force with changing RH. The model shows good agreement with the measurement results for a selected pair of materials from the literature for nano scale contacts. The trend of the effect of humidity on the adhesion force is well predicted.
The effect of normal load on the adhesion force has been discussed. It was shown that if the contact is broken faster than a certain threshold a normal load dependent adhesion force is expected in humid conditions. However, if the contact is broken slowly this effect is not expected to happen. A load dependent capillary force is therefore expected for relatively small contact time. The adhesion force is expected to change with the normal load to the power of *2/3*. Furthermore, the normal load dependency of the adhesion force is only expected in humid conditions. The effect is not expected when the interface is operated in low humidity or in HV environment because the van der Waals forces are not related to surface diffusion effects. The effect of contact time/ rest time has also been discussed and it was shown that this effect can be modelled by an exponential function. The influence of contact time on the adhesion force is also not expected to happen if the interface is operated in HV conditions.

Chapter 5
ADHESION FORCE MEASUREMENTS[1]

5.1 Introduction

In Chapter 4 a newly developed RH dependent adhesion force model was discussed. It is therefore required to validate this model by means of experiments. Similarly, the independent and interdependent effects of normal load, contact time, size and roughness on the adhesion force were studied experimentally to see how they agree with the theory.
Adhesion experiments were performed on the VAFT (explained in Chapter 3) using different materials having different surface and material properties. These experiments were performed both in ambient conditions as well as in high vacuum (HV) conditions. The effects of several parameters on the adhesion force have been studied by performing dedicated experiments. Adhesion measurements have been performed, by changing the RH in the chamber, to see the effect on the capillary force. In HV conditions the amount of water in the chamber is limited and therefore the capillary force can be controlled. Similarly, the effect of the applied normal load on the adhesion force has also been studied for different materials in ambient and HV conditions.
In section 5.2 an introduction to the adhesion measurements performed on VAFT and UNAT will be given. Effects of RH on the adhesion force measurements are discussed in section 5.3 and the model explained in Chapter 4 will be compared. In section 5.4 the normal load effects on the adhesion force will be presented. Contact time effects will be explained in section 5.5 and the size and surface roughness effects will be discussed in section 5.6.

5.2 Adhesion force measurements

Adhesion force measurements were performed between different material combinations as listed in Table 3.1 using the test setup explained in Chapter 3. All the measurements were performed using a ball and flat configuration. The materials used are hydrophilic as the contact angles shown in Appendix C are

[1]Reproduced from: M.A. Yaqoob, M.B. de Rooij and D.J. Schipper, On the transition from bulk to ordered form of water: A theoretical model to calculate adhesion force due to capillary and van der Waals interaction, Submitted to: *Tribology Letters*, 2012.

below *90°*. The two surfaces were approached with a speed of *100 nm/sec* and, taking into account the stiffness of the FMM, the loading rate is approximately *385 μN/sec*. Different kinds of measurements were performed to study the effect of RH, normal load, contact time, size and roughness on the adhesion force. For example, to measure the effect of RH all the other parameters were kept constant. When the two surfaces become very close to each other they are attracted to each other because of the presence of the adhesion force and suddenly makes a contact. This sudden jump-in of the contact is termed as *snap-in*. Similarly, when the surfaces are moved apart, at a certain distance they suddenly lose contact contrary to the snap-in phenomenon, and this is called *pull-off*. A typical force-displacement curve in the normal direction can be acquired after each snap-in and pull-off measurement. Typically, the magnitude of the snap-in force is less than the magnitude of the pull-off force. In this study, the magnitude of the pull-off force is used to define the adhesion force present between the two surfaces under defined conditions.

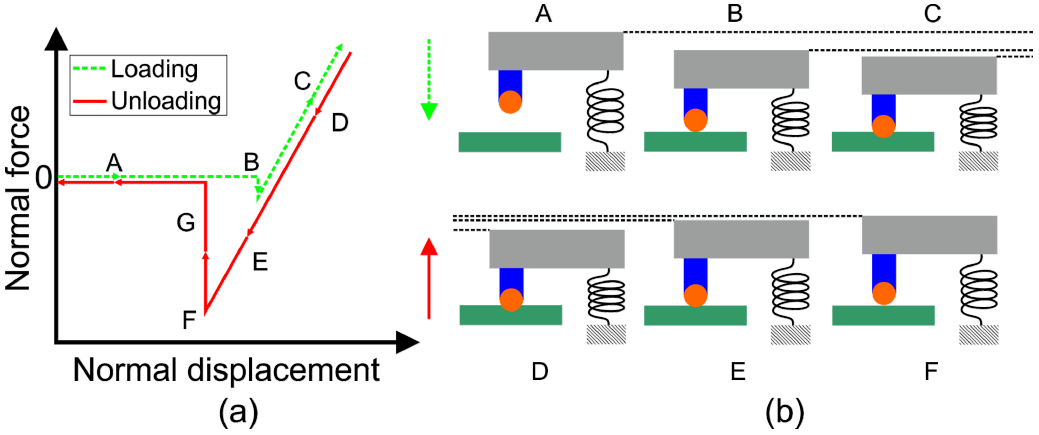

Figure 5.1: (a) Schematic representation of a force-displacement curve in normal direction. (b) Contact situation at different points on the force-displacement curve.

A schematic representation of a measurement of a force-displacement curve in the normal direction is shown in Figure 5.1. The loading and unloading curves have been shown along with the snap-in and pull-off points. The schematic representation of the ball flat contact configuration is also shown in Figure 5.1(b) at some selected points on the force-displacement curve. First, the ball and a flat surface are moved close to each other as shown in point A. Here, the separation distance is large enough and there are no surface forces acting between the surfaces. As soon as the distance is reduced to a certain threshold where the surface forces start to influence the surfaces, a snap-in occurs as shown at point B. The desired normal load is then applied on the contacting interface as shown at point C. At this point the rest time can be added where the surfaces remain in contact under the desired normal load for a certain amount of

time. The surfaces are then retracted or unloaded as shown at point D and it can be seen that even after the applied normal load is completely removed from the interface, the surface remains in contact and a negative force is required to break the contact as shown at point E and, finally, the pull-off occurs at point F. The surfaces are separated and the system goes to its equilibrium position after point G.

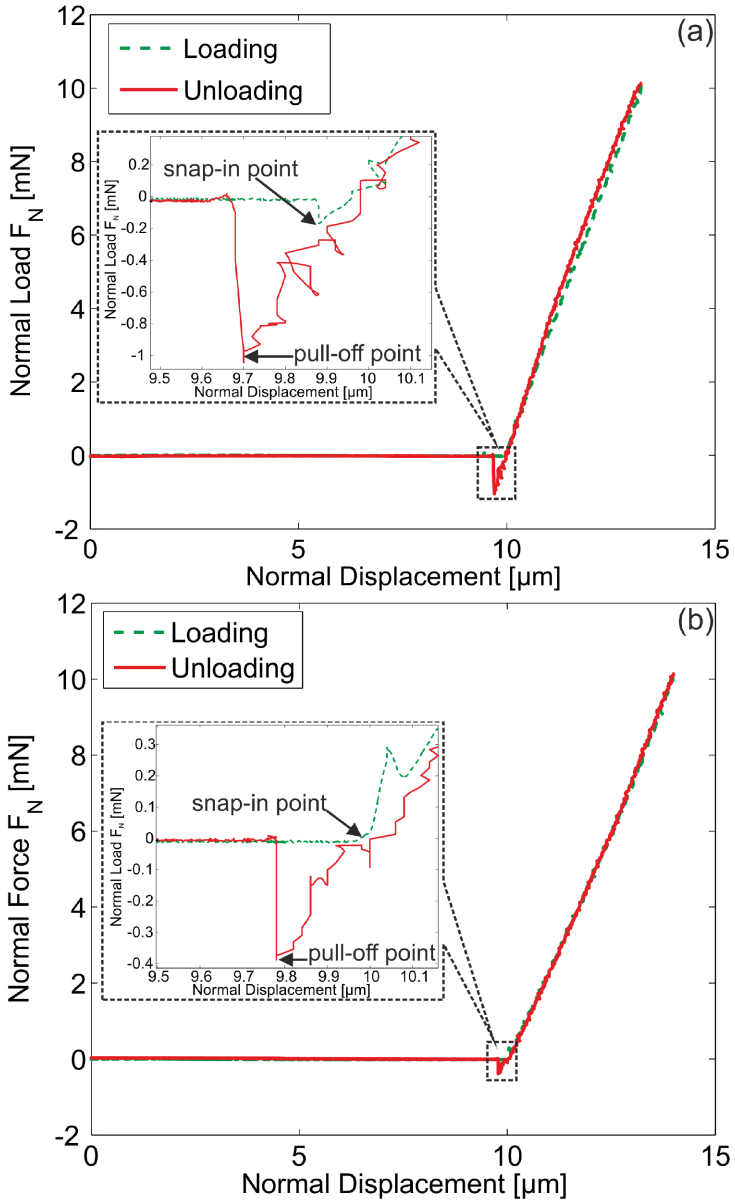

Figure 5.2: A typical force-displacement curve measured with VAFT for 5mm diameter Si ball against glass flat in (a) ambient (20°C, 1 bar and 45±5% RH) and (b) high vacuum (20°C, 10^{-6} mbar) conditions. The insets show the snap–in and pull–off points in both measurements.

A typical force-displacement curve measured on the VAFT between a 5 mm diameter Si ball and a glass flat surface is shown in Figure 5.2. The force-displacement curve in ambient (*20°C, 1 bar and 45±5% RH*) as well as in HV (*20°C, 10^{-6} mbar*) conditions is shown in Figure 5.2(a) and Figure 5.2(b), respectively. The inset of Figure 5.2 shows the snap-in and pull-off points as has been shown in the schematic representation in Figure 5.1. In order to compare and validate these measurements, similar measurements have been performed at TNO Eindhoven. It is important to mention that it was only possible to compare the measurements performed in ambient conditions at TNO since the setup present there is only capable of measuring in ambient conditions.

The measurements at TNO were performed on a combined nanoindenter and scratch tester from ASMEC GmbH (ASMEC's Universal Nanomechanical Tester UNAT). It consists of two measuring sensors, one for normal direction (nanoindenter) and the other for lateral direction (scratch tester). They work completely independent of each other and both with resolutions in the nanometre range. The indenter is mounted on the normal direction-measuring sensor, whereas the sample is placed on the lateral direction-measuring sensor. The UNAT has a displacement resolution of better than *1 nm* and the force resolution is better than *6 μN* [69].

The results of the measurements between a Si ball and a glass flat surface performed both on UNAT and VAFT are shown in Figure 5.3. The results of the pull-off measurements in ambient conditions from both test setups are comparable within the error margins. VAFT is designed to measure the adhesion force with a compliant flexure mechanism whereas the UNAT comprises a stiff construction. This can clearly be seen from the force-displacement curves shown in Figure 5.3 where the displacement required to apply the normal load of *10 mN* in UNAT is approximately *0.02 μm* and for the VAFT it is approximately *2.6 μm*.

The force measured in UNAT is with piezo force sensors whereas in VAFT it is measured with a capacitive sensor and FMM as explained in Chapter 3. The measurement conditions and sample preparations were kept similar as much as possible. Typical force-displacement curves from both test setups are shown in Figure 5.3. There are cycles of pull-off and snap-in during unloading of the ball from the flat surface in the measurements performed with UNAT. These cycles are formed due to a low unloading/retracting speed of UNAT as compared to the VAFT. A distinctive peak can be seen during unloading in the measurements performed with the VAFT giving the pull-off force. Several measurements have been compared and the results of both setups are similar. This shows that both test setups with different construction and measuring principles show similar results for the pull-off force.

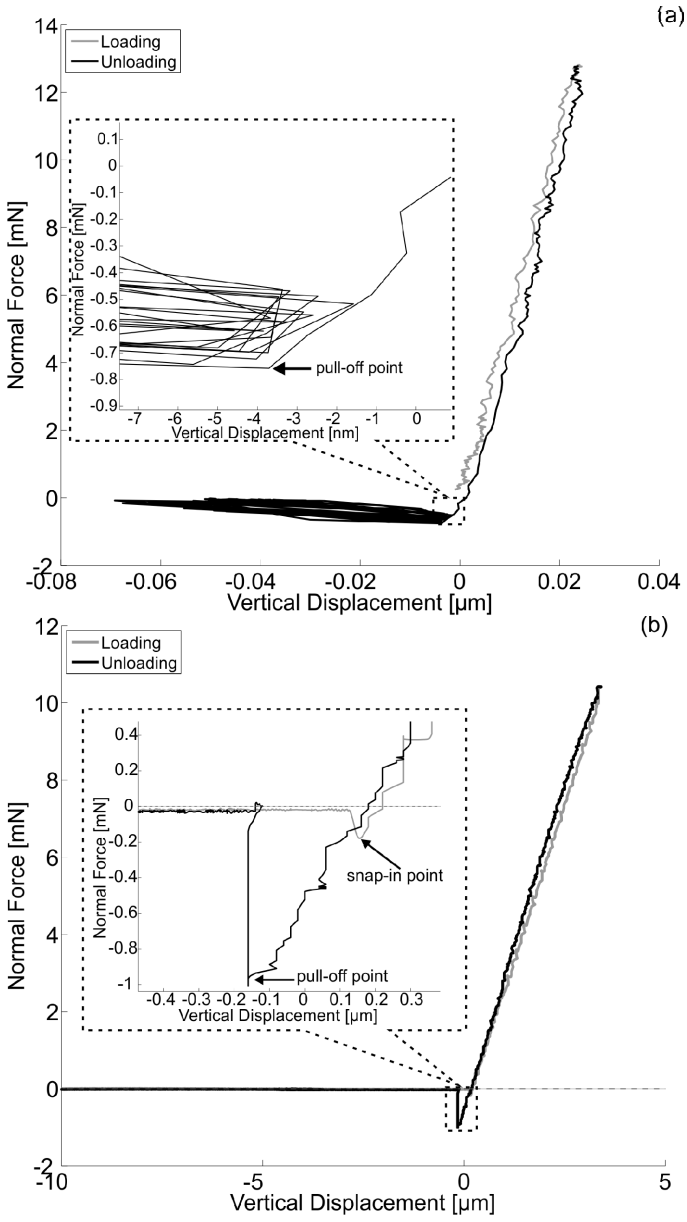

Figure 5.3: Typical force-displacement curves for measuring adhesion force in ambient conditions (20°C, 1 bar and 45±5% RH) for a 5 mm diameter Si ball against glass flat from (a) UNAT at TNO and (b) VAFT.

5.2.1 Sample preparation and inspection

The sample preparation for measurements performed with the VAFT and the UNAT is slightly different. The samples used in the experiments performed

with the VAFT were cleaned in an ultrasonic bath of acetone for *15 minutes*, rinsed with deionized water and then dried. This process has been used to clean the flat glass surfaces, sintered silica and sapphire tips and the *5 mm* diameter Si, SiO_2 and Al_2O_3 balls. The surfaces are inspected under the Keyence Confocal Microscope before the measurements are performed. The samples used in the experiments performed with UNAT are prepared in the same way as explained above but with a slight difference. Before the measurements are performed on UNAT any residues on the surfaces are removed by cleaning the surfaces gently using soaked (mixture of isopropanol and deionized water) and dry fibreless tissues.
For both measurement setups a smooth spot on the ball was located during the inspection of the ball and the same spot was used for the measurements. The adhesion measurements performed with VAFT in ambient conditions were performed before and after several days of pumping to high vacuum and no significant difference was found. Therefore, it can be concluded that the surfaces are clean and the measurements were performed between the materials of interest without any contaminants present on the surface.

5.3 Effects of relative humidity on adhesion force

The humidity dependence on the adhesion force was explained in section 4.2. A theoretical model showing the transitions in the adhesion force with the change in RH was discussed. Experimental validation of this model was required and therefore, adhesion experiments were performed on the VAFT using the adhesion force measurement procedure explained in section 3.5. A flat glass surface and the ball was cleaned and inspected by the process explained in section 0. The flat glass was placed on an XY positioning stage of the VAFT and the ball holder was mounted on the cantilever. The cantilever is mounted through the force measuring mechanism on the Z positioning stage as shown in Figure 3.1. The whole setup was placed in a vacuum chamber to control the RH. The RH was measured through a humidity sensor in the chamber, which can measure with an accuracy of *±5%*. The RH can be controlled by flushing liquid Nitrogen through a coil attached to one of the flanges of the chamber. This coil traps the water molecules present in the chamber by condensing them on the coil.
The measurement results for a *5 mm* diameter silicon ball and glass interface along with the calculated results from the model explained in section 4.2 are shown in Figure 5.4. The measurements were performed in ambient conditions before and after pumping the chamber down to 10^{-7} mbar for several days. The measured adhesion force during this process is well within the error margin

indicated in Figure 5.4. Furthermore, each measurement point consists of at least *10* adhesion measurements.

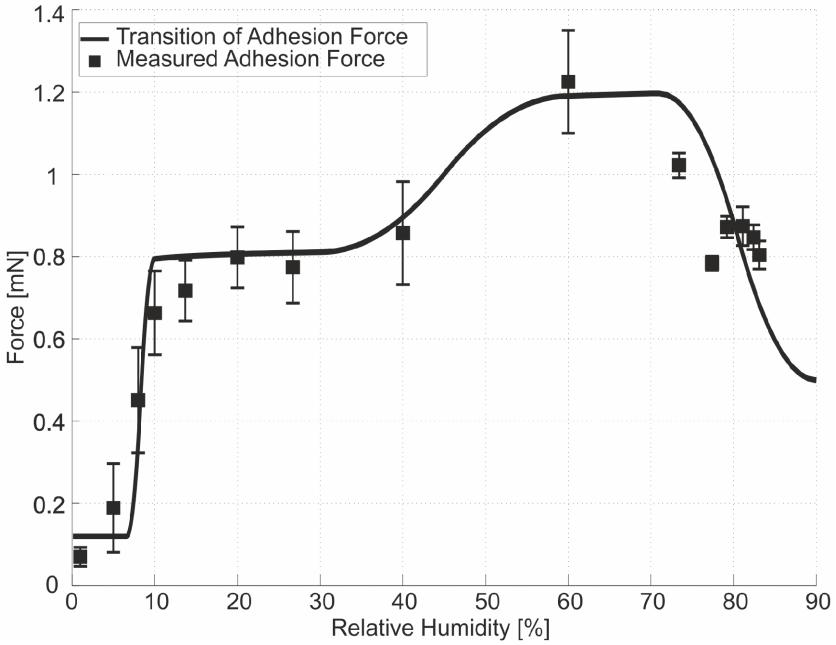

Figure 5.4: Simulation results for the adhesion force along with the measured adhesion force for a 5 mm diameter Si ball against a glass flat. The experimental and modelling results have been scaled when compared to the results shown in Figure 4.7.

The measurement points shown in Figure 5.4 at very low relative humidity and high relative humidity have a small error bandwidth as compared to the measurements between *5-60%* RH. The reason for this large bandwidth in this range could be because of the stochastic nature of the adsorption phenomenon resulting in non-homogeneous thick water layers on the surfaces. The first point in Figure 5.4 depicting the dry situation was measured when the system was pumped down to the pressure of 10^{-7} *mbar*. The pressure is then increased to 10^{-5} mbar and it can be seen that the adhesion force has increased with respect to the measurement performed at 10^{-7} *mbar*. The increase in pressure increases the RH in the chamber, and the adhesion force increases as the pressure is increased until 1 bar showing the formation of monolayers of water on the surfaces.

The measurement results as well as model results show the same trend, however, the magnitude of the adhesion force measured, as shown in Figure 5.4, is approximately *5* times less than the magnitude calculated with the model as shown in Figure 4.7. The main reason for this difference is that the model does not incorporate the surface roughness effects on the adhesion force. The surface roughness values of the SiO_2–glass interface are low, but the adhesion force is very sensitive to surface roughness [9, 26, 27, 70]. An adhesion

parameter θ was introduced, which is a function of the elastic modulus E, surface energy $\Delta\gamma$, asperity radius β and standard deviation of the surface roughness σ and is given by [70]:

$$\theta = \frac{E\sigma^{3/2}}{\beta^{1/2}\Delta\gamma} \tag{5.1}$$

If the value of the adhesion parameter is larger than *10*, the adhesion force significantly reduces from the adhesion force value measured between relatively smooth surfaces [70]. It has also been reported that the adhesion force reduces *2* orders of magnitude with a one order of magnitude change in rms roughness (i.e. *1–10 nm*) [9]. Similarly, the value of the adhesion force as a function of the rms roughness has been reported to be decreasing by a factor of *5* if the rms roughness is increased from *0.2–4 nm* and for higher roughness values it stabilizes [8, 26]. For the SiO_2–glass interface the value of the adhesion parameter reaches *10* when the rms roughness is between *1-3 nm*, taking the mean asperity radius between *10-500 μm*. The measured rms roughness of the Si ball is *2–3 nm* and the flat glass surface is *0.7–1 nm*, see Appendix B. Therefore, the equivalent roughness of the contact is higher than *1 nm*. There are small microcontacts present in the contact and, therefore, the real area of contact is much smaller than the nominal area of contact which reduces the pull–off force significantly. Furthermore, the capillary force and the van der Waals force scale with the radius of the spherical surface (here contacting asperities) [7]. As mentioned earlier, the measured adhesion force is a factor *5* less than the calculated adhesion force from the purposed model and this difference corresponds to the study reported by van Zwol et al. [9] and Ata et al. [8] where the relation between the rms roughness and the adhesion force has been established.

5.4 Normal load effects on adhesion force

It was explained in section 4.3 that theoretically there is an interdependent effect of normal load and contact time on the adhesion force. It is expected that the adhesion force will increase with the increase in normal load to the power of *2/3* if the surfaces are moved apart within a relatively short time span. To see this effect, the adhesion force measurements are performed by changing the applied normal load. The experiments were conducted by keeping a constant loading/unloading rate i.e. *385 μN/sec* and a constant contact time/rest time i.e. *5 sec*.

The normal load effects on the adhesion force were measured for a glass flat surface and *5 mm* balls of Silicon (Si), Silica (SiO_2) and Sapphire (Al_2O_3). The

measurements were performed in ambient (*20°C, 1 bar and 45±5% RH*) as well as in HV (*20°C, 10^{-6} mbar*) conditions. The normal load was increased from *10* to *50 mN* with a load step of *10 mN*. At each load step 5 measurements were performed.

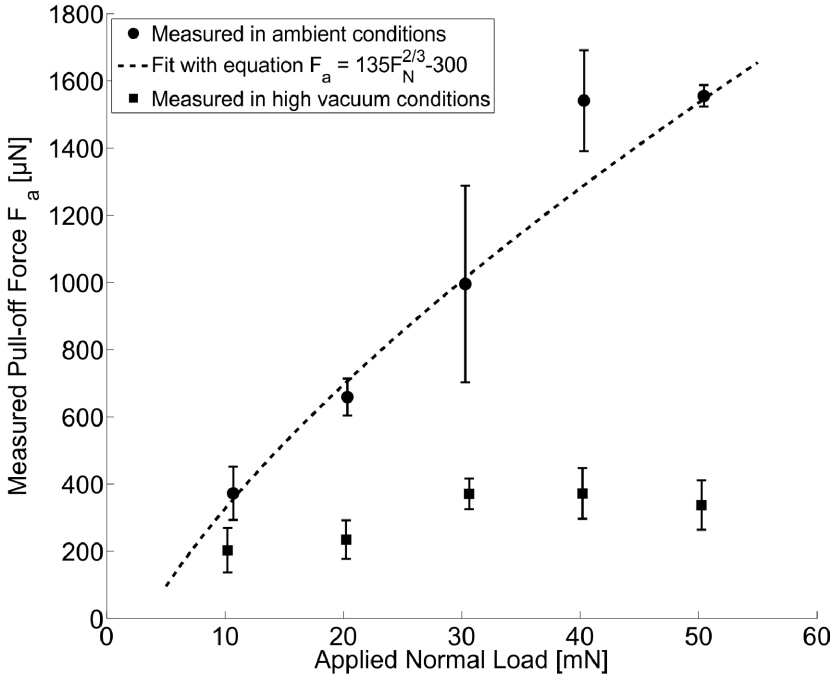

Figure 5.5: Adhesion force measurements for Si ball against glass flat surface in ambient (●) as well as in high vacuum (■) conditions.

The adhesion force measurement results between a Si ball and a flat glass surface are shown in Figure 5.5. It can be seen that the adhesion force does not change significantly with the normal load when the system is operating in HV conditions. However, when the same system is operating in ambient conditions the adhesion force increases with the power of *2/3* when the applied normal load is increased.

The reason for this increase in the adhesion force in ambient conditions is because of the transient effects present in the condensation/evaporation phenomenon. In ambient conditions water from the surroundings condenses around the contact and forms a meniscus. Due to the presence of this meniscus the adhesion force is increased significantly and the magnitude of this force is dependent on the radius of the meniscus, see Chapter 2. As the normal load is increased the meniscus radius increases and as the normal load is decreased it is expected that the meniscus radius will also decrease as can be seen from Eq. (4.5). However, the condensation time is generally lower than the evaporation time and since the loading/unloading rate has been kept the same, there is not

enough time for water to diffuse between the contact as was explained in section 4.3. Therefore, the radius of the meniscus increases with the increase in normal load to the power of *1/3* as given by Hertz in Eq. (2.24) in ambient conditions. This gives the *2/3* power dependence of capillary force on the normal load as can be seen from Eq. (4.5) and which has been expected as mentioned in section 4.3. It is important to mention here that the contact pressures are less than 100 MPa, so it is not expected to have plastic deformation of the surfaces. Therefore, this load dependency is due to the presence of a meniscus.

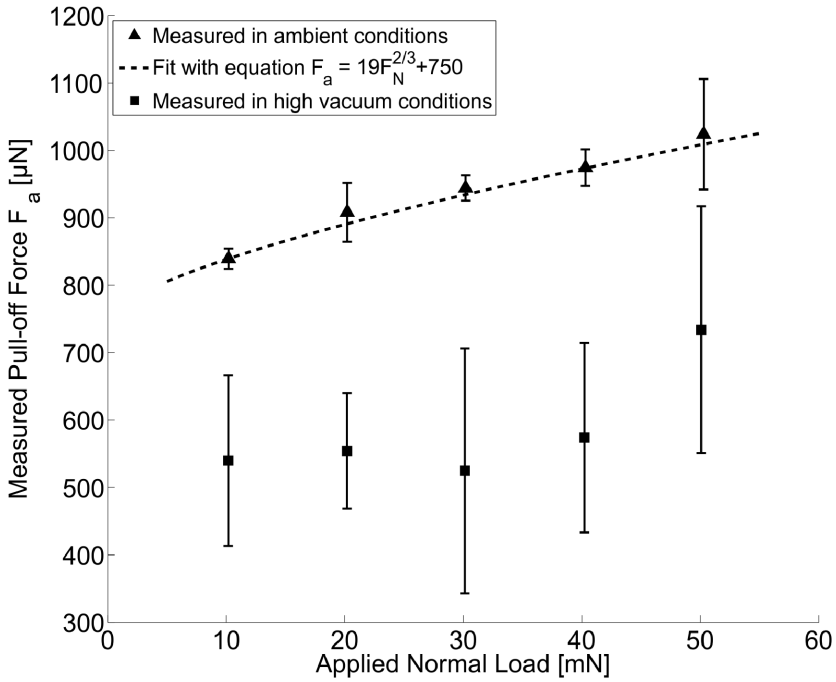

Figure 5.6: Adhesion force measurements for SiO_2 ball against a glass flat surface in ambient (▲) as well as in high vacuum (■) conditions.

Similarly, adhesion measurements were performed between the SiO_2 ball and a flat glass surface in ambient as well as in HV conditions. The results are shown in Figure 5.6 and similar effects can be seen as shown in Figure 5.5. The power law curve fit on the adhesion measurements in ambient conditions also shows the *2/3* power dependence on the normal load. This *2/3* power dependence, as explained before, is due to the power dependence of the capillary pressure force on the meniscus radius as shown in Eq. (4.5).

The adhesion measurements were also performed using a *5 mm* diameter Sapphire (Al_2O_3) ball in contact with a glass flat surface. The measurement results are shown in Figure 5.7. A similar increasing trend in the adhesion force in ambient conditions is observed when the load is increased, as shown in

Figure 5.5 and Figure 5.6. In HV conditions, again a constant adhesion force is found with increasing normal load.

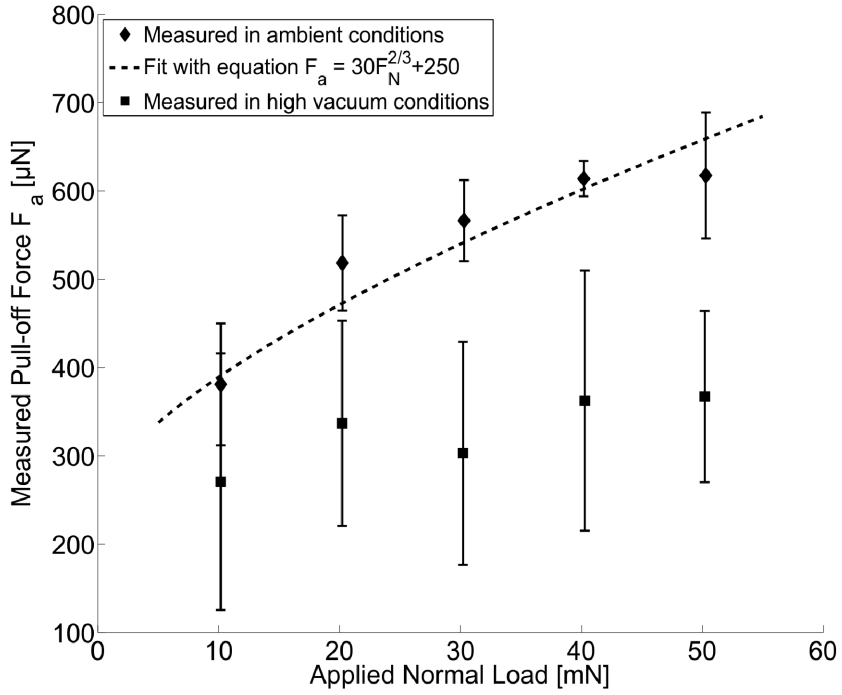

Figure 5.7: Adhesion force measurements for Al_2O_3 ball against glass flat surface in ambient (◆) as well as in high vacuum (■) conditions.

It can be seen that the value of the adhesion force is reduced for Al_2O_3 ball against glass. The reason for this decrease can either be due to the different value of work of adhesion for Al_2O_3-glass interface or due to the higher roughness of the Al_2O_3 ball. From Table 3.1 we can see that the surface energy values of Al_2O_3 and SiO_2 are very close to each other, therefore the difference in work of adhesion might not be expected. However, from Appendix B we can see that the roughness of the two balls is significantly different and a slight increase in the rms roughness of the system under study can decrease the adhesion force significantly, as explained in section 2.2.2.1 and section 5.3.

5.5 Contact time effects on adhesion force

It was mentioned that it is very important to take the time effects into consideration when studying the adhesion force. In the previous section it was shown that the shorter retraction times influences the behaviour of adhesion force as a function of normal load. Similarly, in section 4.3 an exponential function was introduced to define the contact time effects on the adhesion force

in ambient conditions since the meniscus formation is a thermally activated process. Therefore, experiments have been performed to study the behaviour of adhesion force by keeping the normal load constant at 10 mN.
The effect of contact time or rest time on the adhesion force has also been studied for *5 mm* diameter Si, SiO_2 and Al_2O_3 balls against a smooth flat glass surface. The measurements were performed in ambient conditions for all three materials and in HV for SiO_2. The contact time or rest time is defined as the time when the surfaces are kept in contact under a desired normal load. The contact time was varied from *10 msec* to *1000 sec* and the adhesion force is measured at each time step. The ambient conditions have been defined as *20°C* and *45±5% RH*. The results for SiO_2-glass interface when operating in ambient conditions as well as in HV conditions are represented in a semi-log plot as shown in Figure 5.8.

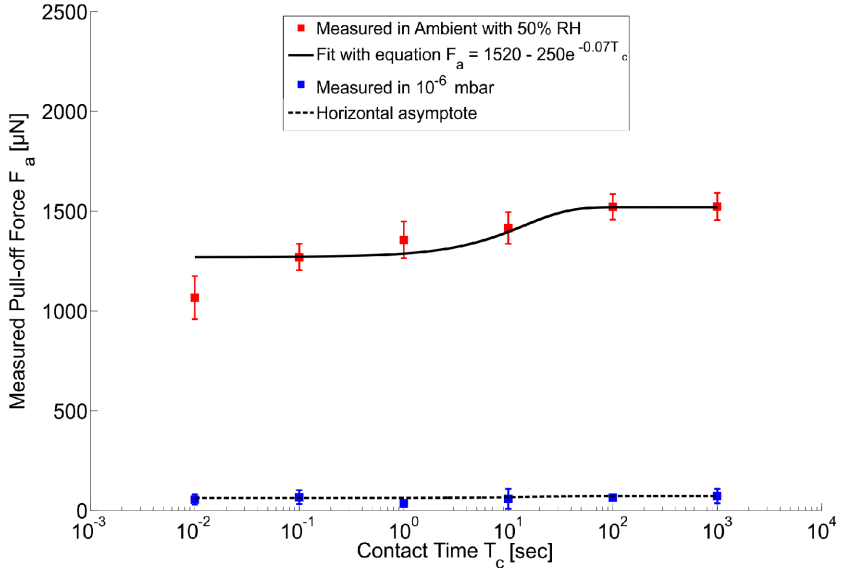

Figure 5.8: Adhesion force measurements for 5 mm diameter SiO_2 ball against glass flat surface in ambient (■) as well as in high vacuum (■) conditions when the contact time is changed and the normal load of 10 mN is applied. The exponential fit shows that the adhesion force is changing with the contact time in ambient conditions.

It can be seen that there is no significant effect of the contact time on the measurements performed in HV conditions, the adhesion force remains constant. However, in ambient conditions the adhesion force increases and stabilizes after certain period of time. This shows that a change in adhesion force is only possible in ambient conditions where capillary/meniscus forces are dominant. Therefore, the contact time dependency of the adhesion force is due to the transient effects present in the meniscus formation. In section 4.3 the model for contact time dependence of the adhesion force in ambient conditions

was discussed. It has been shown that the effect of contact time on the adhesion force can be described by an exponential equation shown in Eq. (4.13). This equation has been used to fit the measurement data and it can be seen in Figure 5.8 that the model explains the experimental results very well. It can also be seen that in ambient conditions the adhesion force increases after *1 sec* and stabilizes after *100 sec*.

Similar experiments were performed with *5 mm* Si and Sapphire balls in ambient conditions. The results were compared with the adhesion measurements performed with the SiO_2 ball and are shown in Figure 5.9. It can be seen that all the materials follow the same exponential trend and the increase in the adhesion force takes place between *1 sec* and *100 sec* of the contact time. It was discussed in section 2.2.2.2 that the size of the sphere has an influence on the stabilizing contact time. Stabilizing contact time is the time when the capillary condensation is in equilibrium and there is no further increase in adhesion force with the increase in contact time. For a small-sized sphere the stabilizing contact time is also smaller and as the size increases the stabilizing contact time increases. It has been reported that the stabilization times for a *100 µm* sphere is in the order of *100 sec* [9]. However, the stabilization cannot be clearly seen in [9] and can be smaller than *100 sec*. In another study the stabilization time for a *1 mm* silicon ball against a silicon flat surface has been reported to be in the order of *100 sec* [12]. The stabilization times measured with *5 mm* diameter spheres are in the same order as reported in [12], i.e. *100 sec*, and can be seen from Figure 5.9.

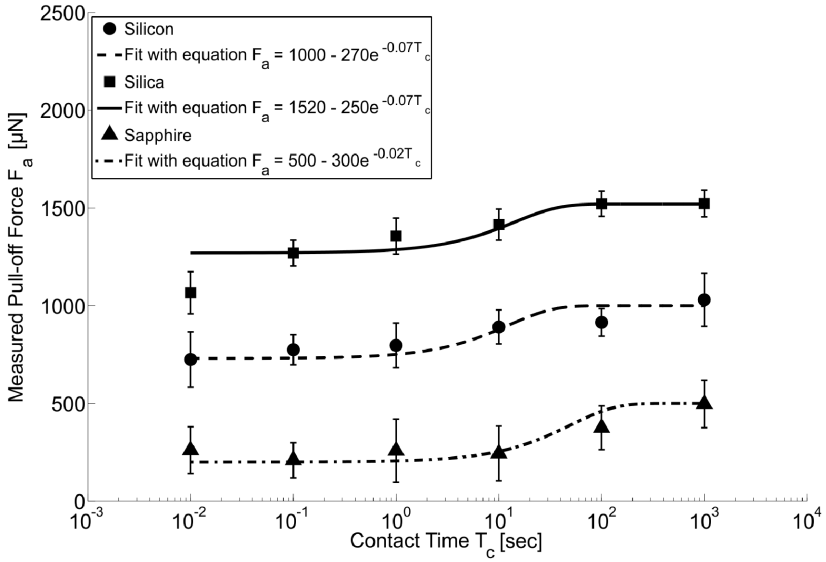

Figure 5.9: Adhesion force measurements for SiO_2 (■), Si (●) and Al_2O_3 (▲) balls against glass flat surface in ambient conditions when the contact time is changed and the normal load of 10 mN is applied. The exponential fits for each material show the changing trend of the adhesion force with the contact time T_c.

It can be seen from Figure 5.9 that the adhesion force for relatively rough contact (Sapphire-glass interface) is smaller than that of the smooth contact (Si-glass or SiO_2-glass interface). The reason for this is that for rough surfaces only the asperities make contact and at low contact times the meniscus is only formed at the asperities where the stabilization times are in the order of a few milliseconds [9]. However, if the contact time is large enough to condense more water around the asperities, then the probability of meniscus formation around more asperities increases. Therefore, for this reason a similar trend is seen even with the rough contact as can be seen for the smooth contact, but with a lower magnitude of adhesion force. The increase in the adhesion force with the contact time for all the material combinations is between *25-30%* of the average value at lower contact times.

5.6 Size and roughness effects on adhesion force

The previous sections dealt with adhesion force measurements between sphere-flat interfaces using the same-sized sphere having similar surface energies, but different rms roughness. The effects of normal load and contact time on the adhesion force were discussed. It was notd that the adhesion force reduces significantly if there is a slight change in the surface roughness values. Many studies have dealt with the effects that surface roughness has on the adhesion force, as was explained in section 2.2.2.1.

If we look at the theory of van der Waals and capillary force, it can be seen that these forces are linearly dependent on the radius of the ball as has been shown in Eq. (2.10) and Eq. (2.18). In section 4.2.3 a theoretical model to calculate the adhesion force as a function of RH was discussed. The maximum estimated value of the adhesion force for a *20 nm* and a *2.5 mm* radii balls has been shown in Figure 4.6 and Figure 4.7 respectively. It can be seen that the maximum value of the adhesion force for a *20 nm* radius ball is approximately *50 nN*. Similarly, simulations were performed for a *2.5 mm* radius ball and the maximum adhesion force is approximately *6 mN*. The two balls differ in size from each other by a factor of 1.25×10^5. If we look at the values of the adhesion force for these surfaces a similar factor can be seen which shows the linear dependence of the radius of the ball on the adhesion force. It is important to mention here that the adhesion model does not incorporate the roughness effects of the surfaces in contact. Therefore, the difference in the adhesion force for the same material is due to the difference in the radius of the ball.

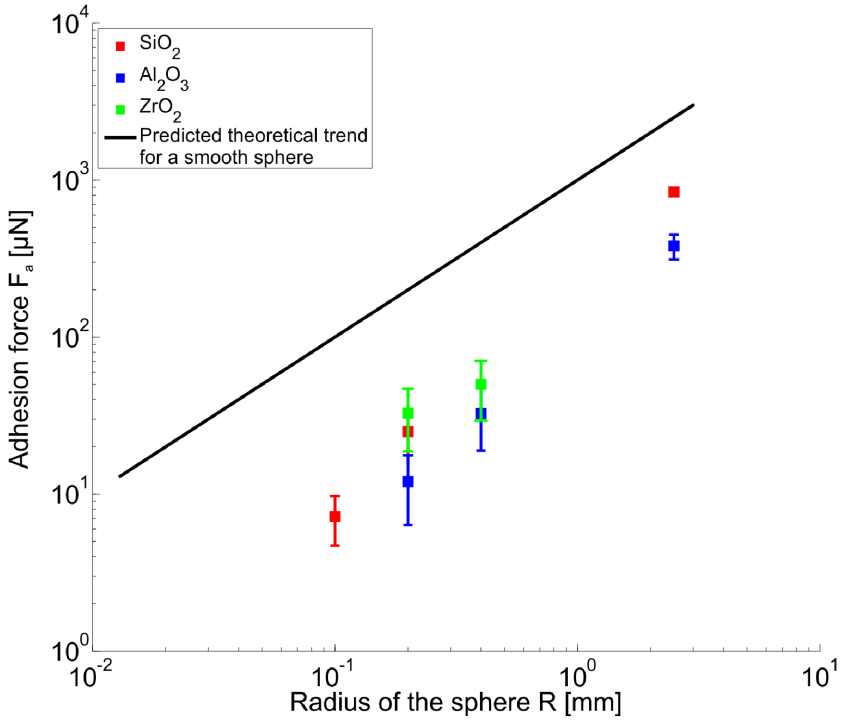

Figure 5.10: Adhesion force measurements for SiO_2 (■), Al_2O_3 (■) and ZrO_2 (■) balls of different sizes against a glass flat surface in ambient conditions with 10 mN applied normal load and contact time of 5 sec. The predicted theoretical trend is also shown for comparison where the change in slope of the measured set of data is due to the surface roughness effects.

Measurements have been performed to study the size and roughness effects on the adhesion force. A normal load of *10 mN* and a contact time of *5 sec* was used for all the measurements. Balls of different radii of the same material were used to study this effect. SiO_2 with the radii of *2.5 mm, 0.2 mm* and *0.1 mm* was used against the flat glass. The *2.5 mm* ball is a lens of fused quartz and *0.2 mm* and *0.1 mm* radii are obtained on grinded and sintered fused silica tips. Similarly, the sapphire balls of *2.5 mm* and *0.4 mm* radii and a sapphire sintered tip of *0.2 mm* radius were used to measure the size effects on the adhesion force. Furthermore, Zirconia (ZrO_2) balls of *0.4 mm* and *0.2 mm* were used to measure the adhesion force. A glass flat surface was used as a counter surface in all the experiments. The rms roughness of the spherical surfaces is fairly different and it was only possible to get very smooth millimetre sized balls but for smaller radii the surface quality cannot be improved. Therefore, a combined effect of size and roughness has been studied. The size effects for different materials are shown in Figure 5.10 where the measurements have been plotted on a log-log scale.

5.7 Summary

The effect of different parameters on the adhesion force was discussed and experiments were performed to study these parameters. The results show that the adhesion force changes when the RH is changed from 1% to 90% RH. The adhesion force first remains constant at very low RH (HV conditions) showing the solid-solid contact and then increases to another constant level as the RH increases. The adhesion force remains constant within a certain band of RH where the water is present in the form of ordered layers and increases again to another level where the capillary force contributes to the total adhesion force. The experimental results were compared with the newly developed theoretical model and considering the roughness effects on the adhesion force, the model fits very well with the experimental results. Similarly, the effect of normal load on the adhesion force in ambient and HV conditions was studied by performing experiments between Si, SiO_2 and Al_2O_3 spheres against a glass flat surface. It was discussed that the adhesion force remains unchanged when measured in HV conditions. However, in ambient conditions the adhesion force for all the material combinations increases with an increase in the normal load. This is due to the increase in the meniscus radius with the increase in the normal load, which is in agreement with the theory.

Contact time effects on the adhesion force have also been experimentally studied for Si, SiO_2 and Al_2O_3 spheres against a glass flat surface. The measurements were performed by applying a constant normal load and by increasing the contact time from *10 msec* to *1000 sec*. An exponential behaviour was observed in the adhesion force with the increase in the contact time. This is because the capillary condensation is a thermally activated process and as the contact time increases more water from the surroundings condenses in the contact. This phenomenon will increase the magnitude of the adhesion force. The water condensation then reaches an equilibrium where the adhesion force stabilizes after longer periods of time.

Furthermore, the effects of radius of a ball and the effects of surface roughness were discussed. It was shown that the adhesion force changes linearly with the change in the radius of the ball. However, an increase in surface roughness decreases the adhesion force significantly.

Chapter 6
PRE-SLIDING BEHAVIOUR OF SINGLE ASPERITY CONTACT[1, 2]

6.1 Introduction

The previous chapters dealt with adhesion force models and their validation through experiments. In this chapter friction modelling and specifically static friction modelling and its experimental validation will be discussed. The transition from pre-sliding to sliding contact is relevant for accurate positioning mechanisms, whose application can be found in e.g. positioning stages of scanning electron microscopes. To understand the pre-sliding behaviour of the surfaces in contact, the understanding of this phenomenon on asperity level is important. Therefore, pre-sliding behaviour of a single asperity contact is the first step in understanding this behaviour. A lot of analyses and studies have been done on different materials and geometries [44]. Partial stick and slip occurrences in a single asperity contact can be critical in micro and nano scale mechanisms. The load applied in the tangential direction on a single asperity contact will induce shear stresses in the contact, and static and kinetic friction forces must be considered [71].
In this chapter, the pre–sliding behaviour of a single asperity contact between a smooth ball in contact with a smooth flat surface will be discussed when the contact pressures are kept below 100 MPa. In section 6.2 the theoretical model to calculate the shear stress and the preliminary displacement in the contact is discussed. In section 6.3 the materials and methods used in the experiments are explained. Experiments were conducted to verify the model and are discussed in section 6.4. The experimental results are compared with the theory for contact pressures below 100 MPa using 2.5 mm radius Silicon and Silica balls with an applied normal load between 10-90 mN. This value of contact pressure is chosen to make sure that the experiments have been performed without wear or plastic deformation of the surfaces. The pre–sliding behaviour explained by

[1]Reproduced from: M.A. Yaqoob, A. Winogrodzka, H.R. Fischer, E.R.M Gelinck, M.B. de Rooij and D.J. Schipper, Pre-sliding behaviour of single asperity contact, Submitted to: *Tribology Letters*, 2012.
[2]Reproduced from: M.A. Yaqoob, M.B. de Rooij and D.J. Schipper, Design of a Vacuum Based Test Rig for Measuring Micro Adhesion and Friction Force, *High performance structures and materials*, VI, pp. 261-274, 2012.

Cattaneo and Mindlin is based on non-adhesive contact since the Hertz theory has been used for calculating the contact area [14, 15]. Furthermore, the trend of normal load dependent static friction force and preliminary displacement has been discussed using Hertz's and Mindlin's theory.

6.2 Theoretical background

The pre-sliding and static friction force behaviour at asperity level between a smooth ball and a smooth flat surface at different normal loads, as well as friction behaviour during full slip has been studied. Experimental results found in the literature [72-74] showed generally good agreement with the theoretical Cattaneo-Mindlin model [14, 15]. However, the contact pressure which was investigated in those measurements was is in the range of *0.3 GPa* for a brass ball of radius *9.5 mm* against steel with an applied normal load in the range of *150 N* and *330 N* [73]. Similarly, using a Si_3N_4 probe of *20 nm* radius against a similar material with an applied normal load of *118 nN* (including adhesion), the applied contact pressure is *10 GPa* [72]. At low pressures the validity of Mindlin's model is not known. It could be that the validity of this model is limited because of the effect of interfacial layers.

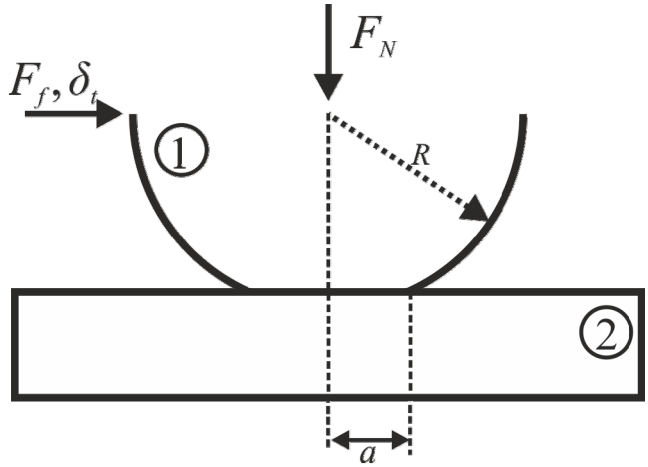

Figure 6.1: A ball in contact with a flat surface depicting a single asperity contact. The radius of the contact a due to applied normal load, applied tangential force F_f and preliminary displacement δ_t is shown.

A smooth ball in contact with a smooth flat surface using an applied normal load (F_N) defines the single asperity contact as shown in Figure 6.1. If an increasing tangential force (F_f) is applied to this contact, the tangential traction (τ) as well as the tangential displacement parallel to the surface is generated [15,

28]. If this applied tangential force changes direction, then a cycle of tangential displacement can be observed, as shown in Figure 6.2.

Under constant applied normal load the tangential force F_f is applied starting from point *O*. The tangential force is increased from *0* to F_t, where, F_t is the maximum tangential force when full slip occurs, i.e. $F_t = \mu \times F_N$, and μ is the coefficient of static friction (COSF). The ball starts to slip partially from point *O* to *A* after which the ball is in full slip regime. The tangential displacement from point *O* to *A* is defined as preliminary displacement (δ_t). During this increase in tangential load the sticking area between two bodies decreases and the slipping area increases till full sliding starts at point *A*.

If the direction of the tangential load is changed from F_t to $-F_t$ then the direction of the tangential displacement is also changed and is shown by the line *ABCD*. At point *D* full slip occurs and the line *ABCD* shows the partial slip in the contact. Similarly, if the direction of the tangential load is again changed from $-F_t$ to F_t i.e. from point *D* to *A* through point *E* and *G*, then the direction of the tangential displacement also changes following the line *DEGA*. The difference between points *O*, *B* and *E* can be explained by hysteresis in the displacement. Similarly, the difference between points *O*, *C* and *G* can be explained by the friction force hysteresis.

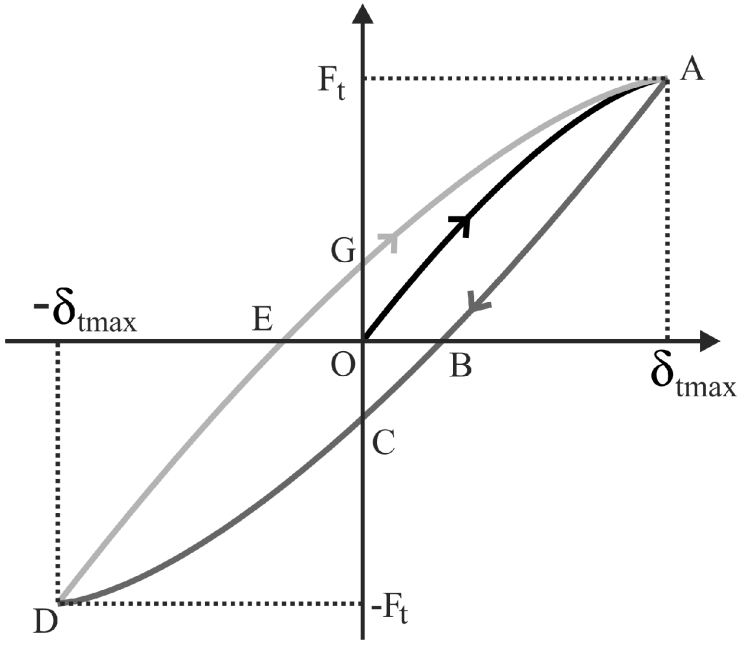

Figure 6.2: Tangential load against displacement showing an oscillating tangential load on a contact when loaded with a constant normal load. The maximum tangential load just before slipping F_t is also shown.

For a ball in contact with a flat as shown in Figure 6.1, the circular area with contact radius a can be calculated using Hertz theory [28]. The preliminary displacement δ_t, when a constant normal load F_N is applied, can then be calculated as [15]:

$$\delta_t = \frac{3 \cdot \mu \cdot F_N}{16 \cdot a \cdot G^*} \left[1 - \left(1 - \frac{F_f}{\mu \cdot F_N} \right)^{2/3} \right] \tag{6.1}$$

Where, G^* is the reduced shear modulus and F_f is the increasing applied tangential load. Eq. (6.1) shows that the preliminary displacement is dependent on the material properties, applied normal load, applied tangential load, coefficient of static friction and contact radius. Furthermore, the contact radius is also dependent on load, elastic properties and radius of the ball.
Figure 6.3(a) presents a comparison of the calculated friction force loops shown in Figure 6.2 between two different materials when the same normal load is applied. The results for Silicon (Si) and Silica (SiO_2) balls are shown. Because the maximum tangential force F_t is lower for SiO_2-glass interface as compared with Si-glass interface, the tangential displacement is also lower for SiO_2-glass interface. The difference in tangential displacement for SiO_2 and Si is about 1 nm. The properties of the materials used for these simulations are shown in Table 6.1.

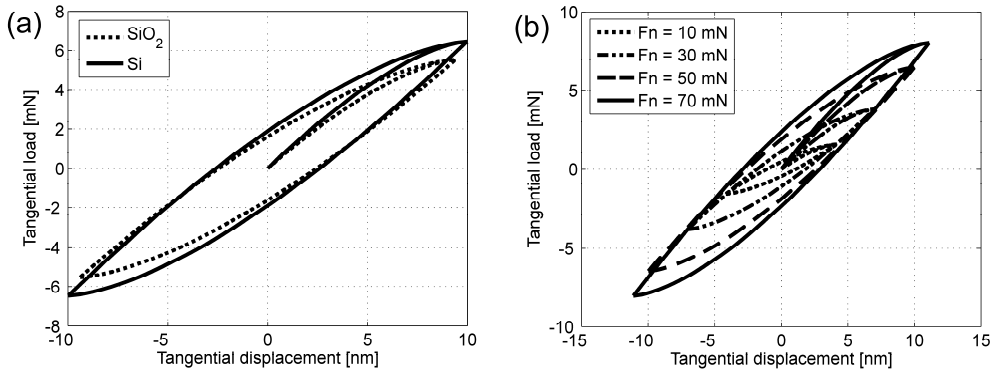

Figure 6.3: The force-displacement curves between the tangential load and the tangential displacement for (a) SiO_2† and Si† against a flat glass surface when a normal load of 50 mN is applied and b) for Si, normal load is changing from 10-70 mN.

†Material properties used for simulation are shown in Table 6.1

In Figure 6.3(b) the friction force loops for the same material loaded with different normal loads is shown. It can be seen that the maximum tangential force and the corresponding tangential displacement increases with an increase

in the applied normal load in accordance with Eq. (6.3) and can also be seen from the equation given by Bowden and Tabor [75]:

$$F_t = \tau \cdot A \tag{6.2}$$

Eq. (6.2) is applicable to a single asperity contact where there is no ploughing. When the applied normal load is *10 mN*, the preliminary displacement can be calculated to be *4 nm* and is increasing with the increase of normal load for the Si-glass interface as shown in Figure 6.3(b). When the applied normal load is increased to *70 mN* the resulting preliminary displacement for the Si-glass interface is *11 nm*. The variation in tangential displacement depends on different conditions and parameters. It can be seen from Eq. (6.1) that a material with low elastic modulus has a higher preliminary displacement as compared with a material of high elastic modulus. An interface with low COSF yields a lower value of tangential displacement as compared with a material combination with high COSF. In Figure 6.3(a) the value of tangential displacement for SiO_2-glass interface is lower than that of Si-glass interface, although Si is stiffer than the SiO_2. The reason for this is due to the lower value of COSF for the SiO_2-glass interface as compared with the Si-glass interface, as discussed in section 6.4.2.

Considering a single asperity contact, according to Hertz theory [28] the contact area is proportional to the applied normal load to the power of *2/3* as shown in Eq. (6.3):

$$A = \pi \cdot \left(\frac{3}{4} \cdot \frac{R}{E^*} \right)^{2/3} \cdot F_N^{2/3} \tag{6.3}$$

Where, R is the radius of the ball in contact with the flat surface, E^* is the reduced elastic modulus of the ball and the flat surface. The normal load dependency of friction force given by Eq. (6.2) and assuming a constant shear stress in Eq. (6.3) gives the relation $F_t \propto F_N^{2/3}$. The coefficient of static friction (COSF) μ is defined by Eq. (6.4):

$$\mu = \frac{F_t}{F_N}, \Rightarrow \mu \propto \frac{F_N^{2/3}}{F_N}, \mu \propto F_N^{-1/3}. \tag{6.4}$$

This proportionality is valid assuming a constant shear stress τ of the interface. Therefore, the coefficient of static friction is proportional to the applied normal load to the power of *-1/3* as shown in Eq. (6.4). However, as explained before, the Hertz theory does not incorporate adhesion effects which are important to consider at low applied normal loads as explained by Johnson [34]. Johnson–

Kendall–Roberts (JKR), Derjaguin–Muller–Toporov (DMT) and Maugis–Dugdale M–D theories are a few examples of incorporating adhesion effects. A comparison of contact area trends for Hertz, JKR and DMT models is shown in Figure 6.4 for a Si ball of 5 mm diameter. The normal load dependency of the contact area as explained in Eq. (6.3) by Hertz remains more or less the same in the JKR and DMT theories. Therefore, to extract the normal load dependency of the contact area even when adhesion plays an important role, the Hertz theory can be used. Similarly, the relationship between the maximum preliminary displacement δ_{tmax} and the applied normal load can be given as:

$$\delta_{t\max} = \frac{3 \cdot F_t}{16 \cdot a \cdot G^*} \Rightarrow \delta_{t\max} \propto \frac{\mu \cdot F_N}{a}, \delta_{t\max} \propto \frac{F_N^{-1/3} \cdot F_N}{F_N^{1/3}}, \delta_{t\max} \propto F_N^{1/3}. \quad (6.5)$$

Where, δ_{tmax} is directly proportional to the maximum tangential load at the point of slip F_t and inversely proportional to the contact radius a. The COSF is proportional to the applied normal load to the power of *-1/3* and the contact radius is proportional to the applied normal load to the power of *1/3*, this gives us the δ_{tmax} proportional to the applied normal load to the power of *1/3* as shown in Eq. (6.5).

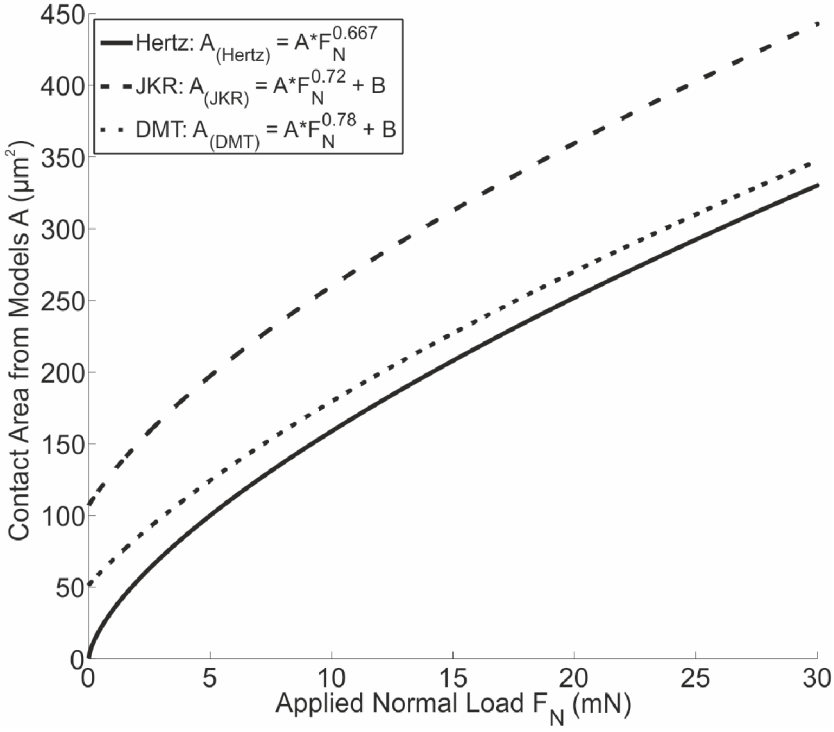

Figure 6.4: A comparison of the contact areas calculated using Hertz, JKR and DMT models for a Si ball of 5 mm diameter against a glass flat surface.

The maximum contact stiffness in tangential direction k_t when there is zero applied tangential force i.e. $F_t = 0$ is given by [15]:

$$k_t = 8G^* a \tag{6.6}$$

The shear stress at a particular value of the contact area for the stick and slip zones when the tangential load is increasing is given by [15, 28]:

$$\tau(r) = \begin{cases} 3 \cdot \mu \cdot \dfrac{F_N}{2 \cdot \pi \cdot a^3} \cdot \left(a^2 - r^2\right)^{1/2} & \text{if } s \le r \le a \quad \text{Slip} \\ 3 \cdot \mu \cdot \dfrac{F_N}{2 \cdot \pi \cdot a^3} \cdot \left[\left(a^2 - r^2\right)^{1/2} - \left(s^2 - r^2\right)^{1/2}\right] & \text{if } 0 \le r \le s \quad \text{Stick} \end{cases} \tag{6.7}$$

Eq. (6.7) is used to find the tangential traction $\tau(r)$ when the ball-flat contact is loaded with a certain normal load F_N and the tangential load is increased. Here, a is the contact radius shown in Figure 6.1, s is the radius of the stick zone and r is the instantaneous value of the radius defined in the Eq. (6.7). Figure 6.5 shows the tangential traction distribution when the tangential load is increasing. Assuming point K on line OA (showing the increase in the tangential load) in Figure 6.5(a), the tangential load at this point is $F_t/2$ and the tangential displacement is δ_t^*. The corresponding tangential traction distribution as a function of r is shown in Figure 6.5(b). At point K the contact is in partial stick condition and the radius of the stick zone s and the annulus of slip a-s are shown. If the tangential force is increased till point A the contact is in full slip condition and radius of the stick zone is not present anymore.

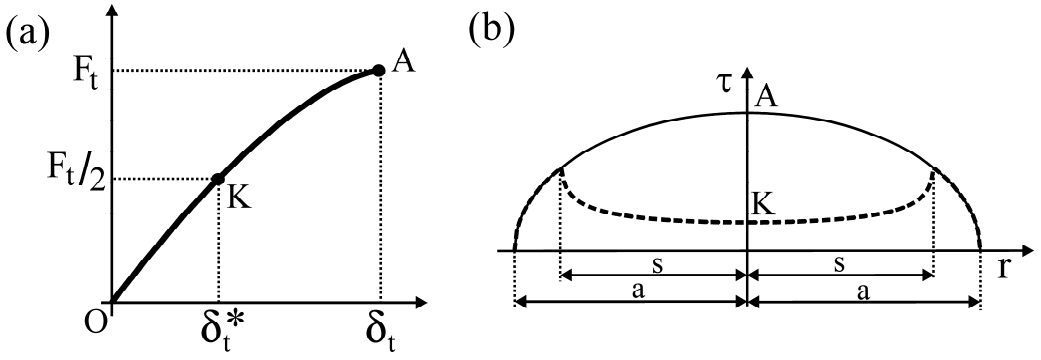

Figure 6.5: (a) Tangential force against tangential displacement showing only the forward scan. (b) Tangential traction against radial distance showing the partial stick and full slip conditions. The radius of the stick zone s and the annulus of slip a-s is also shown.

For one cycle of oscillating tangential load the tangential traction is changing in magnitude as well as in direction depending on the magnitude and direction of the tangential load. This change in the tangential load will also influence the area of the stick zone and the annulus of slip as shown, in Figure 6.6(b). In Figure 6.6(a) a similar cycle that has been shown in Figure 6.2 is shown and in Figure 6.6(b) the corresponding tangential traction is shown.
At point *O* there is no applied tangential load and consequently there is no traction. As the tangential load is increased the tangential traction starts to increase and the radius of the stick zone starts to reduce from *a* to *s* as shown in Figure 6.6(b). At point *K* the tangential traction is shown with a certain value of the radius of the stick zone and annulus of slip. The tangential traction is considered to be positive when the contact is loaded during a forward scan. Point *L* is taken at the same tangential load as point *K*, but on the curve produced during a backward scan. The corresponding tangential traction is also shown and is considered to be negative. It can be seen that the values of the radius of the stick zone and annulus of slip are different than at point *K*. Similarly, the tangential traction at points *M*, *N* and *P* has been calculated and been shown in Figure 6.6(b). Point *A* and *D* are the points on the brink of gross slip and the tangential traction at these points is considered to be the maximum tangential traction to break the contact.

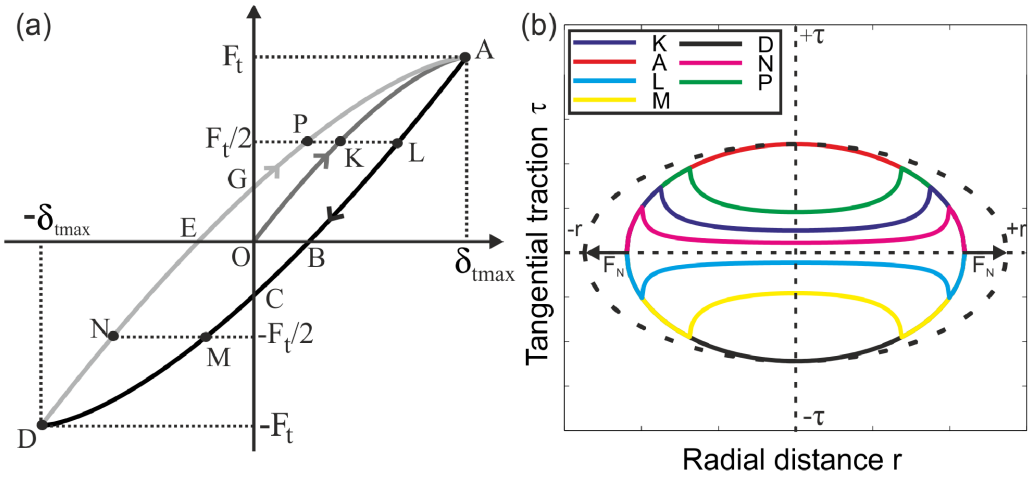

Figure 6.6: (a) Oscillating tangential load against displacement showing points K, L, M, N and P where the tangential traction has been calculated. (b) The tangential traction as a function of radial distance calculated at different points.

If we use the normal load dependence of the contact radius *a* and COSF μ in the centre of the contact, then at point *A* from Eq. (6.7) the maximum shear stress is independent of the normal load. Therefore, by increasing the normal load the radial distance increases and the shear stress remains constant as shown in Figure 6.6(b) with the dotted ellipse. This inference has also been reported in

the literature [76, 77]. So, whatever the actual value of the tangential load, the shear stresses are determined by the ellipses shown in Figure 6.6(b). This representation will also be used in section 6.4.4.

6.3 Materials and methods

Friction experiments have been performed to study the pre-sliding behaviour of a single asperity contact as shown in Figure 6.1. Three different materials have been used to study this behaviour and the material properties of these materials are given in Table 6.1.
In Table 6.1 R is the radius, E is the Young's modulus, v is the Poisson's ratio, G is the shear modulus, γ is the surface energy and R_q is the rms surface roughness. It can be seen from the values of R_q that smooth surfaces have been used in the measurements to simulate a single asperity contact. The experiments have been performed on a combined nanoindenter and scratch tester from ASMEC GmbH (ASMEC's Universal Nanomechanical Tester UNAT) which was explained in section 5.2.

Table 6.1: The material properties of the materials used in the friction force experiments.

Materials	R (mm)	E (GPa)	v (-)	G (GPa)	γ (mJ/m^2)	R_q (nm)[†]
Silicon (Si)	2.5	112	0.28	44	44.1±3.1[*]	2-3
Silica (SiO_2)	2.5	73.6	0.17	31.4	44.1±3.1	3-5
Sapphire (Al_2O_3)	2.5	462.6	0.309	144.3	41.1	8-10
Float glass	∞	64	0.2	26	83.4	0.7-1

[*] Surface energy of SiO_2 because of oxide layers present on the surface

[†] Surface roughness values are shown in Appendix B

The samples were prepared by adapting the procedure explained in section 0. The ball was placed in a mechanically fastened ball holder and a clean smooth spot on the ball was checked under a confocal microscope. The ball holder was then mounted inside the UNAT after finding a clean smooth spot on the flat sample as well. At each loading point *5 cycles* of friction measurements were performed. Each cycle consists of about *100 nm* of scan length in forward direction and about *100 nm* in the backward direction from the zero position.
First the normal direction measuring sensor is moved downwards to make contact between the ball and the flat sample surface. In the approach procedure, the ball approaches the flat with three decreasing speeds, so that the contact is made without damaging the two materials. The contact is detected when the

measured normal load is at least *50 μN*. After the ball and flat surface are in contact the desired normal load is applied and then the flat sample is moved *100 nm* in lateral direction. Then the sample is moved till *-100 nm* to complete one measurement cycle. After *5 cycles* the sample is moved to the zero position and the next load step is applied and the same routine was repeated for all normal load steps. Typical lateral force–displacement curves for the materials mentioned in Table 6.1 are shown in Figure 6.7. The *5 cycles* for each Si–glass and SiO_2–glass interface are shown with an applied load of *30 mN* when measured in ambient (*20°C, 1 bar and 45±5% RH*) conditions.

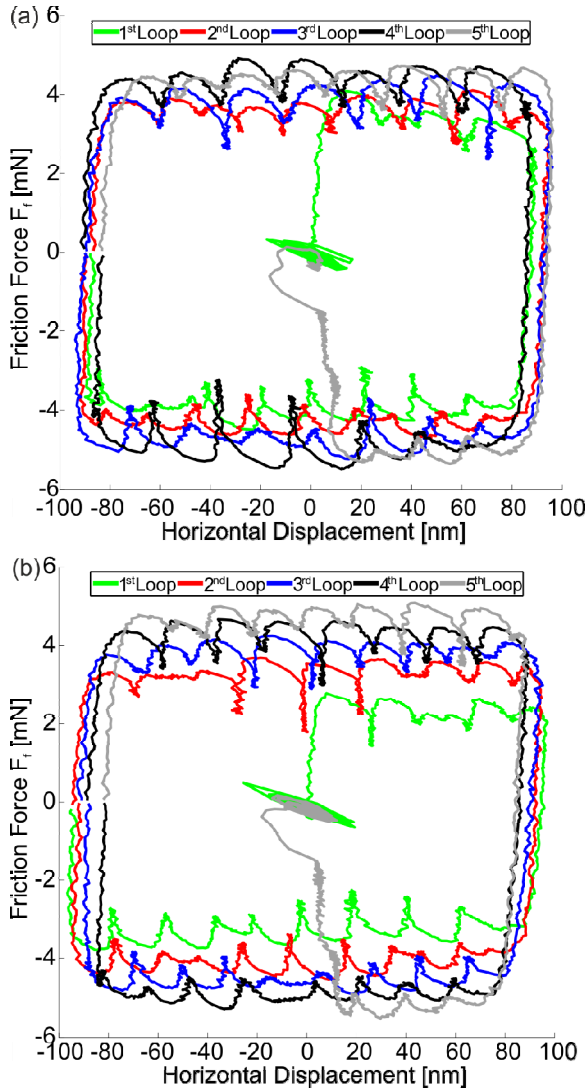

Figure 6.7: Friction force measurement loops measured with (a) Si and (b) SiO_2 ball of 5 mm diameter in contact with float glass flat surface. The measurements were performed by applying 30 mN of normal load in ambient (20°C, 1 bar and 45±5% RH) conditions .

Measurements were also performed on the VAFT for Si-glass interface in ambient as well as in HV conditions to study the static friction behaviour in both environments. The measurements were performed by the friction force measurement procedure explained in section 3.5. Unlike the measurements performed on UNAT, only the first friction force loop was measured and a typical force-displacement curve in tangential direction is shown in Figure 6.8. The measurements shown in Figure 6.8 were performed by applying a normal load of *15 mN*.

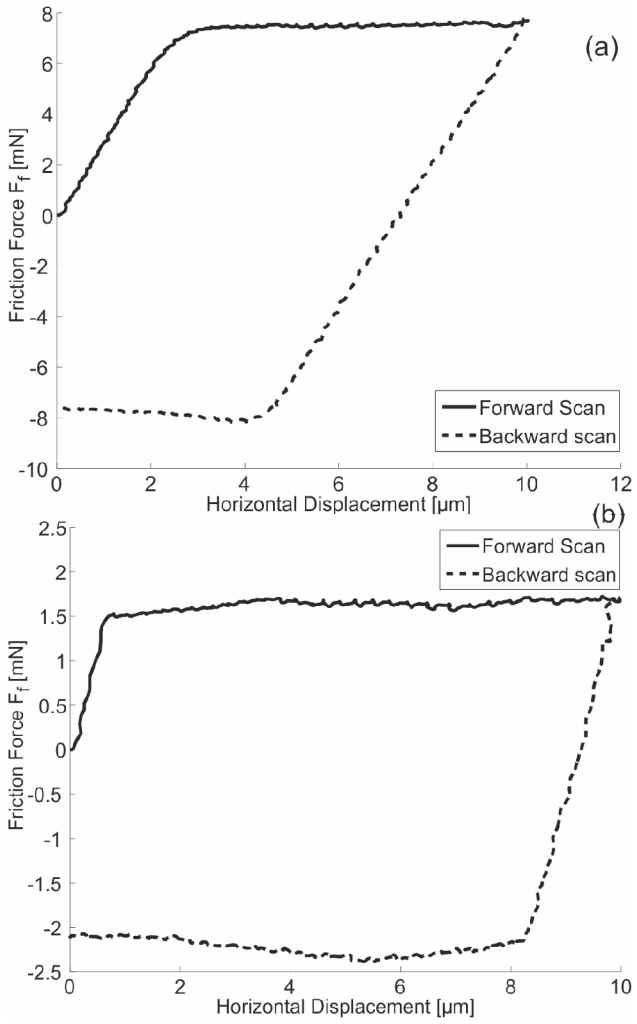

Figure 6.8. A typical force–displacement curve measured with VAFT showing the horizontal displacement and the friction force for Si–glass interface in (a) ambient (20°C, 1 bar and 45±5% RH) and (b) HV (20°C, 10^{-6} mbar) conditions. A normal load of 15 mN was applied for these measurements.

Measurements were performed by changing the normal load from *5 mN* to *25 mN* both in ambient and HV (*20°C, 10^{-6} mbar*) conditions. A significant difference in the static friction force can be seen when the interface is operating in HV conditions. The applied normal load for these particular measurements shown in Figure 6.8 is *15 mN* and the corresponding static friction force is *7.6 mN* and *1.55 mN* in ambient and HV respectively. The results of the static friction force measurements both from UNAT and VAFT will be discussed in the next section. It is important to mention here that the horizontal displacement from both measuring setups is actually an addition of the displacement in the contact (preliminary displacement) and the displacement in the flexible part (e.g. elastic hinges of the VAFT shown in Figure 3.4) of the measurement setup.

6.4 Results and discussion

To verify the model explained in section 6.2 with the system under observation using different material combinations, friction force measurements were performed. The parameters which have been studied with these measurements are the normal load dependency of the static friction force, the coefficient of static friction and the preliminary displacement as explained in section 6.2. Furthermore, the behaviour of the tangential traction as a function of the radial distance has also been studied.

6.4.1 Effect of roughness and shear strength

Si, SiO_2 and Sapphire (Al_2O_3) *5 mm* diameter balls have been used to study the effect of surface roughness on the static friction force. As discussed before, Si and SiO_2 balls are relatively smooth as compared to the Al_2O_3 ball, therefore it is expected that the Al_2O_3 ball will behave differently. Similar measurements were performed for the Al_2O_3-glass interface as shown in Figure 6.7. The first and the second friction loop were compared for all three materials and are shown in Figure 6.9. It can be seen that the static friction force values for Al_2O_3-glass interface are much higher than the Si-glass and SiO_2-glass interface. Therefore, most probably the static friction force increases with an increase in surface roughness and difference in the shear strength of the contacting interface.

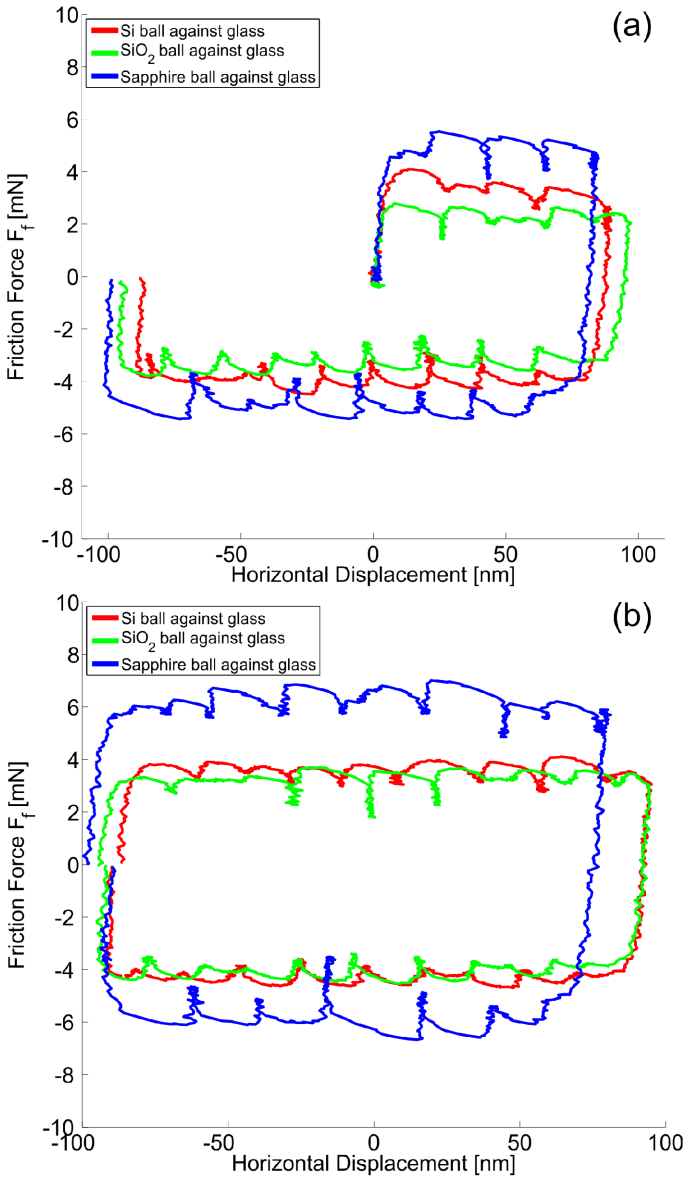

Figure 6.9: (a) First and (b) second friction force loop measured with Si, SiO_2 and Al_2O_3 ball of 5 mm diameter in contact with float glass flat surface in ambient conditions. The measurements were performed by applying 30 mN of normal load.

On the other hand, it can also be seen from Figure 6.9(a) and Figure 6.9(b) that the values of the static friction force for the first loop are slightly different than the second loop. The difference in the values can be due to the presence of contaminant layers between the interface and after the first scan these interfacial layers will be removed. This results in a stable value of the static friction force.

6.4.2 Static friction force

The normal load dependent static friction force for silicon and silica balls against float glass for only the forward scan is shown in Figure 6.10, since the trend of backward scan was similar to the forward scan. The value of the static friction force for both Si and SiO_2 increases with the increase in the normal load. It is also clear from Figure 6.10 that the increase in the friction force is not linear. Therefore, power law curve fits to the measurements have been plotted and it can be seen that the static friction force follows the power law of $F_N^{0.7}$. Using Eq. (6.2) and Eq. (6.3) the relation between friction force and the normal load considering the constant shear stress is $F_t \propto F_N^{2/3}$, therefore the powers used to fit the experimental data are similar to the power law derived from the theory.

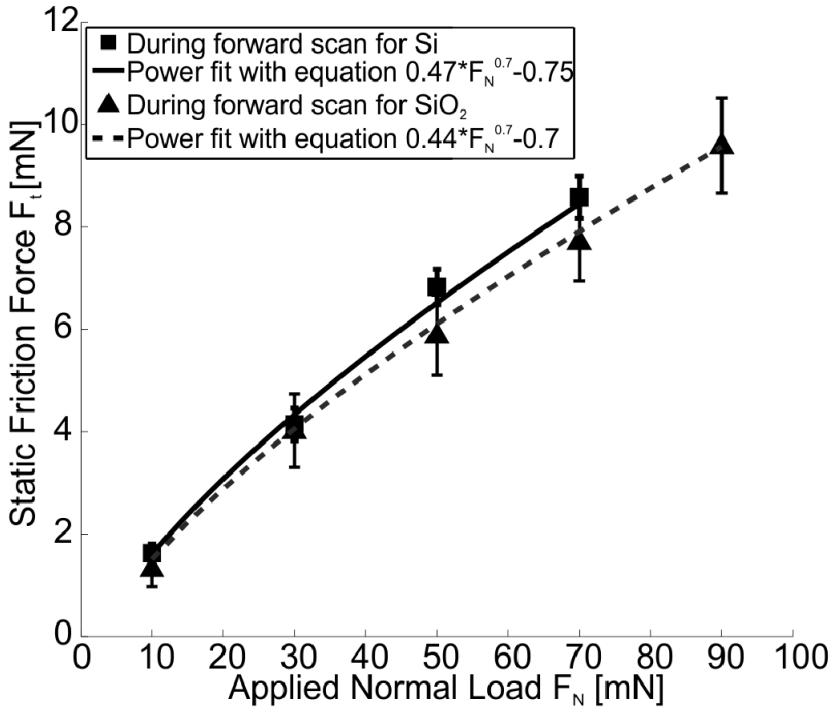

Figure 6.10: Measured static friction force F_t as a function of applied normal load for Si and SiO_2 ball measured in ambient conditions. The power law curve fits are also shown along with the governing equation.

The error bars are showing one standard deviation of the four friction measurements at each normal load instance. The first friction cycle has not been considered in this data since the values obtained from the first cycle is often lower than the other four cycles, as can be seen from Figure 6.7(b). The possible reason for this low value of the friction force in the first cycle is the

presence of contaminants on the surfaces. It can also be seen that the values of the friction force are almost similar for both Si and SiO_2. The reason for this can be explained by the oxidation on the Si ball, meaning that the interface has an interfacial layer of SiO_2. The friction force is not a bulk property but an interfacial property, therefore, the interface plays an important role in determining the frictional behaviour between two materials. As mentioned before Eq. (6.3) is valid for a single asperity contact, therefore, the relation between F_t and F_N is also valid for the single asperity contact. From the experimental results shown in Figure 6.10 it can be clearly seen that the measurements have been performed with a single asperity contact, since $F_t \propto F_N^{2/3}$. It is known that for rough surfaces the contact area follows $A \propto F_N$ [31], meaning that a linear relationship is expected between the static friction force versus the normal load [77].

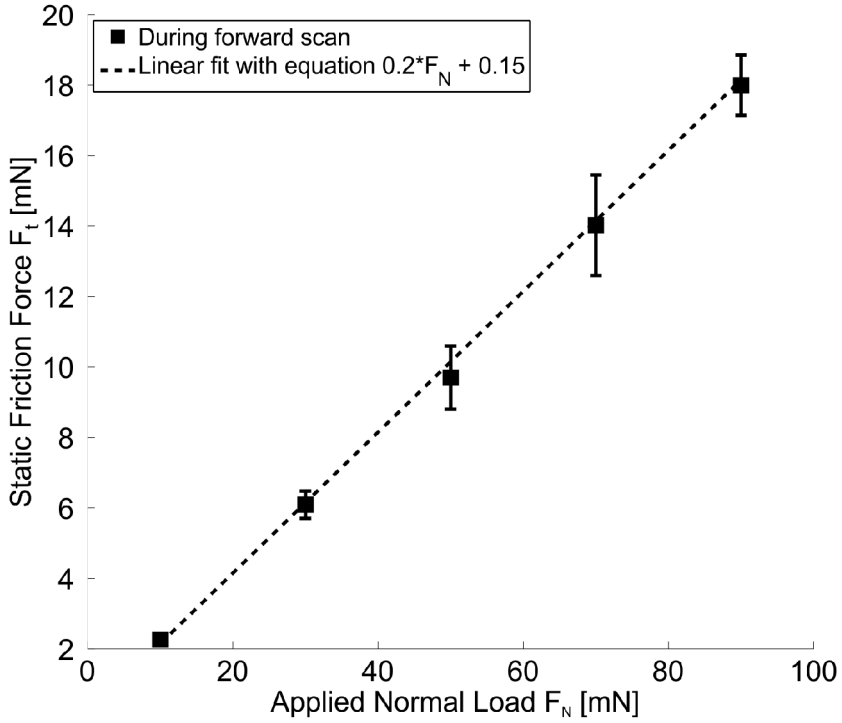

Figure 6.11: Measured static friction force as a function of applied normal load in ambient conditions for a Sapphire ball against a glass flat surface.

The friction force as a function of applied normal load for a relatively rough Sapphire (Al_2O_3) ball and a smooth flat glass surface has also been studied. Similar experiments were performed by changing the normal load and performing 5 friction loops at each normal load step. The measurements were analysed in the same way as they were analysed for Si and SiO_2 balls by not considering the first friction loop. The results shown in Figure 6.11 demonstrate

a linear relationship between the static friction force and the applied normal load, since, it was shown in Table 6.1 that the Al_2O_3 ball is relatively rough compared to the Si and SiO_2 balls. This supports the theoretical relationship for rough surface i.e. $A \propto F_N \Rightarrow F_t \propto F_N$.
Similarly, the COSF was calculated from the static friction force measurements for Si and SiO_2 balls as a function of the applied normal load and is plotted in Figure 6.12. First, we can see that the COSF decreases with the increase in the normal load. At low values of the normal load the COSF decreases more rapidly than at higher values of the normal load where it reaches a stable value. Secondly, the power law shown in Eq. (6.4) has been used to fit the measured data. The power law curve fits, along with the governing equations, are also shown in Figure 6.12 and it can be seen that the power law fits fairly well to the measured data. The offsets in the governing equations, both in Figure 6.10 and Figure 6.12, can be explained by the presence of the adhesion force between the contacting surfaces. Therefore, it can be concluded that the applied normal load F_N also contains the contribution of adhesion force. It is known that for smooth surfaces in a humid environment the adhesion force is mainly determined by the capillary force and plays a very important role in contact mechanics [6, 9].

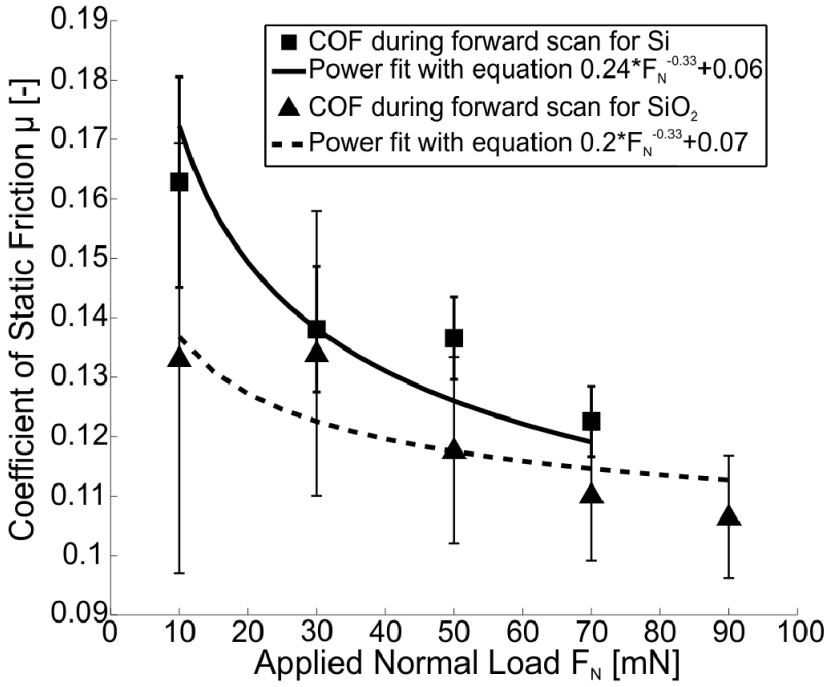

Figure 6.12: Coefficient of static friction force μ as a function of applied normal load for Si and SiO_2 ball. The power fits are also shown along with the governing equation.

To study the effect of the environment, static friction force measurements were performed on VAFT in ambient as well as in HV conditions. The coefficient of

static friction as a function of applied normal load is shown in Figure 6.13 when the measurements are performed in ambient and HV conditions. The values of the COSF reduce when the Si-glass interface is operated in HV conditions. The reason for this reduction is due to the reduction of adhesion force by means of the capillary force in HV conditions as was explained in Chapter 5. It can be seen that the COSF follows the *-1/3* power law for both measurements. However, the magnitude of COSF in ambient conditions measured with VAFT is different when compared with the COSF values measured with UNAT shown in Figure 6.12. The reason for this difference might be due to the difference in preparation of samples.

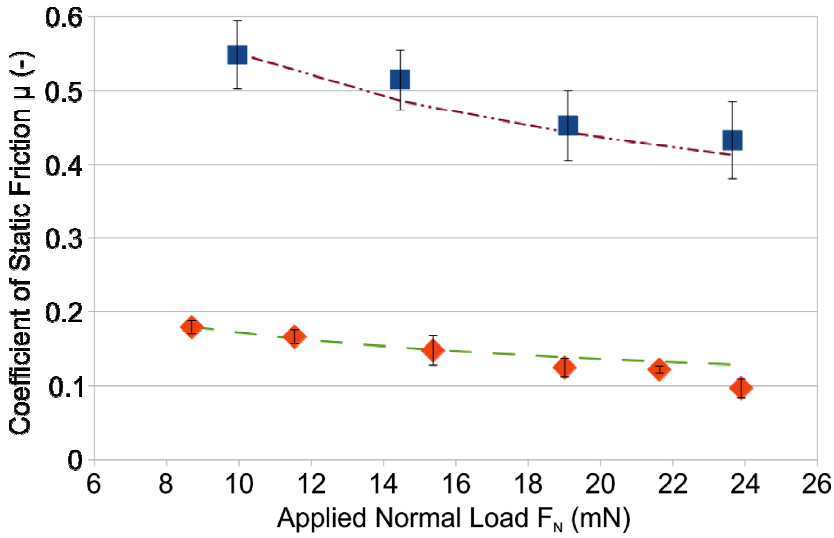

Figure 6.13: Coefficient of static friction force μ as a function of applied normal load for Si ball against glass flat surface measured with VAFT in ambient (■) and HV (◆) conditions.

6.4.3 Preliminary displacement

The friction force measurements were also used to measure the preliminary displacement δ_{tmax}, the tangential displacement in the contact just before sliding. The results for Si and SiO_2 balls against a glass flat surface are shown in Figure 6.14. From Eq. (6.5) it can be seen that the preliminary displacement is dependent on the applied normal load to the power of *1/3*. The power law curve fits on the measured data are also shown along with the governing equations. It can be seen that the displacement is increasing with the increase in the normal load and for Si and for SiO_2 as it follows the power of *0.33*. It is important to mention here that the preliminary displacement measured is in nanometres and the error bars show one standard deviation in the measured data.

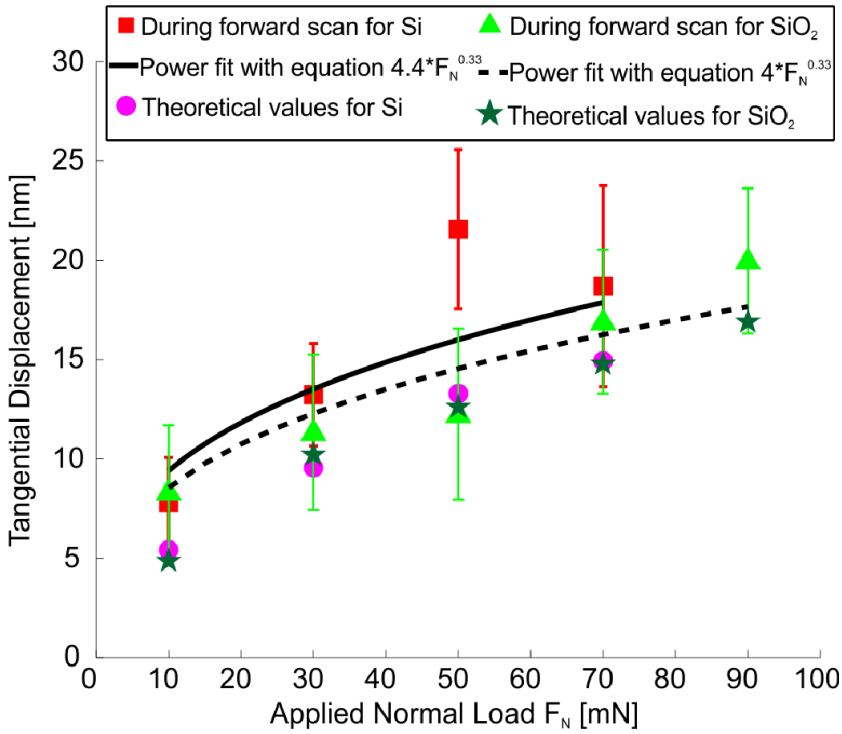

Figure 6.14: Measured tangential displacement and calculated maximum preliminary displacement δ_{tmax} as a function of applied normal load for Si and SiO_2 ball against glass. The power fits are also shown along with the governing equation. Theoretical values calculated using the measured data are also shown for both materials.

The theoretical values of the preliminary displacement at the point of slip for Si and SiO_2 are also shown in Figure 6.14. These values have been calculated using Eq. (6.1) and the measured friction force and COSF data mentioned in section 6.4.2 for all the measurement cycles except the first cycle. The theoretical values shown in Figure 6.14 are the average of four measurements at each normal load. Since the theoretical values are calculated without the first measurement cycle, therefore Eq. (6.1) only calculates a part of the displacement (i.e. from point *G* to point *A* in Figure 6.2). To calculate the displacement from point *D* to *A* in Figure 6.2 the expression is given as [15]:

$$\delta_t = -\frac{3 \cdot \mu \cdot F_N}{16 \cdot a \cdot G^*}\left[2 \cdot \left(1 - \frac{\mu \cdot F_N - F_f}{2 \cdot \mu \cdot F_N}\right)^{2/3} - 1\right] \tag{6.8}$$

It can be seen from Eq. (6.8) that when F_f is equal to zero then the value of δ_t is *26%* of the maximum preliminary displacement δ_{tmax}. Therefore to calculate the complete displacement δ_{tc} (i.e. from point *E* to point *A* in Figure 6.2) the expression is:

$$\delta_{tc} = \delta_t + 0.26 \cdot \delta_{tmax} \tag{6.9}$$

The theoretical values indicate a trend similar to the experimental results. However, the theoretical values of the preliminary displacement are somewhat less than the measured values. The difference in the measured and theoretical values can be explained by realizing that the measured values are the sum of the displacement in the contact and the displacement in the lateral direction measuring sensor of the UNAT. The calibrated lateral stiffness of the UNAT is *334 mN/μm*, which is in the same order as the lateral contact stiffness for the interfaces being studied. Using Eq. (6.6) the lateral contact stiffness for Si-glass interface was calculated to be 767 mN/μm when the applied normal load is 10 mN. It is important to mention here that the lateral stiffness calculated from Eq. (6.6) is the maximum lateral stiffness when there is no applied tangential load. Therefore, theoretically as the tangential load is increased the lateral stiffness decreases and at the point of full slip the lateral stiffness goes to zero. It can be concluded that the difference in the measured and the theoretical values of the preliminary displacement is indeed reasonable because some part of the measured displacement is due to the deformation of the lateral direction measuring head of UNAT and the rest is due to the deformation of the contact.

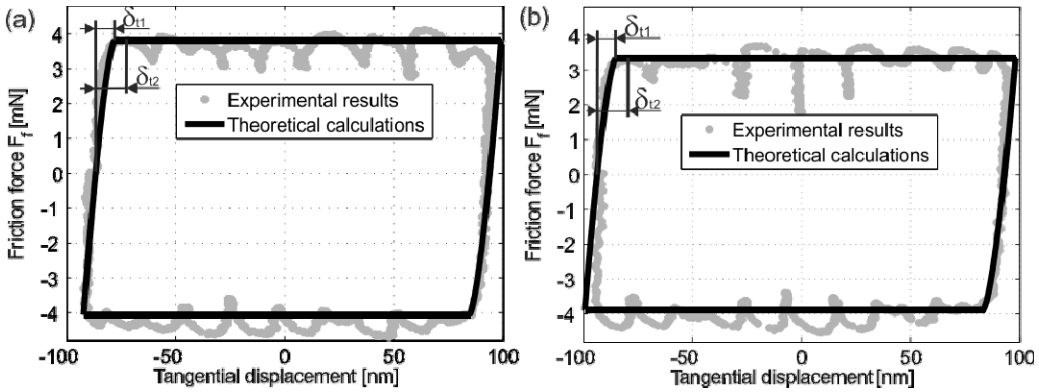

Figure 6.15: Comparison of experimental results of tangential force-displacement curve with the theoretical calculations for (a) Si and (b) SiO_2 balls when 30 mN of normal load is applied. Maximum preliminary displacement calculated δ_{t1} and measured δ_{t2} are also shown.

A comparative example of a measured and a calculated friction force cycle is shown in Figure 6.15. For simplicity only, one cycle is shown both for Si and SiO_2 when the applied normal load is 30 mN. The linear part of the theoretical curve has been calculated using Mindlin's theory and using Eq. (6.9). The horizontal asymptote is drawn to show the maximum tangential force at the time of slip. It can be seen from Figure 6.15 that for both Si and SiO_2 the values of maximum preliminary displacement calculated δ_{t1} and measured δ_{t2} are very close to each other. It can also be seen that the theoretical values are somewhat

less than the measured values and the reason has been explained above. In general, it can be concluded that the Mindlin's theory explains the pre-sliding behaviour of a single asperity contact very well when the contact pressure is kept below 100 MPa.

6.4.4 Tangential traction

In Figure 6.16 the limiting shear stress in the contact required to attain the full slip condition for the Si and SiO_2 balls is shown for different applied normal loads. This maximum tangential traction was calculated using Eq. (6.7) by putting the measured values of the static friction force and the calculated values of the contact radius *a*. The data is represented as it has been shown in Figure 6.6. It can be seen that the increase in the tangential traction with the increase in the normal load is not linear. It was discussed earlier that Mindlin's theory is based on non-adhesive contact and the shear stress is independent of normal load. However, the measurement results show that the shear stress is not independent of normal load. This can be explained by the presence of adhesion between a ball and a flat. The presence of adhesion will change the normal load dependence power law for the contact area and the coefficient of friction. This change can also be seen in the shear stress calculations since the shear stress is dependent on contact area and the coefficient of friction as shown in Eq (6.7). We can also see from Figure 6.16(a) that at higher loads the shear stress is becoming constant which explains the fact that the contribution due to the adhesion force is almost negligible. Moreover, in Figure 6.16(b) it can be seen that the shear stress is also becoming constant at higher loads. Similarly, the increase of normal load also increases the radial distance. In Figure 6.16 the radius of the stick zone *s* approaches to zero and the radial distance shown is only *a* as shown in Figure 6.5.

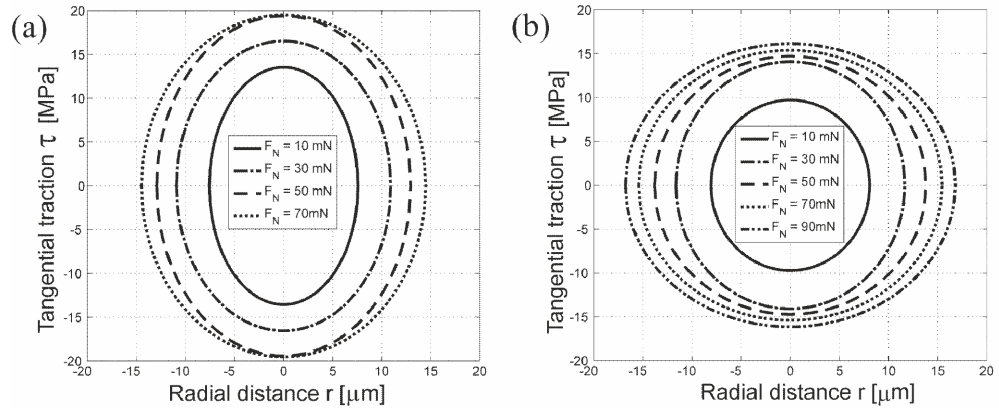

Figure 6.16: The tangential traction as a function of applied normal load for (a) Si and (b) SiO_2 ball against a flat glass surface.

6.5 Summary

The pre-sliding and static friction force behaviour for Si, SiO_2 and Al_2O_3 ball against glass flat surface were discussed. Mindlin's theory was briefly explained and the measurement results were studied using this theory. The measurement results show that the static friction force, coefficient of static friction and the preliminary displacement is dependent on the applied normal load and follows the described theoretical trends. The static friction force measurements were also performed with VAFT using Si-glass interface in ambient and HV conditions. The results show that the COSF as a function of applied normal load also follows the described theoretical trend. The COSF reduces when the same interface is operated in HV conditions.
Furthermore, it has been shown that Mindlin's theory to calculate the preliminary displacement holds for the contact pressures of the order of 100 MPa or less. However, it can be seen from the experimental results that for low applied normal loads, the adhesion forces play an important role. The tangential traction during the oscillating tangential load has also been discussed. Using Mindlin's theory, the changes in the tangential traction and the stick-slip area can be studied. It has also been shown that at low loads the shear stress is dependent on the normal load whereas at higher loads it becomes constant. This effect is also an indication of the presence of adhesion at low loads.

Chapter 7
RELATION BETWEEN ADHESION AND STATIC FRICTION[1]

7.1 Introduction

Chapter 4, Chapter 5 and Chapter 6 gave an explanation and analysis of the adhesion and static friction behaviour of a single asperity contact. No direct or indirect relationship between adhesion and friction can be formulated from this analysis. It has been seen that if the adhesion force is reduced because of a change in the environment (RH, for example), a reduction in the static friction force is also measured. However, if the adhesion force is reduced due to an increase in surface roughness of the interface, the friction force seems to increase for that particular interface. Likewise, the correlation between contact models and experiments is unclear as well. This is why this chapter deals with the relation between adhesion and static friction.

Here, an approach will be presented to completely analyse a single smooth adhesive contact operating in ambient and HV conditions by combining a theoretical analysis, pull-off experiments and friction experiments performed at different applied normal loads. Using this approach, the adhesive contact can be analysed to a fuller extent. For example, not only can the relevant adhesive regime be predicted, but it can also be validated using pull-off experiments in combination with sliding experiments conducted on different loads. Combining the models with the measured adhesion and friction force data will enable to determine the work of adhesion and the shear stress present between the Si–glass interface. When comparing HV conditions with ambient conditions, it was found that the adhesion as well as the friction force is significantly lower under high vacuum conditions for the Si–glass interface. When comparing modelling results with experiments, it can be concluded that the trends from the theoretical predictions are in good agreement with the measurements, both for the HV and ambient regime.

In section 7.2 the contact mechanics models will be discussed along with the results from a modified M-D model incorporating capillary forces.

[1]Reproduced from: M.A. Yaqoob, M.B. de Rooij and D.J. Schipper, Relating friction and adhesion for single smooth contact by means of models and experiments, Submitted to: *Tribology International*, 2012.

Experimental procedures and sample preparation is explained in section 0. In section 7.4 the results are presented and are discussed in detail.

7.2 Contact mechanics models

A ball on a flat configuration, as shown in Figure 7.1, can be used to perform adhesion and friction force measurements for a single asperity contact by pull-off and sliding experiments, respectively. Depending on the magnitude of the adhesive forces compared to the applied load and to the elastic properties of the materials in contact, the contact situation can be described with several contact models, like JKR, DMT, M-D and Hertz.

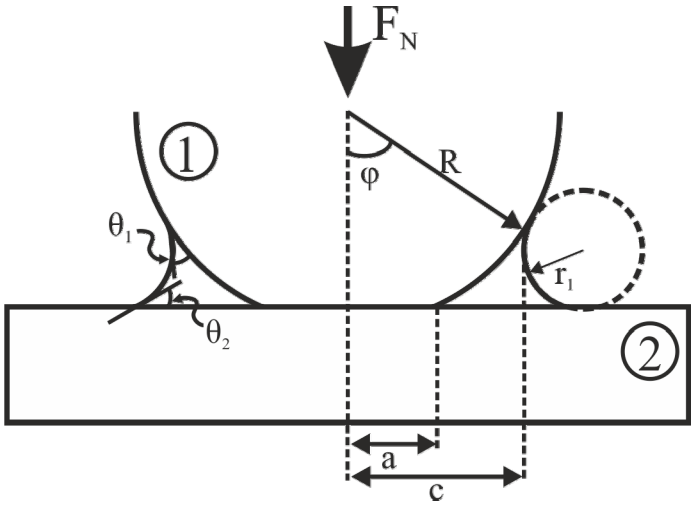

Figure 7.1. A sphere in contact with a flat surface under a certain applied normal load F_N in humid environment. The solid–solid contact radius *a* and the meniscus radius *c* are also shown.

As explained before, the Hertzian model does not consider adhesion in or outside the contact area [7, 18] and assumes that there are no adhesion forces acting in the contact. Typically, at high normal loads the behaviour according to Hertz has been shown to fit the experiments because the adhesion forces are relatively low as compared to the applied load under these conditions. However, the Hertz model fails to predict the area of contact at very low or zero normal load due to the significance of surface forces. Adhesive interactions between the surfaces were taken into consideration when Johnson, Kendall and Roberts (JKR) proposed their model [29]. The JKR model describes the effect of strong short–range interactions between materials with relatively low elastic modulus and large radius of curvature [18, 34]. This model shows that there is a finite contact area between the surfaces under zero normal load and also predicts that there is an external force required to separate two bodies with given surface energies and geometry [29, 30]. The JKR model assumes that the adhesive

interaction is inside the contact zone. Another model including adhesive interactions was proposed by Derjaguin, Muller and Toporov (DMT). In this model, it was assumed that adhesive interactions are present outside the contact area.

A dimensionless parameter μ_T, called the Tabor parameter representing the ratio between the gap outside the contact zone and the equilibrium distance between atoms has been presented in [36]. In mechanical terms, this parameter represents the ratio of the magnitude of the elastic deformation to the range of adhesive forces. This parameter established the range of applicability of the two models and suggested that the JKR and DMT models are at the limits of μ_T.

A solution to the contact problem with interactions inside and outside the contact zone was provided by Maugis [37]. The Dugdale approximation (constant adhesive stress outside the contact zone) has been used in this model and is known as Maugis–Dugdale (M–D) model. The M–D model showed the transition of a contact problem from DMT to JKR as two opposite ends of a continuous spectrum based on a parameter λ (the Maugis parameter), which is equivalent to the Tabor parameter $(\lambda = 1.16\mu_T)$. An adhesion map has been reported by Johnson and Greenwood [34, 38] based on the Maugis model as shown in Figure 2.7. If $\lambda > 5$, the JKR analysis becomes appropriate and when $\lambda < 0.1$, the DMT model is applicable. In the intermediate range $0.1 > \lambda > 5$ the M-D model has to be applied.

Further, a modified M–D model incorporating the meniscus forces has been developed in [39] which was briefly discussed in section 2.3.3. This modification of the model is required since the JKR, DMT and M–D models are assuming solid–solid adhesive contacts where van der Waals forces are dominant. However, if two hydrophilic surfaces are brought into contact with each other under humid environment the meniscus forces will dominate the adhesive interaction [1, 7]. The M–D model has been modified using the Kelvin and Young–Laplace equation and has been used to calculate the contact areas for dry as well as humid contact conditions. However, the validity of the Kelvin equation is questionable at low RH as discussed in section 4.2. Therefore, the modified M–D model cannot be used in relatively dry situations, (e.g. in HV conditions) as it was discussed in [39, 78].

The adhesion force or pull–off force can be calculated using JKR, DMT or M–D model using the following general relation for the pull-off force for a sphere-on-flat contact [39, 78]:

$$F_a = -n\pi W_{12} R \tag{7.1}$$

In this equation, n has a value between $1.5–2$, W_{12} is the work of adhesion between two surfaces and R is the radius of the spherical surface. If the JKR theory is applicable, then $n = 1.5$, if the DMT theory is applicable, then $n = 2$.

In cases where the M–D theory is applicable an intermediate value of n should be used.

For a single smooth contact, (a smooth sphere in contact with a smooth flat surface as shown in Figure 7.1) the contact area can be calculated using the JKR, DMT or M–D models depending on which one describes the actual adhesive conditions. Using Eq. (7.2) one can calculate the contact area using JKR model and using Eq. (7.3) one can calculate the contact area using DMT model.

$$A_{(JKR)} = \pi\left(\frac{3R}{4E^*}\right)^{2/3}\left(F_N + 3\pi W_{12}R + \sqrt{6\pi W_{12}RF_N + (3\pi W_{12}R)^2}\right)^{2/3} \tag{7.2}$$

$$A_{(DMT)} = \pi\left(\frac{3R}{4E^*}\right)^{2/3}\left(F_N + 2\pi W_{12}R\right)^{2/3} \tag{7.3}$$

The M–D equations are more difficult to utilize, since Maugis' formulation lacks a single expression relating only a and F_N. Eq. (7.4) to (7.7) are needed to solve the M–D model [37]:

$$\frac{\lambda\bar{a}^2}{2}\left\{\left(m^2-2\right)\sec^{-1}m + \sqrt{m^2-1}\right\} + \frac{4\lambda^2\bar{a}}{3}\left\{\sqrt{m^2-1}\sec^{-1}m - m + 1\right\} = 1 \tag{7.4}$$

$$\bar{P} = \bar{a}^3 - \lambda\bar{a}^2\left\{\sqrt{m^2-1} + m^2\sec^{-1}m\right\} \tag{7.5}$$

$$\bar{\delta} = \bar{a}^2 - \frac{4}{3}\lambda\bar{a}\left\{\sqrt{m^2-1}\right\} \tag{7.6}$$

Where;

$$\bar{a} \equiv a\left(\frac{4E^*}{3\pi W_{12}R^2}\right)^{1/3};\quad \bar{c} \equiv c\left(\frac{4E^*}{3\pi W_{12}R^2}\right)^{1/3};\quad m = c/a;\quad \bar{P} \equiv \frac{F_N}{\pi W_{12}R};\quad \bar{\delta} \equiv \delta\left(\frac{16E^{*2}}{9\pi^2 W_{12}^2 R}\right)^{1/3}$$

$$\lambda \equiv \sigma_o\left(\frac{9R}{2\pi W_{12}E^{*2}}\right)^{1/3} \tag{7.7}$$

In these equations, a and c are the radii of contact and adhesive zones respectively as shown in Figure 7.1. E^* is the reduced modulus of elasticity of

two materials and R is the radius of the sphere. F_N is the total load and W_{12} and δ are the work of adhesion and deformation respectively. Also, λ and σ_o are the Maugis (elasticity) parameter and constant adhesive stress outside the contact respectively. If $\sigma_o = 1.03W_{12}/z_0$ is assumed then $\lambda=1.16\mu_T$, this corresponds to the same work of adhesion as in the Lennard-Jones potential. Numerical methods are required to solve the M–D model, therefore, by knowing the values of λ and F_N and solving Eq. (7.4) and (7.5) one can find the solutions for a and c. Efforts have been made to generate a simplified equation to fit the contact area and the normal load [79, 80]. In [79] a simplified equation to calculate the normal load dependent contact area has been reported. The equation also uses the JKR and DMT models as the limiting cases of the equation, and the intermediate values can be used to calculate the contact area for M–D model.
A modification of Eq. (7.7) is required to incorporate the capillary forces as explained in section 2.3.3, using the Young-Laplace and Kelvin equations [39]. The resulting modified Maugis parameter λ_{cap} is given as:

$$\lambda_{cap} = \left(\frac{9R\gamma_L^2}{4\pi E^{*^2} r_k^3} \right)^{1/3} \tag{7.8}$$

$$\lambda_{cap} = \left(-\frac{9RR_g^3T^3\left[\log\left(p/p_s\right)\right]^3}{4\pi E^{*^2} V_m^3 \gamma_L} \right)^{1/3} \tag{7.9}$$

Where, V_m is the molar volume, R_g is the gas constant, T is the absolute temperature, γ_L is the surface tension of the liquid (water), r_k is the mean radius of the meniscus or Kelvin radius and p/p_s is the relative humidity (RH). As explained above, the M–D model used the Dugdale approximation of constant adhesive stress outside the contact. Therefore, use of Young-Laplace equation is valid since it considers a constant capillary or Laplace pressure inside the meniscus.
The results of the calculated dimensionless $\bar{a}$ and dimensionless $\bar{c}$ as a function of the dimensionless load $\bar{P}$ for different RH are shown in Figure 7.2(a) and Figure 7.2(b) respectively. These values have been calculated for a *5 mm* silicon ball in contact with a flat glass surface. The corresponding λ values for different RH are also shown. It can be seen from Figure 7.2(a) that as the RH increases the value of the solid–solid contact radius a is decreasing. However, the value of the adhesive radius increases with an increase in RH as shown in Figure 7.2(b). This trend in a and c is because of the increase in the

amount of water with an increase in the RH around the contact. As the amount of water increases it will tend to condensate around the contact forming a meniscus and the meniscus will grow with the increase in the RH. It can also be seen that the value of solid–solid contact radius *a* and the value of adhesive radius *c* is approaching each other when the RH is 5%. This, indeed, indicates that under these conditions there is no adhesive zone around the contact due to meniscus and all the adhesion force is contributed by the solid–solid contact.

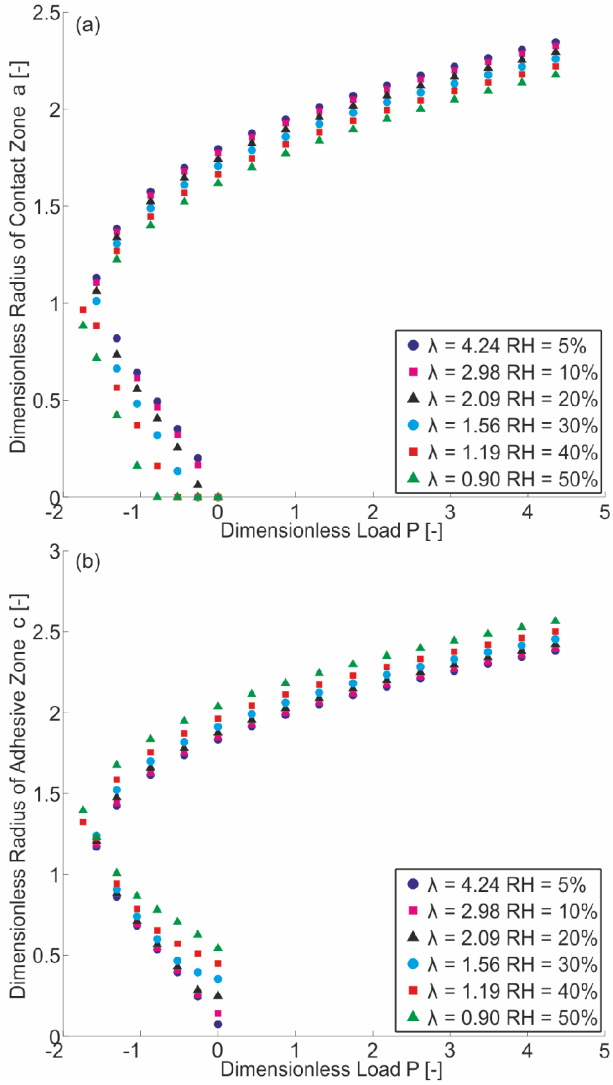

Figure 7.2. (a) Dimensionless radius of the solid–solid contact and (b) the dimensionless radius of the adhesive zone as a function of dimensionless load for different values of RH. The corresponding λ values for different RH are also shown.

The value of λ also decreases with the increase in the RH. Using the adhesion map reported in [34, 38] and the values of λ the appropriate contact mechanics model can be selected. In Figure 7.3 the adhesion map was shown with the marked span of the λ values for *1–90% RH* for a *5 mm* diameter silicon ball and a flat glass surface. This shows that for a dry contact, such as in HV conditions, the JKR model can be used to calculate the contact area. However, as the RH increases, the JKR model cannot be used and the appropriate choice to calculate the adhesion force and contact radius will be the M–D model. It is important to mention here that the λ values for different material combinations change the operational regime depicted in the adhesion map. Similarly, the λ value is also dependent on the radius of the ball in contact with a flat and will also affect the choice of the contact model. The material parameters and the geometry also influence the choice of the appropriate contact model. However, the basic procedure for predicting which contact model to use remains the same. It can also be seen from Figure 7.3 that the JKR, DMT and M-D models are applicable for low values of the applied normal load and for higher loads the Hertz model is applicable.

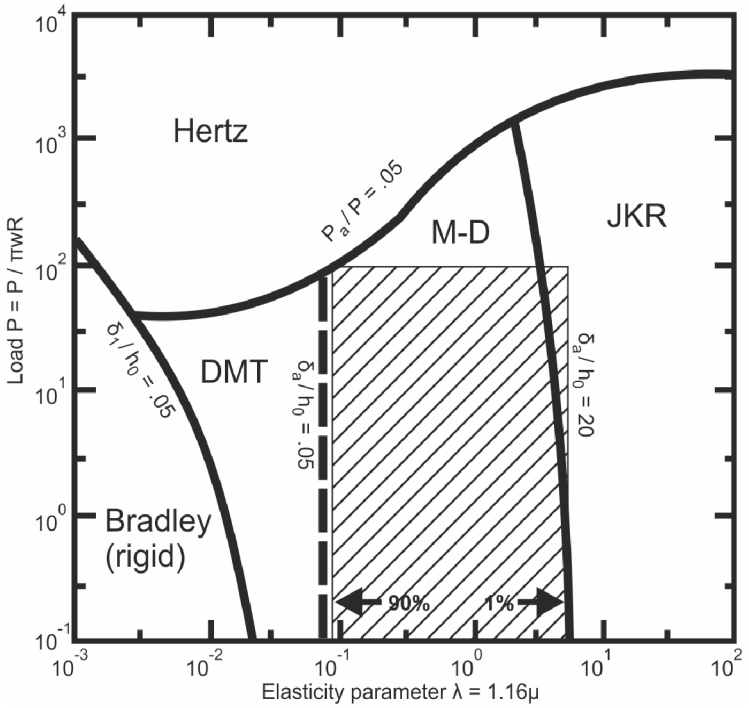

Figure 7.3. An adhesion map reproduced from [34, 38] showing the span of λ values for a 5 mm silicon ball against a flat glass surface from 1–90% of RH. P_a is the adhesive force, δ_a is the adhesive compression, δ_1 is the elastic compression and h_0 is the separation distance where adhesion force is acting.

7.3 Adhesion and static friction experiments

Adhesion and static friction experiments at different loads were performed in ambient (*20°C, 1 bar and 45±5% RH*) as well as in HV (*20°C, 10^{-6} mbar*) conditions to study the relationship between adhesion and friction force. Adhesion and friction measurements were performed on the VAFT by the measurement procedure explained in section 3.5.The appropriate adhesion regime and the contact model determined by M–D analysis can be verified using these experiments.

7.3.1 Sample preparation

Since this study focuses on the single smooth contacts, it is required to reduce the roughness effects as much as possible, like the effect of mechanical interlocking. Samples used to perform the adhesion and friction measurements were, a smooth silicon ball of *5 mm* in diameter with an RMS surface roughness of 2–3 nm and a flat float glass surface with an RMS roughness of *0.7-1 nm*. The flat glass surface was cleaned in an ultrasonic bath of acetone for 15 minutes and then dried and placed on the XY stage. The silicon ball was first cleaned in an ultrasonic bath of acetone for 15 minutes and was then mounted on an indenter, which had been mounted on a cantilever, as shown in Figure 3.2(a). The ball was checked under a Keyence Confocal Microscope to find a clean and smooth spot before the glue was applied. Once a good spot was identified, the ball was very carefully glued so no glue was present in or around the contact area. The ball was again inspected under the microscope to see the presence of any contamination due to glue. The measurements were performed after the assurance of a smooth clean spot.

7.3.2 Experimental procedure

The pull–off measurements were performed in ambient conditions. From these experiments, the adhesion force between the silicon–glass interface is obtained. The average value of five pull-off measurements was used to calculate the work of adhesion using the appropriate contact model. The static friction measurements were performed when the ball was in contact with the flat surface. The normal force is increased by a small force step, that is a fractional part of the final desired normal load, which is set to *25 mN*. After every force step a friction experiment was performed and the static friction force was measured. Each friction experiment consists of one forward and backward scan cycle. The scan speed was kept constant to *100 nm/sec* and the scan length was *10 μm*. These measurements were performed until the final desired load (*25*

mN) was applied and the static friction force for all the force steps were measured.
Similar experiments were performed when the setup was operating in HV conditions. The RH inside the vacuum chamber was reduced to a level of *1–2%* or below because the partial pressure of water determines the total pressure in the chamber, which has been measured with a humidity sensor and the mass spectrometer, see Appendix D. In ambient conditions, the humidity was controlled by flowing liquid Nitrogen through a closed loop coil placed inside the vacuum chamber. The change in the RH influences the adhesion and well as friction force measurements.

7.4 Results and discussion

A typical force–displacement curve in normal direction in ambient as well as in vacuum is shown in Figure 5.2. The measurement shows the normal displacement of the Z–axis stage and the measured applied normal load. In both measurements the applied normal load is *10 mN* and the resulting pull–off force is *1.05 mN* in ambient and *0.39 mN* in high vacuum conditions as shown in the insets of Figure 5.2. Therefore, it is evident from these measurements that the pull–off force changes significantly if the environmental conditions are changed. As mentioned before, a sequence of five such measurements was performed each in ambient and vacuum to get an average value of pull–off force. The average value of the pull–off force was used to calculate the work of adhesion assuming both JKR and DMT behaviour. The values of the work of adhesion for both models are considered as limiting cases. First, Eq. (7.1) is used to calculate the work of adhesion W_{12} of the surfaces in contact in ambient as well as in HV conditions.
Once the W_{12} is known the contact areas according to the JKR and DMT theories were calculated using Eq. (7.2) and Eq. (7.3) respectively. When comparing HV with ambient, the calculated contact areas based on the measured adhesion force as a function of applied normal load are shown in Figure 7.4. It can be seen that the contact area is decreased when the system operates in HV conditions as compared with the area in ambient conditions. This can also be seen in Figure 7.2(b) where the radius of the adhesive zone c is decreasing as the RH is decreased. As discussed before, the JKR and DMT models are the limiting cases of the M–D model, and the actual contact area based on the M–D model lies between the area of solid (JKR) and dashed (DMT) lines in Figure 7.4. At this stage the exact behaviour of the contact area is still unknown.

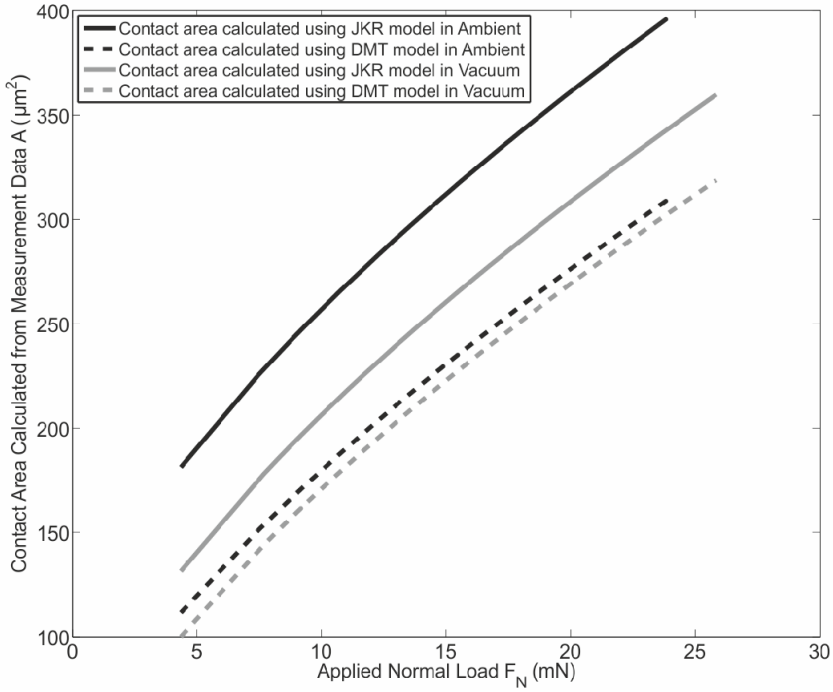

Figure 7.4. The calculated contact area based on adhesion force measurements data for the Si–glass interface. The JKR and DMT areas for both ambient and HV conditions are shown.

After calculating the contact area using both limiting adhesive models, the interfacial shear strength of the surfaces in contact can be calculated. From the friction force measurements the shear stress was calculated using the measured static friction force F_f for a single asperity contact and the following relation:

$$F_f = \tau \cdot A \tag{7.10}$$

Where, A is the contact area calculated for the JKR and DMT models obtained from pull-off measurements and τ is the interfacial shear strength to be determined. The average value of the shear stress was calculated for the JKR and DMT models for ambient as well as in HV condition and will be called τ_{JKR} and τ_{DMT}, respectively.

Carpick, Ogletree and Salmeron (COS) [79] provided an approximate general equation for easily describing the contact area from the M-D model. The general equation can be used for curve fitting and provides a method of determining the value of the transition parameter describing the range of surface forces. They showed that the Maugis' formulation could be approximated using the following formula to determine the contact radius:

$$a = a_{0(\alpha)}\left(\frac{\alpha + \sqrt{1 + F_N / F_a}}{1+\alpha}\right)^{2/3} \quad \because a_{0(\alpha)} = \left[\frac{3\pi W_{12}R^2 + 6\pi W_{12}\alpha R^2}{2E^*}\right]^{1/3} \tag{7.11}$$

Where, α is the transition parameter, a_0 is the contact area at zero load and F_a is the measured pull–off force. Note that $\alpha = 1$ corresponds exactly to the JKR case, and $\alpha = 0$ corresponds exactly to the DMT case. Included in Eq. 7.11 is the fact that F_a and a_0 depend on α as well. Eq. 7.11 is referred to as the generalized transition equation or COS equation. For intermediate cases ($0 < \alpha < 1$), the generalized transition equation corresponds very closely to the Maugis' solution for the transition regime ($0.1 < \lambda < 5$) which is indicated in Figure 7.3. The actual contact radius has been calculated using Eq. 7.11 by putting the values of measured average F_a, W_{12} values and using the transition parameter α as a fitting parameter.

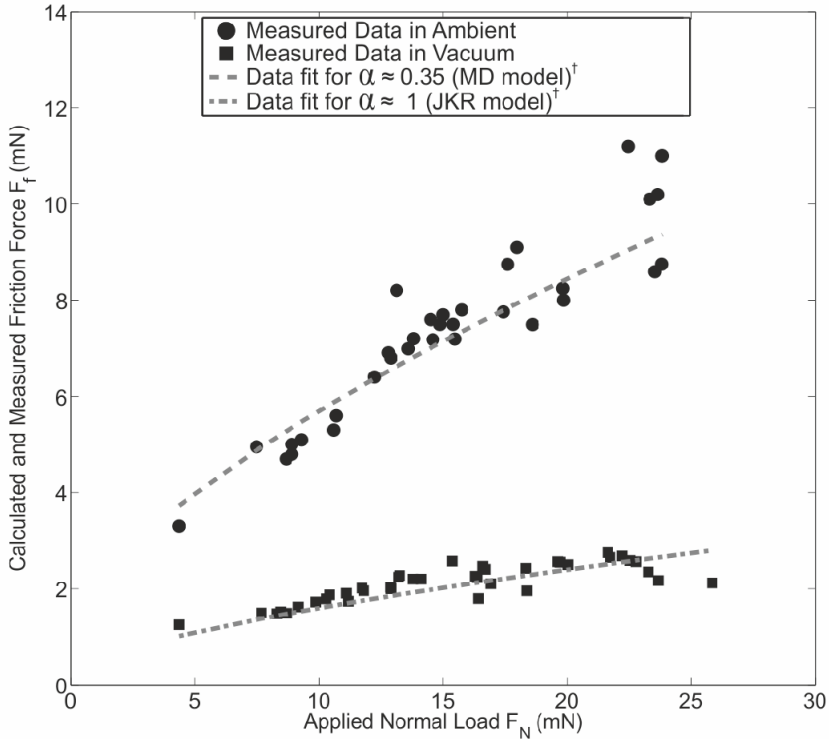

Figure 7.5. Measured static friction force versus normal load data, with a 5 mm diameter silicon ball and a float glass flat surface. Fit of data to the JKR and M–D model using Eq. 7.10 and Eq. 7.11†. The two free fitting parameters are the interfacial shear strength τ and the transition parameter α.

A typical friction force measurement was shown in Figure 6.8 where the force–displacement curve was shown for both measured in ambient as well as in HV. The applied normal load for the measurements shown in Figure 6.8 is *15 mN* and the resulting static friction force is *7.6 mN* and *1.55 mN* in ambient and HV respectively. Similar friction force measurements were performed by stepwise increase in the normal load and the measurement results along with the data fit using Eq. 7.11 are shown in Figure 7.5.

In Figure 7.5 the measured static friction force is plotted against the applied normal load when operating in ambient as well as in HV conditions. The data fit on these measured points is plotted using a procedure explained above. Once the value of contact radius is known for all the values of applied normal load, the value of the average interfacial shear strength calculated for the JKR and DMT models was used as a boundary for the shear stress in Eq. 7.10. The calculated values of work of adhesion and average shear stress for ambient as well as for HV conditions are shown in Table 7.1. The values for the JKR and DMT models are shown in Table 7.1 along with the values used to generate the data fit on the measurement data. By choosing the appropriate values of α ($0 < \alpha < 1$) and τ ($\tau_{JKR} < \tau < \tau_{DMT}$) the friction force can be calculated as a function of applied normal load for JKR, DMT and M–D models. It can be seen from Table 7.1 that the values of the shear stress satisfy the condition of $\tau_{JKR} < \tau < \tau_{DMT}$. It is clear from Figure 7.5 that for HV conditions the measured data followed the JKR trend, as the value of α determined from the measured data is approximately *1*. However, for measurements performed in ambient conditions the data fit follows the M–D model as the value of α is approximately *0.35*. A step-by-step diagram showing each step in analysing the measured data is shown in Figure 7.6.

The value of work of adhesion calculated to plot the data fit on the measured data shown in Table 7.1 for ambient conditions lies between the JKR and DMT limits. The meniscus forces are dominant in ambient conditions and the pull-off force required to break the contact is also contributed by the surface tension of water. However, in HV the low value of work of adhesion was calculated, which is very close to the values calculated using JKR model. The possible reason for this low value is that even at HV conditions there are molecular thick adsorbed layers present and it is known that the surface energy reduces if there are adsorbed layers present on the surfaces [7].

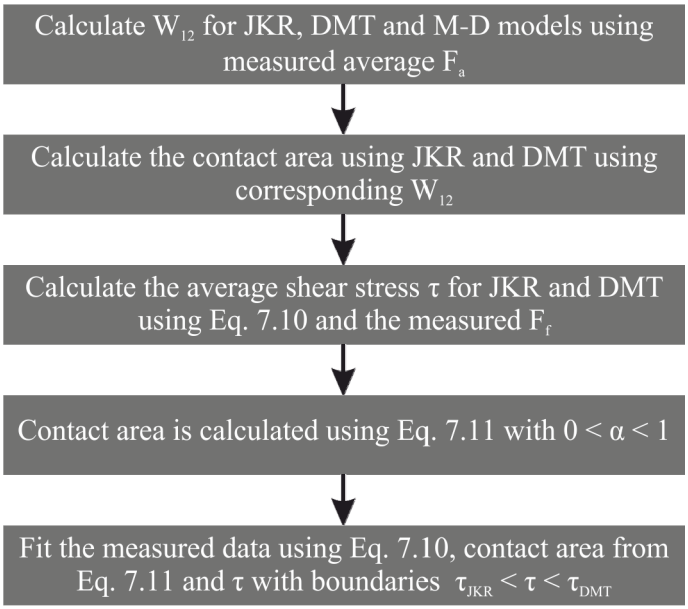

Figure 7.6. A step-by-step process to calculate the data fit on the measured friction force data. During the process the work of adhesion and shear stress in the interface are also calculated.

It can also be seen that the predicted model explained in section 7.2 corresponds to the trend of the measured static friction force. Solving the modified λ_{cap} value for ambient conditions ($RH \approx 45\%$) and solving the λ value for HV conditions ($RH < 5\%$) in the M–D model, the appropriate contact mechanics model can be selected using Figure 7.3. The predicted model can be verified using the adhesion and friction measurements and plotting the data fit for the predicted contact mechanics model on the measured data using the procedure mentioned above. It can also be seen that the measured static friction force in ambient is much higher than the static friction force measured in HV. As shown in Figure 5.2, the adhesion force in ambient conditions is also much higher than the adhesion force in HV conditions. Therefore, it can be stated that due to the higher value of adhesion force in ambient conditions a higher value of friction force has been experienced.

Table 7.1: Calculated work of adhesion and the shear stress from the measured adhesion and friction force.

Model	Work of adhesion W_{12} (mJ/m^2)		Shear stress τ (MPa)	
	Ambient	HV	Ambient	HV
JKR	88.5	20	23.6	8.2
DMT	66.3	15	32	9.6
Fit	73.7	19.3	27	8.5

7.5 Summary

A method was discussed to analyse and to interpret the adhesion and friction force measurements at different values of applied loads performed in different environmental conditions based on the M–D and modified M–D model. The work of adhesion and the shear stress at the interface can be calculated by combining adhesion and friction force measurements at different applied loads. The model shows that the solid–solid contact radius a decreases with the increase in the RH, whereas the adhesive radius or total contact radius c increases with the increase in RH. This can be verified from the experimental results: that the contact radius increases when the system is operating in ambient as compared to when operating in HV. A step-by-step method was discussed to calculate the work of adhesion and the shear stress in the contact. This method can be used to analyse the measured data in more detail. It has been shown that the predicted contact mechanics model fits very well to the measured values of the normal load dependent static friction force. For a smooth contact, the adhesion and static friction force are much higher when measured in ambient than in HV conditions. This is because the contact area and the shear stress in ambient conditions are larger than the contact area and shear stress in HV conditions.

Chapter 8
CONCLUSIONS AND RECOMMENDATIONS

This section of the thesis outlines the main conclusions that were already summarized at the end of each chapter. A discussion then follows, to present topic which require more attention to refine the models as well as the comparisons with the experimental results. Finally, some recommendation for further research are put forward.

8.1 Conclusions

Chapter 2: Adhesion and friction force mechanisms

- Van der Waals and capillary forces are dominant contributors on the adhesion force in a contact and are influenced by parameters like relative humidity and contact time.

Chapter 3: Experimental setup, materials and procedures

- An experimental setup was designed and tested to measure the adhesion and friction force in ambient as well as in high vacuum (HV) conditions. The setup is capable of measuring forces with an accuracy better than $8\ \mu N$.

- The disturbances from different vibrating sources were reduced by isolating the sources from the setup. Eddy current damping was used to achieve the desired accuracy in the measurements.

- The heart of the vacuum-based adhesion and friction tester (VAFT) is a dedicated force measuring mechanism (FMM), which is designed to measure the adhesion and friction force independently.

- The important step in performing contact measurements is to find the point of contact between two surfaces. A method to find the contact by studying the amplitude and frequency shift in the power spectrum of the measurement signal has been proven to be accurate and successful.

Chapter 4: Modelling the adhesion force for single asperity contact

- A model for calculating the adhesion force as a function of relative humidity (RH) between hydrophilic materials was developed. The model utilizes the thickness of the absorbed layer according to BET adsorption theory to predict the transitions in the adhesion force as a function of RH.

- The results show that the adhesion force calculated only by using the capillary force equation based on Kelvin and Young-Laplace relations underestimates the total adhesion force present in the contact. Similarly, this equation cannot be used to calculate the adhesion force at low RH.

- The transition and trends of the adhesion force as a function of RH predicted by the model fits very well with the data from the literature for small radii.

- The interdependency of normal load and contact time effects on the adhesion force was discussed. It was argued that at short contact times a normal load dependent adhesion force is expected under ambient conditions. In this case, the adhesion force is expected to change with the normal load to the power of *2/3*.

- The normal load dependency of the adhesion force is not expected to happen when the same system is operated in HV conditions since the time dependent behaviour is caused by condensation and surface diffusion effects.

- The effect of contact time on the adhesion force in the ambient conditions is given by an exponential function since the capillary condensation is a thermally activated process.

Chapter 5: Adhesion force measurements

- The effect of RH on the adhesion force was studied by performing adhesion measurements in HV (dry) and ambient conditions by changing the RH. The experimental results were compared with the theoretical model developed in Chapter 4 and considering the roughness effects as a scaling factor in the experimental results, the model fits very well.

- The experimental results confirm that for short contact times the adhesion force in ambient conditions changes with the normal load to the power of *2/3*. However, it remains constant when the contact operates in HV.

- Contact time effects on the adhesion force confirm the exponential behaviour of the adhesion force as a function of contact time.

- The interdependent effects of size of the asperity and the surface roughness were also presented. The adhesion force has been shown to be linearly dependent on the size of the asperity, which is in correspondence with the theory.

Chapter 6: Pre-sliding behaviour of single asperity contact

- The theoretical trends of the static friction force, the coefficient of static friction (COSF) and the preliminary displacement as a function of the applied normal load were derived.

- The results of sliding experiments performed at low contact pressures show that the static friction force, COSF and preliminary displacement follow the normal load dependent derived theoretical trends.

- The COSF has also been measured for Si-glass interface in ambient and HV conditions. It was shown that the COSF decreases when the interface is operated in HV and is dependent on applied normal load to the power of *-1/3*.

- Experimental results have shown that the Mindlin's model can be used to calculate the preliminary displacement when the contact pressure is of the order of 100 MPa. At small contact pressures, adhesion effects limit the agreement between model and experiments.

- An increase in the shear stress with the increase in the applied normal load is found. It has been shown that at low applied normal loads the shear stress in the contact is dependent on the normal load, whereas at high loads it becomes constant. This is explained by adhesion effects.

Chapter 7: Relation between adhesion and static friction

- A method was discussed to analyse and interpret the adhesion and friction force measurements performed at different values of applied normal load. The modified Maugis-Dugdale (M-D) model incorporating capillary force is suitable to interpret the adhesion measurement performed in ambient as well as in HV conditions.

- The results show that the RH can influence the applicable contact model to calculate the contact area. It has been shown for the Si-glass interface (a case study) that in dry (HV) conditions JKR model is applicable whereas in relatively wet (RH ≈ 50%) conditions the M-D model is suitable to calculate the contact area and the work of adhesion. This was confirmed by the calculated values of the work of adhesion and the average shear stress using experimental data.

- Static friction force measurements both in ambient and HV conditions were used to calculate the average shear stress of the interface. The measured static friction force data as a function of applied normal load was fitted using the appropriate contact model. It has been shown that the predicted contact model using the modified M-D model fits very well to the static friction force data.

8.2 Discussion

The focus of this study was to investigate the adhesion and friction behaviour of a single asperity contact. Therefore the adhesion and static friction models have been developed using perfectly smooth surfaces and not taking into account the surface roughness effects. However, it has been seen from the measurements that the influence of surface roughness on the adhesion and friction force cannot be ignored. A significant difference is seen if the surface roughness is higher than a few nanometres. Both van der Waals and capillary forces are very sensitive to the presence of small details on engineered surfaces. The magnitude of the adhesion force as a function of RH is also affected by the surface roughness. It has been reported in many articles that the increase in the surface roughness will decrease the adhesion force. Furthermore, for a certain rough contact the adhesion force measured in low RH (Figure 8.1(a)) will be lower than the force measured in high RH (Figure 8.1(b)). The reason for this increase is because at low RH the water will condense around the contacting asperities and at high RH the whole contact is so-called flooded with water as shown in Figure 8.1(a) and Figure 8.1(b). Similarly, the effect of contact time is also influenced by the surface roughness.

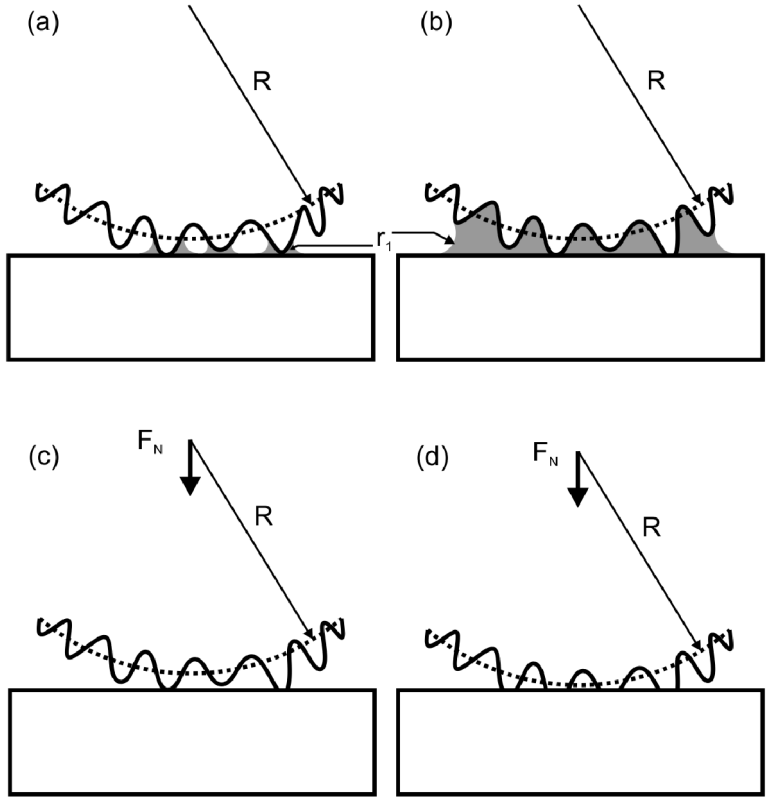

Figure 8.1. Schematic representation of the influence of surface roughness on the interface. (a) At low RH menisci will form around the asperities in contact or close to the counter surface. (b) At high RH a larger meniscus will be formed and the whole contact is "flooded". (c) At certain applied normal load F_N only a few asperities are in contact with the counter surface. (d) Increased F_N where more asperities make a contact and some are deformed.

The influence of normal load on adhesion as well as friction force will be different since the real area of contact increases with the increase in normal load and more asperities will deform and make contact with the counter surface as shown in Figure 8.1(d). Therefore, it is required to consider the influence of surface roughness on the measurements. The effect of contact time, roughness, as well as normal load will be strongly interrelated.

8.3 Recommendations

The effect of surface roughness on the adhesion and friction force can be addressed in two ways. First, it can be included in the adhesion and friction models discussed in this thesis. Secondly, the measurements have to be performed in a way that enables the effect of surface roughness to be studied.

- The surface roughness should be incorporated into the model by considering the surface parameters of the real engineering surfaces. A model can be developed by investigating stochastic and random nature of the surface and not by simplifying the surface profile. Since the adhesion and friction forces are so sensitive to the surface roughness, the simplification of the surface profile cannot give the right estimate of these forces.

- Adhesion and friction measurements have to be performed with different interfaces of well-defined roughness, e.g. using textured surfaces, by keeping the parameters like RH, size of the sphere, normal load, contact time and loading/unloading rate constant. The experiments should be supported by additional measurement techniques. In an ideal case, the real contact area should be measured or even the actual size of the microcontacts can be measured. The potential techniques to measure the real contact area could be based on thermal conductivity, electrical resistance or ultrasound techniques.

APPENDICES

Appendix A

Calculations for hole hinges and flexure hinges

The building block of the design of the FMM is a hole hinge. In Chapter 3 the stiffness of the hole hinge in adjustable direction was given. Here the stiffness of a hole hinge in tensile and shear direction are given along with the calculated values. The approximate solution of the stiffness are given by [49]:

$$k_t = 0.48\sqrt{\frac{t_h}{D_h}}E_{Al}w_h \tag{A.1}$$

$$k_s = \frac{0.56\sqrt{\frac{t_h}{D_h}}E_{Al}w_h}{1.2+\frac{D_h}{t_h}} \tag{A.2}$$

Using Eq. (A.1) and (A.2), the stiffness in the tensile direction k_t and the stiffness in the shear direction k_s for a compound parallelogram flexure mechanism as shown in Figure 3.4 is calculated to be 1.14×10^8 N/m and 7.8×10^6 N/m respectively.

Appendix B

Measured surface roughness of materials

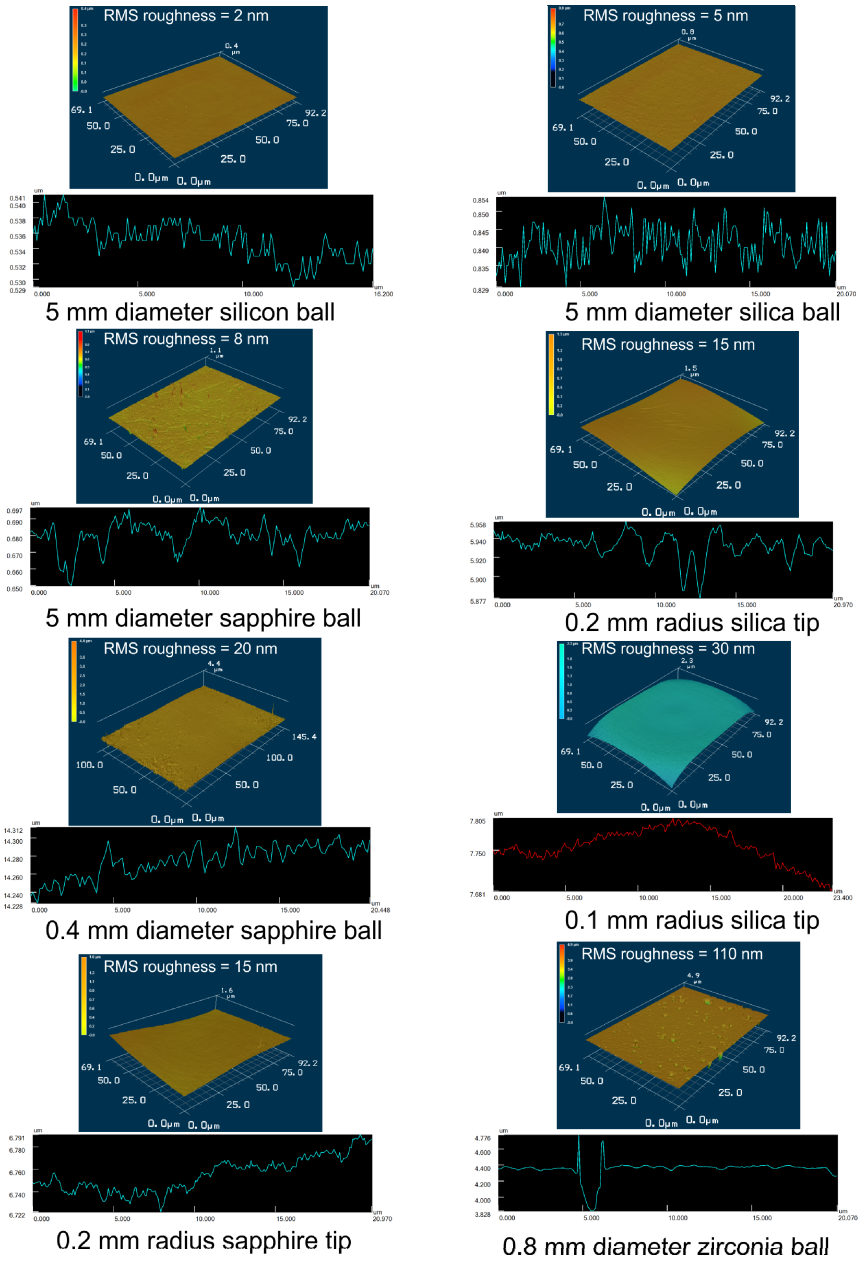

Figure B.1. Surface roughness measurements with the Keyence Confocal Microscope on different sized spheres and tips of silicon, silica, sapphire and zirconia.

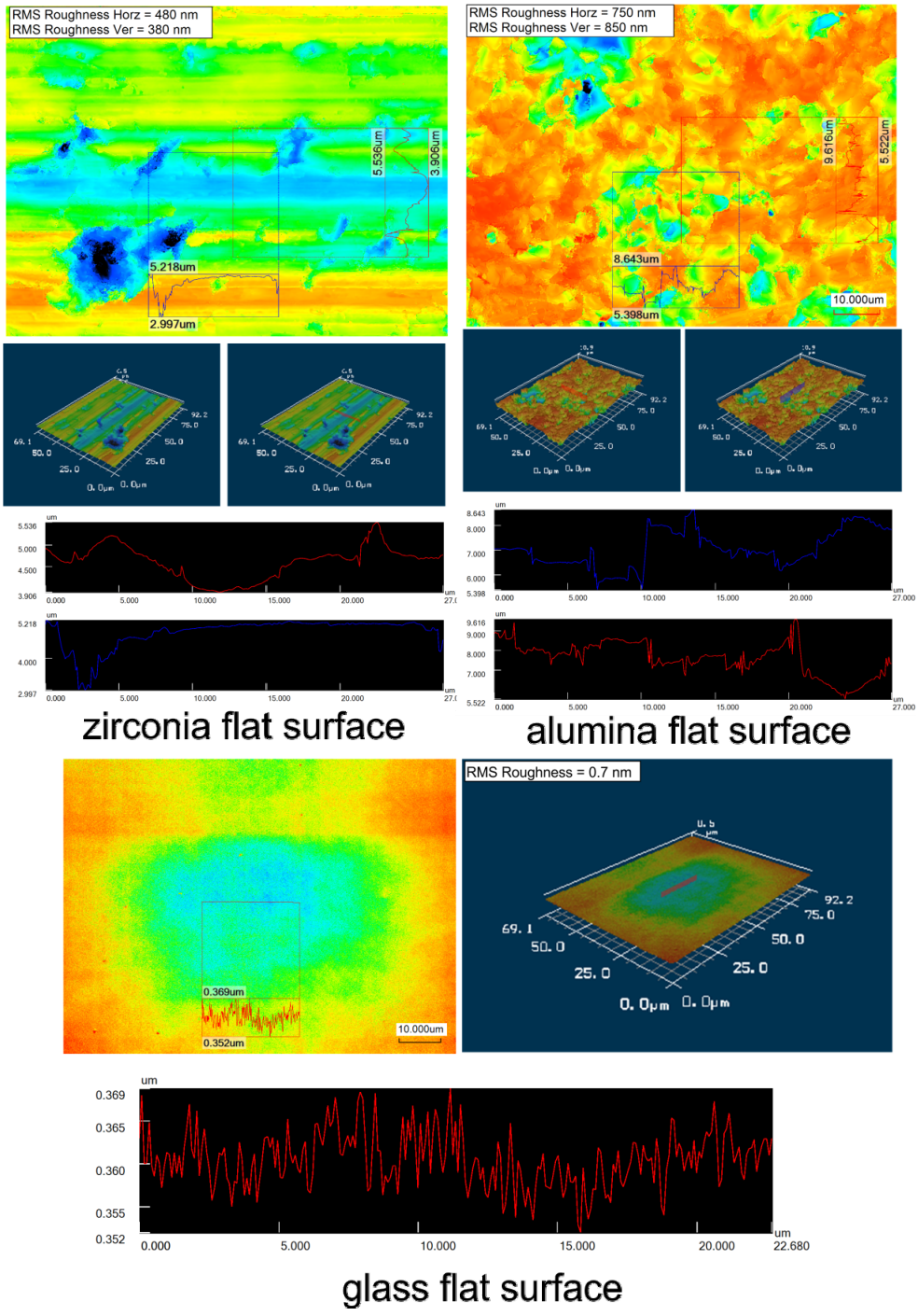

Figure B.2. Surface roughness measurements with the Keyence Confocal Microscope on different sized spheres and tips of silicon, silica, sapphire and zirconia.

Appendix C

Contact angle measurements

Contact angle measurements were performed using the Sessile drop method at ambient conditions (20 ◦C) with a contact angle goniometer (Dataphysics OCA20) on flat substrates of Glass, Silicon with a native oxide, Zirconia and Alumina. Zirconia and Alumina flat surfaces are very rough and the surfaces were cleaned before measuring the contact angle using an ultrasonic bath of Isopropyl Alcohol (IPA) for 15 minutes, then they were rinsed and dried. The measurements are shown in Figure C.1. The measurements shown were performed using water as a liquid.

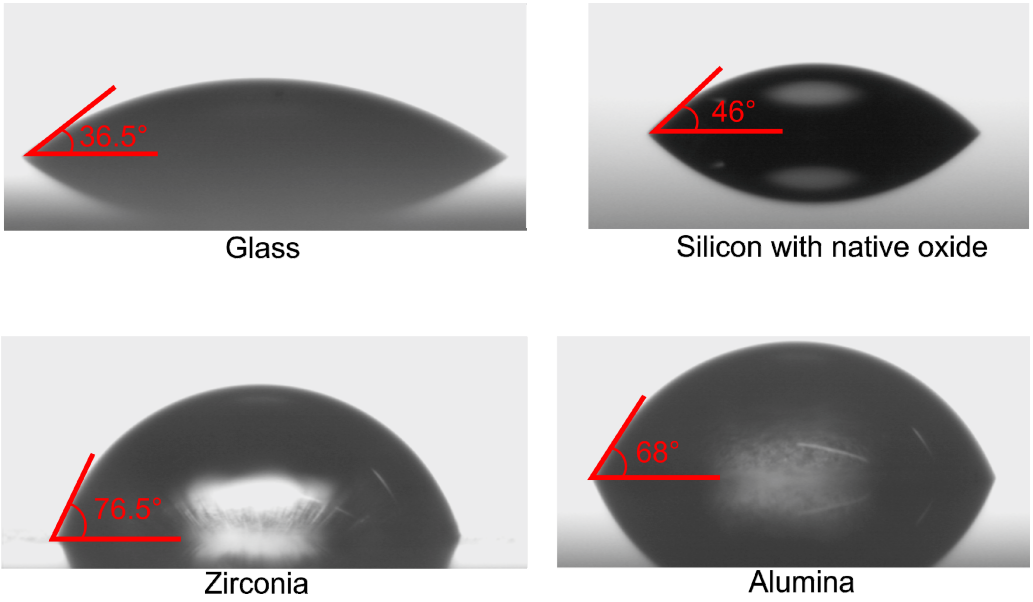

Figure C.1. Contact angle measurements on different substrates and water using Sessile drop method.

Appendix D

Mass spectrometer measurements

Measurements were performed to measure the partial pressures of the gases inside the vacuum chamber when the chamber is pumped to high vacuum (HV) conditions. The measurements were performed in such a way that first the chamber is pumped down to 10^{-7} mbar as shown in Figure D.1(a). It can be clearly seen that the partial pressure of water and the total partial pressure of the chamber are almost equal. Then, for a short moment, the vacuum pump is turned off and the total pressure starts to increase as shown in Figure D.1(b). The partial pressures of all the gases also start to increase.

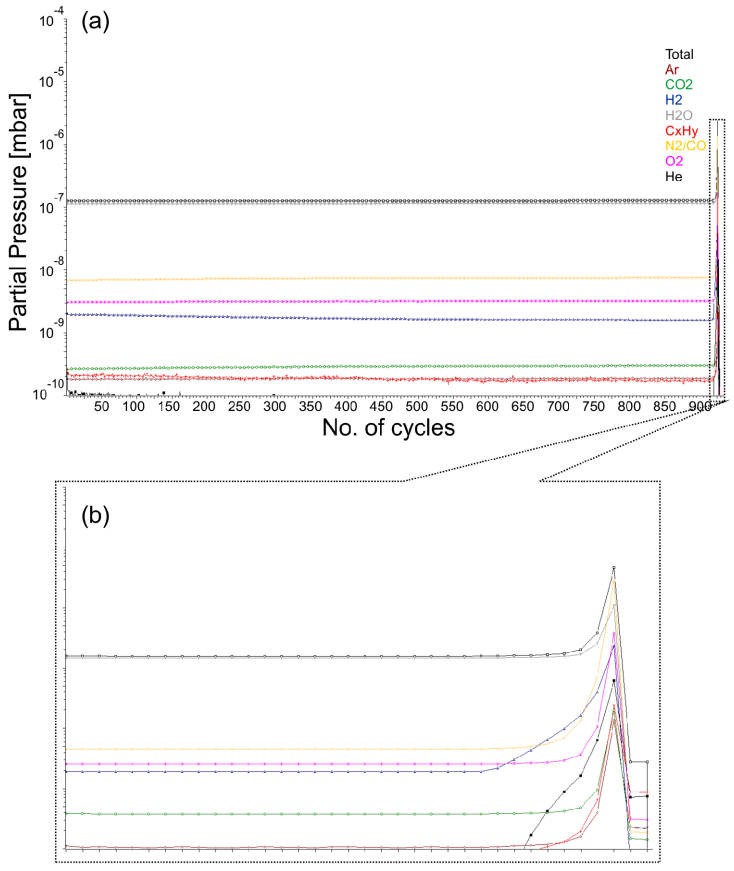

Figure D.1. Partial pressure of different gases present in the vacuum chamber measured with the mass spectrometer. In (a) the total measurement is shown and in (b) the zoomed-in region of (a) is shown indicating the increase in the partial pressures when turning off the vacuum pump.

REFERENCES

[1] Butt, H.-J. and Kappl, M., Normal capillary forces. *Advances in Colloid and Interface Science*. 146, pp. 48-60, 2009.

[2] Colak, A., Wormeester, H., Zandvliet, H.J.W. and Poelsema, B., Surface adhesion and its dependence on surface roughness and humidity measured with a flat tip. *Applied Surface Science*. 258, pp. 6938-6942, 2012.

[3] Grobelny, J., Pradeep, N., Kim, D.I. and Ying, Z.C., Quantification of the meniscus effect in adhesion force measurement. *Applied Physics Letters*. 88(091906), pp. 091906-1-091906-3, 2006.

[4] Jones, R., Pollock, H.M., Cleaver, J.A.S. and Hodges, C.S., Adhesion force between glass and silicon surfaces in air studied by AFM: Effects of relative humidity, particle size, roughness and surface treatment. *Langmuir*. 18, pp. 8045-8055, 2002.

[5] Mate C.M., *Tribology on small scale: A bottom up approach to friction, lubrication and wear*. 1st ed, Oxford University Press, 2008.

[6] Xiao, X. and Qian, L., Investigation of humidity-dependent capillary force. *Langmuir*. 16, pp. 8153-8158, 2000.

[7] Israelachivili, J.N., *Intermolecular and surface forces*. 2nd ed, Elsevier Ltd., 1991.

[8] Ata, A., Rabinovich, Y.I. and Singh, R.K., Role of surface roughness in capillary adhesion. *Journal of Adhesion Science and Technology*. 16(4), pp. 337-346, 2002.

[9] van Zwol, P.J., Palasantzas, G. and de Hosson, J.T.M., Influence of roughness on capillary forces between hydrophilic surfaces. *Physical Review E*. 78(031606), pp. 1-6, 2008.

[10] van Zwol, P.J., *Contact mode casimir and capillary force measurements,* PhD Thesis, University of Groningen, pp. 49-74, 2011.

[11] Chilamakuri, S.K. and Bhushan, B., A comprehensive kinetic meniscus model for prediction of long-term static friction. *Journal of Applied Physics*. 86(8), pp. 4649-4656, 1999.

[12] Liu, L. and Bushan, B., Adhesion and friction studies of microelectromechanical systems/ nanoelectromechanical systems

materials using a novel microtriboapparatus. *Journal of Vacuum Science and Technology A*. 21(4), pp. 1528-1538, 2003.

[13] Ciavarella, M., The generalized Cattaneo partial slip plane contact problem. I-theory. *International Journal of Solids and Structures*. 35(18), pp. 2349-2362, 1998.

[14] Mindlin, R.D., Compliance of elastic bodies in contact. *ASME Journal of Applied Mechanics*. 16, pp. 259-268, 1949.

[15] Mindlin, R.D. and Deresiewicz, H., Elastic spheres in contact under varying oblique forces. *Journal of Applied Mechanics*. 20, pp. 327-344, 1953.

[16] Butt, H.-J., Graf, K. and Kappl, M., *Physics and chemistry of interfaces*, Wiley-VCH: Weinheim. 177-203, 2003.

[17] Casimir, H.B.G. and Polder, D., The influence of retardation on London-van der Waals forces. *Physical Review*. 73(4), pp. 360-372, 1948.

[18] Colton, R.J., Nanoscale measurements and manipulation. *Journal of Vacuum Science and Technology*. 22(4), pp. 1609-1635, 2004.

[19] Bordag, M., Mohideen, U. and Mostepanenko, V.M., New developments in the Casimir effect. *Physics Reports*. 353(1-3), pp. 1-205, 2001.

[20] Guerret-Piecourt, C., Bec, S., Segault, F., Juve, D., Treheux, D. and Tonck, A., Adhesion forces due to nano-triboelectrification between similar materials. *The European Physical Journal : Applied Physics*. 28, pp. 65-72, 2004.

[21] Feiler, A.A., Stiernstedt, J., Theander, K., Jenkins, P. and Rutland, M., Effect of capillary condensation on friction force and adhesion. *Langmuir*. 23, pp. 517-522, 2007.

[22] Jinesh, K.B. and Frenken, J.W.M., Capillary condesation in atomic scale friction: How water acts like glue. *Physical Review Letters*. 96(16), pp. 166103-1-166103-4, 2006.

[23] Sirghi, L., Szoszkiewicz, R. and Riedo, E., Volume of a nanoscale water bridge. *Langmuir*. 22, pp. 1093-1098, 2006.

[24] He, M., Blum, A.S., Aston, D.E., Buenviaje, C. and Overney, R.M., Critical phenomena of water bridges in nanoasperity contacts. *Journal of Chemical Physics*. 114(3), pp. 1355-1360, 2001.

[25] van Zwol, P.J., Palasantzas, G. and de Hosson, J.T.M., Influence of random roughness on the adhesion between metal surfaces due to capillary condensation. *Applied Physics Letters*. 91(101905), 2007.

[26] Rabinovich, Y.I., Alder, J.J., Esayanur, M.S., Ata, A., Singh, R.K. and Moudgil, B.M., Capillary forces between surfaces with nanoscale roughness. *Advances in Colloid and Interface Science*. 96, pp. 213-230, 2002.

[27] Rabinovich, Y.I., Alder, J.J., Ata, A., Singh, R.K. and Moudgil, B.M., Adhesion between nanoscale rough surfaces II. Measurement and comparison with theory. *Journal of Colloid and Interface Science*. 232, pp. 17-24, 2000.

[28] Johnson, K.L., *Contact mechanics*, Cambridge University Press: UK, 1985.

[29] Johnson, K.L., Kendall, K. and Roberts, A.D., Surface energy and the contact of elastic solids. in *Proceedings of Royal Society of London. Series A, Mathematical and Physical Sciences*, 1971.

[30] Gnecco, E., Bennewitz, R., Gyalog, T. and Meyer, E., Friction experiments on the nanometre scale. *Journal of Physics: Condensed Matter*. 13, pp. 619-642, 2001.

[31] Greenwood, J.A. and Williamson, J.B.P., Contact of nominally flat surfaces. *Proceedings of Royal Society of London. Series A, Mathematical and Physical Sciences*. 295, pp. 300-319, 1966.

[32] Adams, G.G. and Nosonovsky, M., Contact modeling - forces. *Tribology International*. 33, pp. 431-442, 2000.

[33] Johnson, K.L., Adhesion and friction between a smooth elastic spherical asperity and a plane surface. in *Royal Society of London. Series A, Mathematical and Physical Sciences*, 1997.

[34] Johnson, K.L., Mechanics of adhesion. *Tribology International*. 31(8), pp. 413-418, 1998.

[35] Yoshizawa, H., Chen, Y.L. and Israelachvili, J., Fundamental mechanisms of interfacial friction. Relation between adhesion and friction. *Journal of Physical Chemistry*. 97(16), pp. 4128-4140, 1993.

[36] Tabor, D., Surface forces and surface interactions. *Journal of Colloid and Interface Science*. 58(1), pp. 1-13, 1977.

[37] Maugis, D., Adhesion of spheres: The JKR-DMT transition using a Dugdale model. *Journal of Colloid and Interface Science*. 150(1), pp. 243-269, 1992.

[38] Johnson, K.L. and Greenwood, J.A., An adhesion map for the contact of elastic spheres. *Journal of Colloid and Interface Science*. 192, pp. 326–333, 1997.

[39] Xu, D., Liechti, K.M. and Ravi-Chandar, K., On the modified Tabor parameter for the JKR-DMT transition in the presence of a liquid meniscus. *Journal of Colloid and Interface Science*. 315, pp. 772-785, 2007.

[40] Feldman, K., Fritz, M., Hahner, G., Marti, A. and Spencer, N.D., Surface forces, surface chemistry and tribology. *Tribology International*. 31(1-3), pp. 99-105, 1998.

[41] Anderson, S., Soderberg, A. and Bjorklund, S., Friction models for sliding dry, boundary and mixed lubricated contacts. *Tribology International*. 40, pp. 580-587, 2007.
[42] Luo J., Hu Y., and Wen S., *Physics and chemistry of micro-nanotribology*, ASTM International, 2008.
[43] Bhushan, B., *Introduction to tribology*, John Wiley & Sons: New York, 2002.
[44] Johnson, K.L., Surface interaction between elastically loaded bodies under tangential forces. *Proceedings of Royal Society of London. Series A, Mathematical and Physical Sciences*. 230, pp. 531-548, 1955.
[45] Agilent technologies vacuum technologies – product catalogue 2010, catalogue for turbo pumps. Last visit 04-08-2012; Available from: www.chem.agilent.com.
[46] Sodano, H.A., *Development of novel eddy current dampers for the suppression of structural vibrations,* PhD Thesis, Virginia Polytechnic Institute and State University, pp. 44–94, 2005.
[47] Bae, J.-S., Kwak, M.K. and Inman, D.J., Vibration suppression of a cantilever beam using eddy current damper. *Journal of Sound and Vibrations*. 284, pp. 805-824, 2005.
[48] Awtar, S., *Synthesis and analysis of parallel kinematic xy flexure mechanism,* PhD Thesis, Massachusetts Institute of Technology, pp. 23-42, 2004.
[49] Koster, M.P. and van der Hoek, W., *Design principles for accurate moving and positioning (constructieprincipes)*, Twente University Press, 2000.
[50] Material properties of silicon, borosilicate glass and alumina. Last visit 04-08-2012; Available from: www.matweb.com.
[51] Material properties of silica and sapphire. Last visit 04-08-2012; Available from: www.ispoptics.com.
[52] Material properties of silica, zirconia and alumina. Last visit 04-08-2012; Available from: www.ceramics.nist.gov.
[53] Material properties of borosilicate glass. Last visit 04-08-2012; Available from: www.schott.com.
[54] Asif, S.A.S., Wahl, K.J. and Colton, R.J., Nanoindentation and contact stiffness measurement using force modulation with a capacitive load-displacement transducer. *Review of Scientific Instruments*. 70(5), pp. 2408-2416, 1999.
[55] Asay D.B. and Kim S.H., Evolution of the adsorbed water layer structure on silicon oxide at room temperature. *Journal of Physical Chemistry B*. 109(35), pp. 16760-16763, 2005.
[56] Verdaguer, A., Weis, C., Oncins, G., Ketteler, G., Bluhm, H. and Slameron, M., Growth and structure of water on SiO2 films on si

investigated by Kelvin probe microscopy and in situ X-ray spectroscopies. *Langmuir*. 23, pp. 9699-9703, 2007.

[57] Mizushima S., Determination of the amount of gas adsorption on SiO2/Si(100) surfaces to realize precise mass measurement. *Metrologia*. 41, pp. 137-144, 2004.

[58] Mizushima S., The improvement of the adsorption characteristics of stainless steel surfaces by sputter-deposited films. *Metrologia*. 44, pp. 161-166, 2007.

[59] Naono, H. and Hakuman, M., Analysis of adsorption isotherms of water vapor for nonporous and porous adsorbents. *Journal of Colloid and Interface Science*. 145(2), pp. 405-412, 1991.

[60] Ferreira, O.D.S., Gelinck, E.R.M., de Graaf, D. and Fischer, H.R., Adhesion experiments using an AFM-parameters of influence. *Applied Surface Science*. 257, pp. 48-55, 2010.

[61] Riedo, E., Palaci, I., Boragno, C. and Brune, H., The 2/3 power law dependence of capillary force on normal load in nanoscopic friction. *Journal of Physical Chemistry B*. 108, pp. 5324-5328, 2004.

[62] Nasrallah, H., *Capillary adhesion and friction - an approach with the afm circular mode,* PhD Thesis, Université du Maine, pp. 45-65, 2011.

[63] Smith, D.L., *Thin-film deposition: Principles and practice*, McGraw-Hill Inc., 1995.

[64] Xu, L., Lio, A., Hu, J., Ogletree, D.F. and Salmeron, M., Wetting and capillary phenomenon of water on mica. *Journal of Physical Chemistry B*. 102, pp. 540-548, 1998.

[65] Bocquet, L., Charlaix, E., Ciliberto, S. and Crassous, J., Moisture-induced ageing in granular media and the kinetics of capillary condensation. *Nature*. 396, pp. 735-737, 1998.

[66] Xu, L. and Siedlecki, C.A., Effects of surface wettability and contact time on protein adhesion to biomaterial surfaces. *Biomaterials*. 28, pp. 3273-3283, 2007.

[67] Xu, L. and Siedlecki, C.A., Atomic force microscopy studies of the initial interactions between fibrinogen and surfaces. *Langmuir*. 25, pp. 3675-3681, 2009.

[68] Szoszkiewicz, R. and Riedo, E., Nucleation time of nanoscale water bridges. *Physical Review Letters*. 95(135502), pp. 1-4, 2005.

[69] Specifications of UNAT. Last visit 11-06-2012; Available from: www.asmec.de.

[70] Fuller, K.N.G. and Tabor, D., The effect of surface roughness on the adhesion of elastic solids. *Proceedings of Royal Society of London. Series A, Mathematical and Physical Sciences*. 345, pp. 327-342, 1975.

[71] Popov, V.L., *Contact mechanics and friction. Physical principles and application*, Springer: Germany, 2010.

[72] Mazeran, P.E. and Beyaoui, M., Initiation of sliding of an elastic contact at a nanometer scale under a scanning force microscope probe. *Tribology Letters*. 30, pp. 1-11, 2008.

[73] Brun, X.F. and Melkote, S.N., Modeling and experimental verification of a partial slip for multiple frictional contact problems. *Wear*. 256, pp. 34-41, 2008.

[74] Zolotarevskiy, V. and Kligerman, Y., Elastic-plastic spherical contact under cyclic tangential loading in pre-sliding. *Wear*. 270, pp. 888-894, 2011.

[75] Bowden, F.P. and Tabor, D., *The friction and lubrication of solids*, Oxford University Press, 1950.

[76] Carpick, R.W., Agrait, N., Ogletree, D.F. and Salmeron, M., Measurement of interfacial shear (friction) with an ultrahigh vacuum atomic force microscope. *Journal of Vacuum Science and Technology B*. 14(2), pp. 1289-1295, 1996.

[77] Schwarz, U.D., Zworner, O., Koster, P. and Wiesendanger, R., Quantitive analysis of the frictional properties of solid materials at low loads. I. Carbon compounds. *Physical Review B*. 56(11), pp. 6987-6996, 1997.

[78] Xu, D., Liechti, K.M. and Ravi-Chandar, K., On scale dependence in friction: Transition from intimate to monolayer-lubricated contact. *Journal of Colloid and Interface Science*. 318, pp. 507-519, 2008.

[79] Carpick, R.W., Ogletree, D.F. and Salmeron, M., A general equation for fitting contact area and friction vs load measurements. *Journal of Colloid and Interface Science*. 211(2), pp. 395-400, 1999.

[80] Schwarz, U.D., A generalized analytical model for the elastic deformation of an adhesive contact between a sphere and a flat surface. *Journal of Colloid and Interface Science*. 261, pp. 99-106, 2003.

ISBN: 978-90-77172-86-5